

**DESIGN AND COMMISSIONING OF A TEST STAND TO CONDUCT  
PERFORMANCE DEGRADATION STUDIES AND ACCELERATED LIFE  
TESTING ON WATER-COOLED VARIABLE-SPEED SCREW  
COMPRESSOR CHILLERS**

by

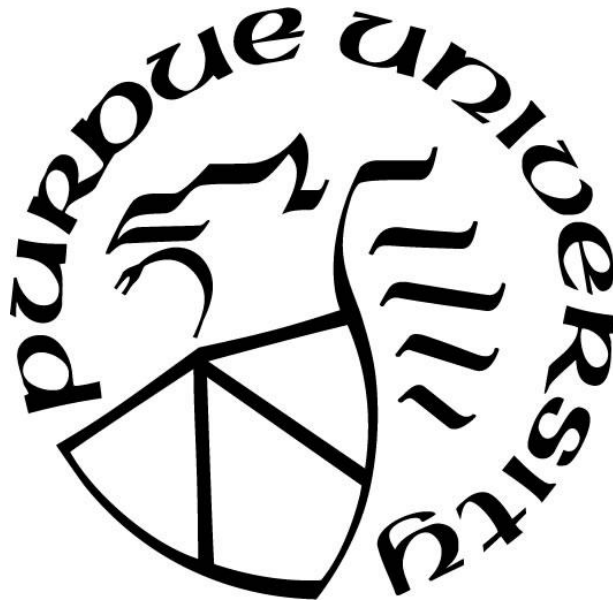
**Andreas Josef Hoess**

**A Thesis**

*Submitted to the Faculty of Purdue University*

*In Partial Fulfillment of the Requirements for the degree of*

**Master of Science in Mechanical Engineering**



School of Mechanical Engineering

West Lafayette, Indiana

May 2022

**THE PURDUE UNIVERSITY GRADUATE SCHOOL  
STATEMENT OF COMMITTEE APPROVAL**

**Dr. Davide Ziviani, Co-Chair**

School of Mechanical Engineering

**Dr.-Ing. Eckhard A. Groll, Co-Chair**

School of Mechanical Engineering

**Dr. James E. Braun**

School of Mechanical Engineering

**Approved by:**

Dr. Nicole Key

## ACKNOWLEDGMENTS

To my family, for their support and motivation to come to the U.S., especially during the Corona lockdown but generally during my whole Master's.

To my advisors Professor Groll, Professor Ziviani, Professor Braun for your mentorship, patience, and consistent support. Thank you for your advice and guidance that helps me to develop not just professionally but also in a personally. The passion for thermodynamic that you share is contagious and together with you deep knowledge and experience it makes the Herrick Labs the valuable place it is.

To my colleagues at the Herrick Labs in particular I would like to thank Changkuan “Steven” Liang, Weigang Hou, Jaewon Park, Parveen Dhillon, Haotian Liu, Riley Barta, Jon Ore, Nick Salts, Marie Shelly, Leon Brendel, and John Brehm not just for their and consistent support with my work at the Herrick Labs even after their graduation but also for their friendship which was extremely helpful.

To the technicians at the Herrick labs, Frank, Rob, Ryan and Charlie who always had a helping hand and trust in my skills, especially during the upgrade of the test stand.

To sponsors for their motivation and support as well as for bringing in their engineering expertise during every step of my work.

# TABLE OF CONTENTS

LIST OF TABLES .....	6
LIST OF FIGURES .....	8
LIST OF EQUATIONS .....	11
NOMENCLATURE .....	13
ABSTRACT .....	17
1. INTRODUCTION .....	18
1.1 Motivation.....	18
1.2 Literature Review.....	21
1.2.1 Simulation, impact evaluation, detection, and processing of faults .....	21
1.2.2 Accelerated life testing .....	28
1.2.3 FDD modeling .....	30
1.3 Thesis objectives and approach .....	35
2. DESIGN OF THE TEST SYSTEM .....	37
2.1 Selection of a water-cooled screw chiller .....	37
2.2 Development of the test stand design within setup steps.....	40
2.2.1 Overview and original test setup .....	40
2.2.2 Standard requirements and design targets .....	42
2.2.3 First generation test system .....	43
2.2.4 Commissioning and performance limits .....	48
2.2.5 Second generation test system .....	57
2.2.6 Water testing.....	61
3. EXPERIMENTAL TESTING.....	65
3.1 Baseline testing .....	65
3.1.1 Testplan.....	65
3.1.2 Data analysis.....	66
3.1.3 Test results .....	67
3.1.4 IPLV value.....	73
3.2 Accelerated life testing .....	77
3.2.1 Cycle assumptions .....	77

3.2.2	Test requirements.....	77
3.2.3	Test modes .....	78
3.2.4	Development of the test mode and test stand automation .....	82
3.3	Recurring baseline testing.....	90
3.4	System and fault analysis.....	93
3.4.1	System and sub-systems .....	93
3.4.2	Characteristic variables.....	95
3.4.3	Compressor .....	96
3.4.4	Electric drive system (Motor and VSD) .....	102
3.4.5	Heat exchanger .....	104
4.	PRELIMINARY SYSTEM MODEL .....	108
4.1	Objectives .....	108
4.2	Approach.....	108
5.	CONCLUSION.....	110
	APPENDIX I: P, H DIAGRAM OF THE BASELINE TEST CYCLES .....	111
	APPENDIX II: P, H DIAGRAM OF THE ACCELERATED LIFE TEST CYCLES.....	115
	APPENDIX III: P, H DIAGRAM OF THE RECURRING PERFORMANCE TEST CYCLES .....	117
	REFERENCES .....	133
	VITA .....	137
	PUBLICATIONS.....	138

## LIST OF TABLES

Table 1: Operating conditions and nominal performance [36].....	38
Table 2: Nominal performance under AHRI 550/590 test conditions [36] .....	38
Table 3: AHRI 550/590 standard rating conditions [38] .....	42
Table 4: Geometric information of the heat exchangers.....	47
Table 5: Comparison with specified heat exchanger data and model predictions .....	47
Table 6: Actual heat transfer rate for different load levels during the commissioning .....	50
Table 7: Mass flow in the chilled water cycle .....	51
Table 8: Maximum heat transfer rate on the chilled water side.....	52
Table 9: Maximum heat transfer rate on the condenser loop side .....	52
Table 10: Load dependent effectiveness of the chilled water heat exchanger.....	53
Table 11: Pressure drops of the single components within the evaporator loop .....	56
Table 12: Operating conditions and nominal performance [36].....	57
Table 13: Nominal performance under AHRI 550/590 test conditions [43] .....	57
Table 14: List of all sensors used in the second-generation setup.....	60
Table 15: Component list of second-generation test stand .....	61
Table 16: Test plan for 125 RT (439.6 kW) baseline testing.....	65
Table 17: Summary of the baseline test results .....	68
Table 18: Evaluated data at 32% load.....	69
Table 19: Evaluated data at 51% load.....	70
Table 20: Evaluated data at 76% load.....	71
Table 21: Evaluated data at 101% mode.....	72
Table 22: Measured and interpolated/extrapolated efficiency values as basis for IPLV calculation .....	73
Table 23: Chiller efficiency comparison.....	74
Table 24: Summary of the 1000 h-test results .....	91
Table 25: Measured and interpolated/extrapolated efficiency values as basis for the IPLV calculation.....	92
Table 26: Efficiency and IPLV value comparison.....	93

Table 27: Thermodynamic properties in cycle during 32% load baseline test run [48] .....	111
Table 28: Thermodynamic properties in cycle during 51% load baseline test run [48] .....	112
Table 29: Thermodynamic properties in cycle during 76% load baseline test run [48] .....	113
Table 30: Thermodynamic properties in cycle during 101% load baseline test run [48] .....	114
Table 31: Thermodynamic properties in cycle during “high load/low head” test cycle conditions [48] .....	115
Table 32: Thermodynamic properties in cycle during "low load/high head" test cycle conditions [48] .....	116
Table 33: Thermodynamic properties in cycle during 1000 h-test at 31% load [48] .....	117
Table 34: Evaluated data at 31% load (1000 h-test) .....	118
Table 35: Thermodynamic properties in cycle during 1000 h-test at 32% load [48] .....	119
Table 36: Evaluated data at 32% load (1000 h-test) .....	120
Table 37: Thermodynamic properties in cycle during 1000 h-test at 49% load [48] .....	121
Table 38: Evaluated data at 49% load (1000 h-test) .....	122
Table 39: Thermodynamic properties in cycle during 1000 h-test at 50% load [48] .....	123
Table 40: Evaluated data at 50% load (1000 h-test) .....	124
Table 41: Thermodynamic properties in cycle during 1000 h-test at 76% load [48] .....	125
Table 42: Evaluated data at 76% load (1000 h-test) .....	126
Table 43: Thermodynamic properties in cycle during 1000 h-test at 85% load [48] .....	127
Table 44: Evaluated data at 85% load (1000 h-test) .....	128
Table 45: Thermodynamic properties in cycle during 1000 h-test at 90% load [48] .....	129
Table 46: Evaluated data at 90% load (1000 h-test) .....	130
Table 47: Thermodynamic properties in cycle during 1000 h-test at 100% load [48] .....	131
Table 48 : Evaluated data at 100% load (1000 h-test) .....	132

## LIST OF FIGURES

Figure 1: U.S. energy consumption in the building sector (obtained from [7]).....	19
Figure 2: Mean impact on the overall efficiency of the chiller according to Comstock [14].....	22
Figure 3: Impact and correlation of faults on the components of a chiller (obtained from [18]).	24
Figure 4: Positions to mount accelerometers on a screw compressor (obtained from [22]).....	27
Figure 5: Representative failure rate for mechanical systems (obtained from [24]) .....	29
Figure 6: Physical setup of the York YVWA chiller [37] .....	38
Figure 7: Simplified refrigeration cycle of the York YVWA chiller series .....	39
Figure 8: Schematic of the original experimental system (based on [14]; [46]) .....	41
Figure 9: PI-Diagram of the first-generation system setup [46] .....	43
Figure 10: U-tube heat exchanger geometry (adapted from [39]) .....	45
Figure 11: 90% Load test run with first-generation test stand.....	48
Figure 12: Performance curve of the condenser water pump [41].....	54
Figure 13: Performance curve of the evaporator loop water pump [42].....	55
Figure 14: Simplified flow diagram of the evaporator loop with probe positions [46] .....	56
Figure 15: PI-diagram of the second-generation test stand [46].....	59
Figure 16: View on the test stand in the configuration of the second generation .....	59
Figure 17: Water test results .....	64
Figure 18: Efficiency values on the baseline test.....	68
Figure 19: Fluid temperatures during 32% test run .....	69
Figure 20: Fluid temperatures during 51% test run .....	70
Figure 21: Fluid temperatures at 76% test run.....	71
Figure 22: Fluid temperatures at 101% test run.....	72
Figure 23: Unit efficiency with interpolated values .....	74
Figure 24: Fluid temperatures during the baseline test runs [48] .....	76
Figure 25: LMTD of the evaporator during the baseline test runs [48].....	76
Figure 26: Ideal load curve for high load/low head operation.....	79
Figure 27: Temperature during operation in high load/low head-mode .....	79

Figure 28: Oil pressure and oil differential pressure during the high load/low head-mode [48]..	80
Figure 29: Ideal load curve for low load/high head-operation .....	81
Figure 30: Temperature during operation in low load/high head operation [48] .....	81
Figure 31: Motor temperatures during low load/high head operation [48] .....	82
Figure 32: GUI of the test stand controls in LabVIEW [47] .....	83
Figure 33: Implementation of the test automation .....	83
Figure 34: Temperature control scheme .....	84
Figure 35: Flow control scheme .....	85
Figure 36: Indicator details of the GUI [47] .....	89
Figure 37: Test menu selection [47] .....	89
Figure 38: PI diagram with real time measurement indicators in the GUI [46] .....	89
Figure 39: Real time temperature visualization [47] .....	90
Figure 40: Comparison of measured efficiencies oveat baseline test vs 1000 h-test.....	91
Figure 41: Overlay of 1000-test efficiencies over baseline .....	92
Figure 42: Sub-systems of the chiller [46].....	94
Figure 43: Characteristic variables for the fault analysis [46].....	95
Figure 44: Compressor power consumption [48] .....	96
Figure 45: Pressure levels in the systems [48].....	97
Figure 46: System oil pressure and oil differential pressure [48].....	98
Figure 47: Sight glasses of the oil separator during an operation with low (left) and high (right) pressure differential .....	98
Figure 48: Isentropic efficiency of the compressor .....	99
Figure 49: Superheat measured in the suction line .....	100
Figure 50: Super heat measured on the economizer port.....	101
Figure 51: Superheat in discharge line.....	101
Figure 52: VSD output frequency vs. VSD output voltage [48].....	102
Figure 53: Compressor phase current comparison [48].....	103
Figure 54: Motor temperatures [48].....	104
Figure 55: System fluid temperatures [48] .....	105
Figure 56: LMTD of the Condenser and the evaporator [48].....	106

Figure 57: Evaporator mass flow and capacity [48] .....	107
Figure 58: Condenser mass flow and capacity [48].....	107
Figure 59: Dymola modeling set up [49].....	109
Figure 60: P, h diagram of the cycle at 32% load during the baseline test [48] .....	111
Figure 61: P, h diagram of the cycle at 51% load during baseline test [48] .....	112
Figure 62: P, h diagram of the cycle at 76% load during baseline test [48] .....	113
Figure 63: P, h diagram of the cycle at 101% load during baseline test [48] .....	114
Figure 64: P, h diagram of the "high load/low head" test cycle conditions [48] .....	115
Figure 65: P, h diagram of the "low load/high head" test cycle conditions [48] .....	116
Figure 66 : P, h diagram of the cycle at 31% load during 1000 h-test [48].....	117
Figure 67: Fluid temperatures during 31% load recurring performance test.....	118
Figure 68: P, h diagram of the cycle at 32% load during 1000 h-test [48].....	119
Figure 69: Fluid temperatures during 32% load recurring performance test.....	120
Figure 70: P, h diagram of the cycle at 49% load during 1000 h-test [48].....	121
Figure 71: Fluid temperatures during 49% load recurring performance test.....	122
Figure 72: P, h diagram of the cycle at 50% load during 1000 h-test [48].....	123
Figure 73: Fluid temperatures during 50% load recurring performance test.....	124
Figure 74: P, h diagram of the cycle at 76% load during 1000 h-test [48].....	125
Figure 75: Fluid temperatures during 76% load recurring performance test .....	126
Figure 76: P, h diagram of the cycle at 85% load during 1000 h-test [48].....	127
Figure 77: Fluid temperatures during 85% load recurring performance test.....	128
Figure 78: P, h diagram of the cycle at 90% load during 1000 h-test [48].....	129
Figure 79: Fluid temperatures during 90% load recurring performance test.....	130
Figure 80: P, h diagram of the cycle at 100% load during 1000 h-test [48].....	131
Figure 81: Fluid temperatures during 100% load recurring performance test.....	132

## LIST OF EQUATIONS

1.1 IPLV for Hongkong .....	33
2.1 NTU .....	45
2.2 Heat exchanger effectiveness.....	45
2.3 Heat exchanger capacity .....	45
2.4 Heat transfer rate.....	45
2.5 Nusselt number on tube side.....	46
2.6 Correction factor j.....	46
2.7 Heat transfer coefficient on tube side .....	46
2.8 Effective cross-sectional area .....	46
2.9 Effective mass flow rate.....	46
2.10 Effective tube diameter .....	46
2.11 Reynolds number on shell side .....	46
2.12 Nusselt number on shell side .....	47
2.13 Heat transfer coefficient on shell side.....	47
2.14 Heat exchanger effectiveness.....	49
2.15 Heat transfer rate.....	49
2.16 Selection of maximal heat transfer rate (chilled water cycle).....	50
2.17 Selection of maximal heat transfer rate (condenser water cycle) .....	50
2.18 Chilled water mass flow.....	51
2.19 Maximum heat transfer rate on chilled water side.....	51
2.20 Maximum heat transfer rate on condenser water loop side .....	52
2.21 Pump head calculation .....	54
3.1 Fahrenheit to Celsius.....	66
3.2 GPM to kg/s .....	66
3.3 Evaporation capacity.....	66
3.4 Load factor .....	66
3.5 Coefficient of performance .....	66
3.6 Efficiency according to AHRI 550/590 .....	67
3.7 Corrected efficiency.....	67

3.8 Degradation correction factor .....	67
3.9 Load factor .....	67
3.10 IPLV.IP .....	67
3.11 Overall heat transfer coefficient.....	75
3.12 Thermal resistance .....	75
3.13 Composition of thermal resistance.....	75
3.14 Isentropic efficiency of compressors with economizer .....	99

## NOMENCLATURE

### *Units*

<i>kW</i>	Kilowatts
<i>TWh</i>	Terra-Watthours
<i>GWh</i>	Giga-Watthours
<i>RT</i>	Refrigeration tons
<i>Btu/h</i>	British thermal units per hour
<i>MMBtu/year</i>	Million British thermal units per year
$^{\circ}\text{C}$	Degree Celsius
$^{\circ}\text{F}$	Degree Fahrenheit
<i>K</i>	Kelvin
<i>m</i>	Meter
<i>cm</i>	Centimeters
$\text{m}^2$	Square meter
<i>in.</i>	Inch
$\text{ft}^2$	Square feet
<i>GPM</i>	Gallons per minute
<i>kg/s</i>	Kilogram per second
<i>hr</i>	Hour
<i>kJ/kg</i>	Kilojoule per kilogram
<i>psi</i>	Pound per square inch
<i>kPa</i>	Kilo-Pascal
<i>ppm</i>	Parts per million
<i>mA</i>	Milliamps
<i>V</i>	Volts
<i>Hz</i>	Hertz

## *Acronyms*

AC	Air-Conditioning
AHRI	Air Conditioning, Heating, and Refrigeration Institute
ALT	Accelerated Life Testing
ANN	Artificial Neural Network
COP	Coefficient of Performance
DBN	Deep Believe Network
DOE	Department of Energy
EIA	Energy Information Agency
EES	Engineering Equation Solver
FDD	Fault Detection and Diagnosis
FR	Flow Rate
GUI	Graphical User Interface
HERL	Ray W. Herrick Laboratories
HNN	Hopfield Neural Network
HVAC&R	Heating, Ventilation, Air-Conditioning, and Refrigeration
HX	Heat Exchanger
IEA	International Energy Agency
IPLV	Integrated Part Load Value
LMTD	Logarithmic Mean Temperature Difference
LSI	Langlier Saturation Index
MTBF	Mean Time Before Failure
PCA	Principal Component Analysis
RPM	Revolutions per Minute
TC	Thermocouple
VSD	Variable Speed Drive

### **Variables**

A	Area, $m^2$ ( $ft^2$ )
B	Baffle distance, $m$ ( $in.$ )
C	Heat capacity rate, $J/K$
C'	Tube spacing, $m$ ( $in.$ )
C <sub>D</sub>	Degradation correction factor, -
c <sub>p</sub>	Specific heat capacity, $kJ/kg\cdot K$
d	Diameter, $m$ ( $in.$ )
G	Effective mass flow rate, $kg/s$
h	Heat transfer coefficient, $W/m^2\cdot K$ ( $Btu/hr\cdot ft^2\cdot ^\circ F$ )
k	Thermal conductivity, $W/m\cdot K$ ( $Btu/hr\cdot ft\cdot ^\circ F$ )
LF	Load factor, %
$\dot{m}$	Mass flow rate, $kg/s$
Nu	Nusselt number, -
P	Pitch, $m$ ( $in.$ )
$\dot{P}$	Power consumption, $kW$
Pr	Prandtl number, -
$\dot{Q}$	Cooling capacity, $kW$ ( $RT$ )
Re	Reynolds number, -
T	Temperature, $^\circ C$ ( $^\circ F$ )
$\Delta T$	Temperature difference, $K$
U	Overall heat transfer unit, $W/m^2\cdot K$ ( $Btu/hr\cdot ft^2\cdot ^\circ F$ )
$\varepsilon$	Effectiveness, %
$\rho$	Density, $kg/m^3$
$\mu$	Dynamic viscosity, $kg/m\cdot s$

### ***Subscripts***

C	Condenser
CH	Chilled water
EV	Evaporator
FL	Full load
Inlet	Value at inlet conditions
max	Maximum
min	Minimum
Outlet	Value at outlet conditions
PL	Part load
S	Shell
s	Isentropic process
iso	Isentropic
T	Tube

### ***Refrigerants***

R-22	Refrigerant nomenclature for Chlorodifluoromethane
R-32	Refrigerant nomenclature for Difluoromethane
R-134a	Refrigerant nomenclature for 1,1,1,2-Tetrafluoroethane
R-410A	Refrigerant nomenclature for a Difluoromethane-Pentafluoroethane Mixture

## ABSTRACT

Environmental challenges, increasing energy costs and demand, and upcoming regulations (e.g., new equipment performance ratings, phase-down of HFCs) are a few of the main drivers behind the research on advanced HVAC&R equipment. The HVAC&R systems are one of the largest energy consumers in both commercial and residential buildings and their operation is essential to ensure thermal comfort as well as other industrial needs. Within this context, large chillers provide chilled water to condition commercial buildings and the new generation of smart chillers feature variable speed compressors that enable active capacity modulation. In turn, variable speed operation along with other factors can contribute to performance degradation. Understanding mechanisms of degradation and developing models that enable predicting the decrease in performance with respect to the rated values are still open topics in the literature.

The overarching goal of this research is to investigate the performance degradation of a water-cooled variable-speed screw chiller under long term operation and to gain insights on the behavior of the chiller under accelerated life testing. In particular, this thesis covers the initial task of designing an experimental test setup that enables performance testing according to the AHRI 550/590 standard. Once the experimental setup was commissioned, a set of four standard-conform baseline tests was conducted to map the rated performance of the chiller at both full and part-load conditions. After completing the baseline tests, an accelerated life test cycle procedure was developed and implemented in order to conduct 24/7 automated testing on the chiller. To this end, two test modes were established to simulate a real-life use of the chiller and induce high level of thermo-mechanical stresses on the compressor. Furthermore, eight recurring baseline tests were conducted to determine the performance behavior after 1000 operating hours. Finally, a preliminary system model was set up. This thesis describes the design of the system, the commissioning and control and provides insights on the performance testing as well as long-term testing methodology and the modeling work that was done so far.

# 1. INTRODUCTION

## 1.1 Motivation

Heating, ventilation, air-conditioning, and refrigeration (HVAC&R) equipment is a key technology when it comes to the reduction of the electrical energy consumption of buildings and to meet the goals of the Paris Agreement on Climate Change to reduce global warming.

This gains special importance facing the raising energy consumption worldwide and, in the United States of Amerika. Between 1990 and 2021 the global total electricity consumption increased by the factor of more than 2.4 from 10,897 *TWh/year* ( $3,718 \cdot 10^7$  *MMBtu/year*) to 26,444 *TWh/year* ( $9,023 \cdot 10^7$  *MMBtu/year*) according to the International Energy Agency (IEA). For the year 2021 alone, the international electricity market recorded an increase of 6.2%. At the same time, the electricity consumption in the United States grew by a factor of almost 1.5 from 2,924 *TWh/year* ( $9,977 \cdot 10^6$  *MMBtu/year*) to 4,312 *TWh/year* ( $1,471 \cdot 10^7$  *MMBtu/year*) and further growth is projected [1,2].

The biggest consumers in terms of total electricity use in 2021 were China, followed by the United States and India [3]. The significant increase can be explained by a fast growth of economy and population, especially in Asian countries such as China or India which were the biggest drivers for the global consumption raise but also the post-covid economic growth in the United States. Another big factor that takes more and more impact on the electricity consumption worldwide is the global warming. Warmer summers and colder winters require more energy for heating and cooling and may lead to an increase by 40% globally by 2030 [4].

This has a huge impact on the biggest electricity consumer in the U.S. which is the sector of buildings that includes commercial and residential buildings. According to the U.S. Department of Energy (DOE), the building sector is responsible for 40% of the primary energy use, while 21% of the primary energy consumption for residential and 38% of the commercial buildings is directly related to refrigeration, ventilation, and space cooling as Figure 1 shows [5; 6]. That is about 10% of the overall electricity use in the U.S. but this is not just a national development [6]. The amount of energy used for air-conditioning (AC) applications doubled between the year 2000 and 2020 and is prospected to continue this trend until at least 2040 [6; 7].

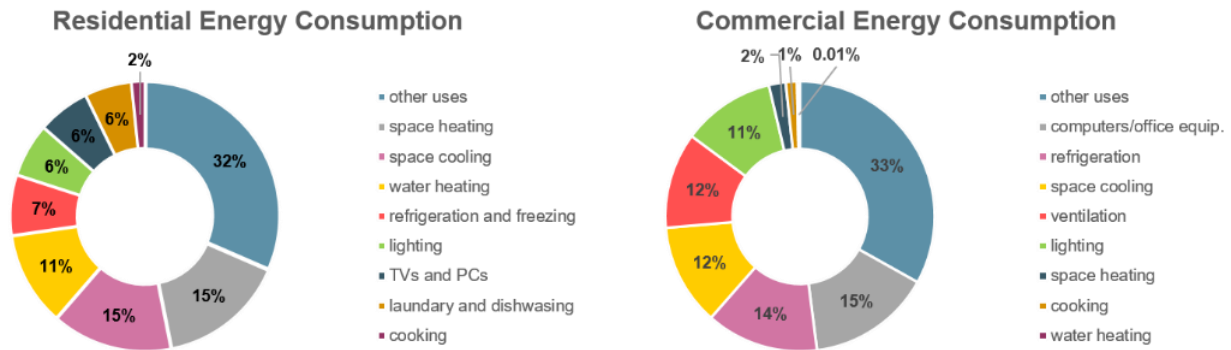


Figure 1: U.S. energy consumption in the building sector (obtained from [7])

The impact of chillers in the building sector is significant despite the fact that chillers are mostly used for commercial applications. It is estimated that chillers provide approximately 60% of the total air conditioning needs for commercial buildings [4]. The Building Energy Data Book [8] states that 31% of the main commercial primary energy use for cooling equipment refers to chillers. A comparison of the given numbers and fractions is not possible in a highly accurate manner since the sources are from different years and countries, some information seem to be outdated on the first look, but the given electricity consumption numbers are sufficient to recognize the clear trend of and increasing electric energy demand in the field heating, ventilation, air-conditioning, and refrigeration for buildings.

Chillers are not just used in the building sector where they mostly provide chilled water for air-conditioning (AC) applications, but also in the industrial cooling. The electricity consumption of refrigeration systems and especially of chillers in U.S. industry cannot be defined very accurate since some industrial manufacturers, especially the ones with a high energy consumption produce their electricity on-site. Published data from the U.S. Energy Information Agency relies on manufacturer surveys [9]. The industries share on the electricity end use in the United States grew just slightly from 14% in 2002 to 15% in 2018 [10]. That means that there was no significant change in the electricity use of the industry. The manufacturer survey report [9] states a general increase of the gross output of 12% for the industry since 1998 while the electrical energy use in the manufacturing industry decreased. Therefore, other electricity consumers increased the cooling demand in the last 23 years such as data centers that have an electricity consumption of  $73 \text{ GWh}$  ( $2,491 \cdot 10^3 \text{ MMBtu}$ ) in 2020 what is 1.7% of the overall end electricity use according to the data

center energy usage report. 43% of that energy is just needed for the operation of cooling and power provision systems [11].

The previous paragraphs show detailed that the impact of chillers on the electrical end energy consumption of the United States is significant. The need in the building sector is consistently increasing while the consumption in the industrial sector appears to be constant with options of an increase. For this reason, it is an important task to further improve the efficiency and operational safety of these systems to reduce energy waste. An enhancement of efficiency and operational safety of refrigeration systems with a deeper focus on screw chillers can have a notable influence on the global primary energy and electricity consumption. This development would not just relieve the climate from additional indirect carbon dioxide emissions and smog due to the energy production but also actually save money for the operators of chillers. In times of sharply increasing energy prices, this is a non-neglectable factor for the competitive position of a company.

During the last decades, there has been a change in the application of large capacity chiller systems due to the ongoing technological developments. For instance, water-cooled screw chillers were replaced in high-capacity applications (about  $>1300\text{ kW}$ ) by centrifugal chillers because of their low vibration level and the lower energy consumption. However, there is still a wide field of applications for water-cooled screw chillers that can for example handle a lower temperature level and that can be controlled easier in part-load operations [12].

Based on the aforementioned challenges, this research work addresses the needs to advance the reliability of water-cooled screw compressor chillers by investigating the performance degradation of a screw chiller in long term operation. The investigated device was a water-cooled variable-speed screw chiller with a capacity of  $145.9\text{ RT}$  ( $513.1\text{ kW}$ ). By gaining a deeper understanding for the performance degradation mechanics of the screw compressor, a model can be developed, that helps to control the chiller within the maximum efficiency. Also, the data can be used to apply predictive maintenance to the refrigeration system and therefore maintain the efficiency high by increasing the operating lifetime. To create a sufficient dataset for a performance degradation model, a performance test stand was designed, and an accelerated life test (ALT) was defined and set up. The related tasks are described in this thesis.

## 1.2 Literature Review

A comprehensive literature review was performed to understand the state of the art in the field of fault detection and diagnostic (FDD) and predictive techniques of performance degradations in HVAC&R equipment. The published literature that is most relevant for this project can be categorized in simulation, impact evaluation, detection, and processing of faults (1), ALT to create a comprehensive data set for a performance degradation investigation (2), and FDD modeling approaches (3). The publications might have overlapping topics at some point, but category was picked based on the impact for this thesis.

### 1.2.1 Simulation, impact evaluation, detection, and processing of faults

Fault detection is a desired feature of chiller manufacturers since controllers and microcontroller were implemented in the systems. Over the years, the complexity of the systems increased rapidly. Striving to detect as many types of faults as possible early on without using sensors that are not fitted by the manufacturer, it is important to identify potential faults, by correlating different variables.

Rossi and Braun [13] provided a general description of a statistical, rule-based fault detection methodology for HVAC systems. Their approach builds up on predefined generic rules that react on the sensor provided inputs like temperature or pressure. Experimental data is not required as a base for this methodology since the sensitivity of the failure detection was evaluated by simulation on a model of a vapor compression system. Rossi and Braun considered the following faults for the FDD tool: low refrigerant charge/leakage, liquid-line restriction, faulty compressor valves, fouling on the condenser and pollution of the filter of the evaporator. The functionality was later tested on a 3-RT (10.55 kW) rooftop air conditioning unit where the faults were installed in different severeness. The susceptibility of the method to error or for inaccuracies is dependent on the used preprocessors which can be simple transformations, characteristic quantities, or models for the thermodynamic relationships.

Groundbreaking work in the simulation of faults on chillers was done when Comstock and Braun [14] developed a FDD tool for chillers with the aim of reducing repairs, timely maintenance, and shorter downtimes for the chiller operators in field applications. The variety of operation modes and simulated faults makes the study outstanding from others. The tool is based on a

comprehensive data set of a 90-RT (31.65 kW) centrifugal chiller (McQuay PEH048J) using R-134a as refrigerant, that includes a variety of 27 operating conditions, both in steady states and transient conditions. Furthermore, the test set does not just represent different load and operating modes but also faulty conditions of different severeness. In his investigative test runs at faulty conditions, Comstock picked a large variety of faults such as a loss of condenser water flow, loss of evaporator water flow, refrigerant leakage but also refrigerant overcharge, the presence of excess oil, condenser fouling, the presence of non-condensable substances in the refrigerant, and a faulty expansion valve. The selection of these specific faults was based on a survey and evaluation of the most frequent and costly faults on screw and centrifugal chillers among U.S. chiller manufacturers that was conducted by Comstock in the initial phase of the project. The simulated faults caused measured efficiency deviations of up to over 20% compared to a normal operating setup.

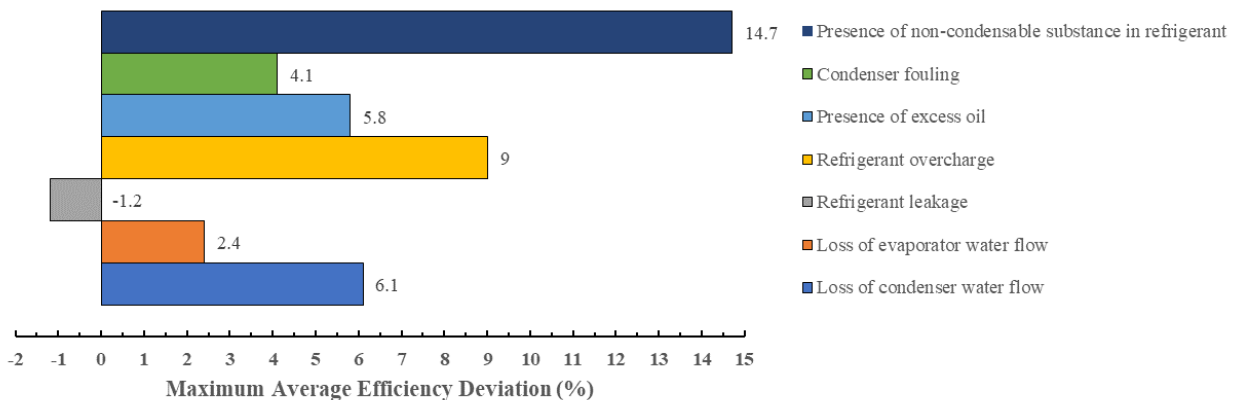


Figure 2: Mean impact on the overall efficiency of the chiller according to Comstock [14]

Based on the findings of Comstock (see Figure 2), it can be concluded that non-condensable components in the refrigerant have the highest impact on efficiency deviations, while a low charge (-10% to -40%) has the lowest efficiency impact. The fault application on the chiller test stand provided detailed insights into the system behavior and reaction on different faults or even multiple faults during operation such as temperature and pressure changes. Therefore, the failure-sensitive variables can be extracted from the data set of the conducted benchmark tests to detect irregularities in the refrigeration system early on. Steady state models of both heat exchangers, the evaporator and the condenser were used to check if the measurements were legit.

Fault analysis of the sensitive variables concluded that all faults could be detected by simple temperature and pressure measurements that are already used for the chiller operation. Simply the distinction between the different faults is hard for some problems. Nevertheless, an adequate diagnosis should be possible as according to the author.

McIntosh et al. [15] created a FDD tool for chillers building up on the work of several previous studies, especially on the model and data of a 5500-ton (19342.69 kW) centrifugal chiller that was set up by Braun et al. [16]. The FDD tool is useful to identify faults, but also to isolate the fault and associate it to a specific component. Besides the heat transfer related faults on a chiller such as reduced (or complete absence of) water flow or heat exchanger fouling, also compressor related faults were investigated and simulated in a model to test the FDD. To this end, the compressor fault could be separated into internal compressor faults and motor/transmission faults. The isentropic efficiency turns out to be the most sensitive variable to detect internal issues on a centrifugal compressor according without relying too significant on the load range of the compressor to McIntosh. For motor or transmission faults, the motor efficiency is defined as the leading characteristic quantity.

Building up on the findings of Comstock and Braun [14], Bendapudi et al. [17] focused on detailed transient modeling of centrifugal chiller to be used for FDD with emphasis on identifying an efficient way of computing the impact of faults on chillers. According to their work [17], transient modeling is more useful than steady-state modeling due to its ability to cover changes that are caused by disturbance in the system during operation such as mode changes and emerging faults. Several different transient approaches for single components, but also for the complete system were investigated and compared. The finite-volume direct solution method was decided to be the most robust approach for the given chiller application. All assumptions and modeling approaches for the components are described step by step in the publication. Furthermore, detailed information about how to address to the impact of faults based on the dataset is given by showing up the correlations between faults and the related fault-sensitive variables such as temperature or pressure. The model was validated and tested extensively with the dataset from a water-cooled 90-RT (316.52 kW) McQuay centrifugal chiller using the refrigerant R-134a. The data, collected by Comstock and Braun [14] was used since it covers a high range of operating modes and faults as mentioned earlier in this chapter.

Most FDD approaches and tools assume that there is just one fault or system issue coming up at a time which makes the detection easier predictable. In real fault situations that might not always be the case since especially a severe compressor or heat exchanger fault brings several other issues with it. Existing FDD solutions often run into issues at this point. Even more important is it, to find correlations for multiple-fault situations.

Li and Braun [18] tried to address this problem in their work and developed a methodology for diagnosing multiple simultaneous faults in vapor-compression systems. As Figure 3 shows, the correlation and interactions of different fault types and the related system state variables were investigated. To simplify the pattern, the fault types were assigned to either the component level fault category or the system level fault category. To enable a correlation between operating variables dependent on the operating mode and faults on system and component level, decoupling features and virtual sensors were applied, *e.g.*, to identify refrigerant charge faults. Finally, the model was trained to detect faults on a more dimensional level to be able to detect several faults that occur at the same time. For the validation and adjustment of the sensitivity of the tool, a 5-RT (17.58 kW) rooftop unit using R-22 with fixed-speed scroll compressor was used. In the experimental setup, the tool was able to detect faults before they caused 5% cooling capacity decrease.

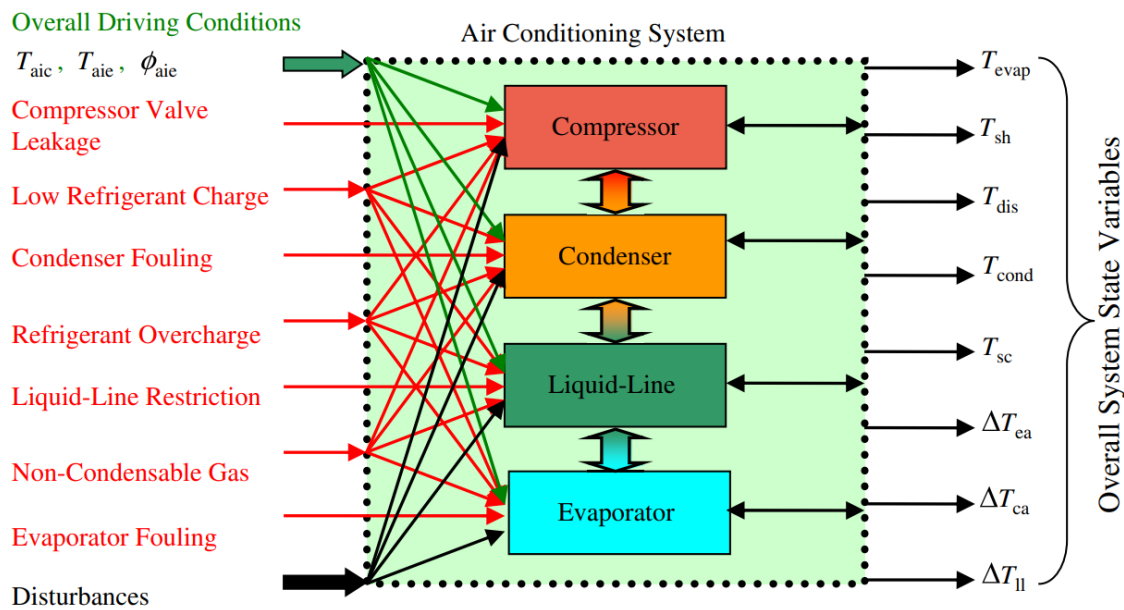


Figure 3: Impact and correlation of faults on the components of a chiller (obtained from [18])

Zhou et al. [19] studied fault detection and diagnosis for different HVAC sub-systems on a system level. Therefore, they defined the different sub-systems of a chiller plant like pumps, heat exchangers and the chillers itself. Furthermore, baselines were created for all components, and fault sensitive sensor values, or performance indices how they are called in the paper, were defined for every sub-system. Typical faults that were included in the model include fan motor degradation for the cooling tower system, compressor motor degradation and heat exchanger fouling for the chiller, partial clog in the pipe and pump for the pump system and tube fouling for the heat exchanger system. An overall system model was created based on several individual component models from various researchers to perform the FDD. The FDD model was applied to a chiller plant consisting of six chillers of 7230 kW each that was also used for the tool tuning and validation. The tests showed that the model was not just able to detect system and sub-system faults but also to rate the level of severeness of a fault and was therefore rated sufficient. However, since the accuracy of the model relies on accuracy of the sensors, the authors suggest that this factor should always be taken into consideration.

Beghi et al. [20] proposed a principal component analysis (PCA) for a semi-supervised data driven FDD algorithm to increase the energy efficiency of HVAC equipment and reduce the operating cost at the same time. The algorithm detects abnormal operating conditions and characterizes potential faults based on the sensitive variables. The sensitive variables are a collection of features mentioned in elaborations of Comstock and Braun [14], McIntosh et al. [15] and Bendapudi et al. [17] augmented by additional defined variables. The tool considers the following 10 characteristics as markers for faults:

- Evaporator water temperature difference
- Refrigerant suction superheat temperature
- Refrigerant discharge superheat temperature
- Condenser approach temperature
- Evaporator approach temperature
- Overall evaporator heat loss coefficient
- Polytropic efficiency of the compressor
- Isentropic efficiency of the compressor
- Expansion valve blockage coefficient
- Calculated compressor efficiency

A matrix connects all faults to the related characteristics and the severeness of a fault. For an assessment of the applicability and a tuning of the tool, it was tested satisfying on about 200 data sets of air-cooled water chillers with two types of R-134a compressors. One with a frictionless turbo compressor and a cooling capacity of 209 kW and another one with a for a screw compressor and a cooling capacity of 220 kW. The FDD model is applied to the centrifugal chiller for a reduces evaporator water flow and a refrigerant leak and to the screw chiller for a reduced condenser air flow and a reduced compressor efficiency.

Hjortland et al. [21] applied FDD for common faults on fixed speed and variable speed rooftop air conditioning units to optimize service intervals. The published study does not just focus on the impact of faults over time but also includes a techno-economic analysis that allows a condition-based maintenance strategy to reduce the operational costs and lifetime costs of the product. Therefore, a semi-empirical component-based modeling approach was used to simulate the performance of a system and the impact of faults on the system performance. The major investigation and simulation were on heat exchanger fouling and incorrect refrigerant charge. Also, combinations of those faults were investigated. The model is based on data that was collected under optimum conditions in psychrometric chambers as well as on data from non-optimum conditions without psychrometric chamber and achieves an accuracy of 10% of the measured fault impacts. All experimental data for the study was measured on a 5-RT (17.58 kW) R-410A multi-stage roof top unit with scroll compressor and finned-tube heat exchangers. Finally, a data-driven artificial neural network model (ANN) of such a roof top unit could be developed to simulate different faults with varying impact on the system. The ANN was combined with a building model to test the application of the FDD to optimize the overall operational cost of the system. The simulations that were ran for an optimization problem underpinned the financial advantage of the condition-based strategy over periodic maintenance intervals.

Chiller FDD methods often rely on rudimentary values that are tracked by almost every chiller like fluid temperatures and pressures. This way, the engineers want to enable a use in all chillers or even a potential retrofit by a simple software update. Another approach, to measure faults or wear of the mechanical components of a system and the associated mechanical power loss is to add more sensors such as accelerometers to detect vibrations. Even if that is not common practice for chillers in field applications yet, it is for other applications that use rotary machines. Meslameni and Kamoun [22] applied vibrations diagnostics to an air screw compressor to detect

potential imbalance faults on a screw compressor. This is a fault type that not directly causes issues but can lead to additional wear a shorter lifetime of bearings and the screw surfaces due to cylindrical vibrations. An extensive investigation of the vibrations on a screw compressor was used to create a probability driven FDD tool. Therefore, mobile accelerometers were mounted on all mechanical bearing points of the compressor which is on both ends of each screw and on the bearings of the electric motor as shown in Figure 4. The used dual-screw air compressor has a nominal power draw of 45 kW at 2940 rpm. Since there is always a certain imbalance on mechanical manufactured rotary parts, the measured values were compared with the ISO 10816 standard that defines thresholds to estimate the acceptability of a vibration or in this case imbalance. In the investigated case, the model and analysis tool could be used to detect an imbalance that led to an on-site balancing to fix that issue.

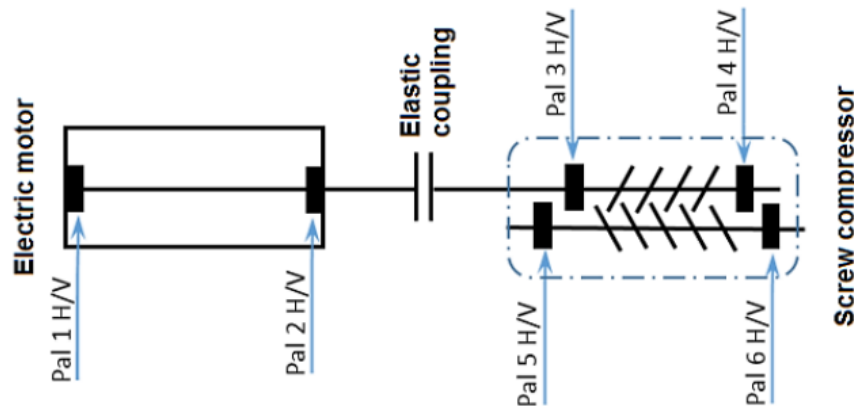


Figure 4: Positions to mount accelerometers on a screw compressor (obtained from [22])

Summarizing there can be said that a system needs to be investigated intensively first. Sub-systems and components must be defined, and potential failures must be studied for each sub-system. All defined faults need include correlations that show how they can be measured or tracked, even in multiple-fault scenarios. Based on this, algorithms can help to detect, isolate and identify faults.

Nowadays, chiller can detect regular faults and even in situations in which multiple faults occur. The literature review showed that significant work has been done on that topic. However, one fault that is not sufficiently investigated so far is the performance degradation of a chiller over time. This may not be a fault that affects operational safety in the first place, but it affects operational costs and efficiency of the whole system and should therefore be considered.

### 1.2.2 Accelerated life testing

To track performance degradation over time a comprehensive dataset is necessary. The dataset should display the change of the chiller efficiency over time. Since chillers are industrial products and therefore are usually designed for life spans for 15 years or more, a study in regular operation would demand more time that is available for most projects. A solution for that issue is the accelerated life testing. ALT allows to increase the mechanical aging and wear process of a product due to extreme, predefined operating conditions and test cycles. A literature review was executed to investigate the details of ALT and get an impression of procedures and test cycles. Since there was no available source which described the tests for screw chillers, the focus was set on ALT in general and work that was done on refrigeration cycles and compressors.

Miller and Nelson [23] studied stress based accelerated life testing, where all units were run to a failure. Therefore, they applied overstress testing with high temperature, voltage, pressure, vibration, cycling rate, and load to the test units. Two different test modes were explained further. One is the constant stress mode where an increased failure rate due to constant stress is assumed and the system or the device is run under constant high stress conditions. The second mode is the step stress operation. In this mode, the test unit is exposed to a low stress level initially. After a specified time, the stress level is increased. This can be done in several clearly defined time and stress steps, until the load increase leads to a system failure. The step stress mode is useful if the maximum value for a stress test cannot be defined or is hard to estimate. The disadvantage of the step stress mode is that a model is needed to relate the different stress stages to an actual lifetime. Based on an example, Miller and Nelson [23] showed how a step stress test can be designed, how big the necessary sample size needs to be, and how advanced modeling helped them to decide between different test approaches.

Pruitt, Davis, and Ross [24] provided a review of evaluated methods for accelerated life tests for a cryocooler with a design life span of 10,000 *hr* or more than 10 *years*. Driver for the evaluation was that the airborne and spaceborne application of the cryocooler where very little or no maintenance and repair is possible and at the same time, a high reliability of the system operation is required. On the same side, it is usually not possible to test and proof the fault-free lifecycle within the design process. The authors separate the failures of a system into three time-dependent phases which are infant mortality, that happens right at the beginning of the operation based on workmanship issues and material defects and become less, the more operating hours a

system accumulates. The second phase is characterized by a generally low failure rate where mostly random failures occur. And finally, the third phase which is the wear out phase when the system is confronted with a peak of failures based on the wear of components which reach their maximum designed lifetime. The exact time-based definition as displayed in Figure 5 refers to the investigated cryocooler, but the three defined phases can potentially be transferred to most other products such as compressors.

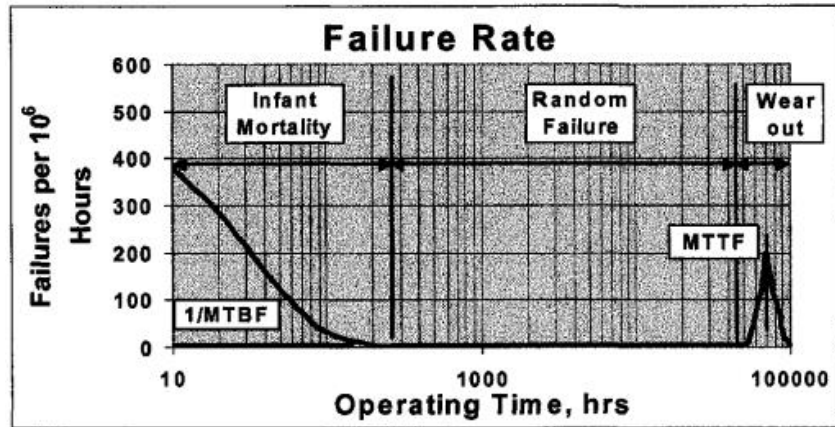


Figure 5: Representative failure rate for mechanical systems (obtained from [24])

One described accelerated life test approaches base on test series with a statistically significant number of identical units that are tested past the infant mortality phase. With a statistical approach, the so-called mean time before failure (MTBF) can be calculated. This method is just partly sufficient since just the first failure phase is covered properly. Even though this phase provides a high failure probability, those are not lifetime limiting. A second test type was developed in cooperation with the Air Force Research Lab where several cryocoolers were instrumented and undergo 24/7 long-term testing at predefined conditions and steady state operations that are just interrupted by recurring performance tests to compare the current operational data and efficiency with the initially measured baseline data set. The cryocooler is run on this mode until it provides a certain amount of predefined failure data. An accelerated dynamic stress testing works with different levels of vibrations that affect the system. Based on the amplitude and the severeness of the vibration, the lifetime test can be reduced from 12,000 *hr* to 945 *hr*. During the accelerated thermal stress testing, the chiller was operated in extreme operating modes that were aiming for a faster degradation of material. For this test, the authors just mention

a predictable increase of the failure rate and mechanical wear based on temperature changes that results in a higher-pressure difference. According to the paper, wear should already be quantifiable after 1000 *hr* to 4000 *hr*.

Jayatilleka [25] studied life cycle designs and ALT in his publication. The work focused on household equipment but also HVAC equipment. According to the authors findings, so called seasonal functional usage duty cycles must be defined for HVAC units which means that certain cycles or patterns like starts and stops, or total number of revolutions must be identified for the investigated product. Furthermore, a decomposition of the system into subsystems is suggested to identify the components that are prone to fail, *e.g.*, a bearing or operating modes that lead to a failure over time *e. g.* start-stop cycles. The complexity of an analysis for HVAC equipment was shown on the example for a 500-RT (1,754.43 kW) chiller for a building in Houston, TX. The analysis of the chiller was supported by an EnergyPlus model that provides mechanical data like compressor shaft speed versus time based on the power input and electrical data like switching frequency vs. temperature increase. Then, the model data was used to gain the number of thermal cycles in a product life range by simple multiplication. Therefore, it is important to know or define the specific product parameters that are expected. Drivers for the expectations can be very manifold but they are mostly driven by customer expectations as Jayatilleka states. The described examples for accelerated life tests mostly focused on the identified components of the subsystems or problematic operation modes.

The literature review showed that the important role of an accelerated life test is to define or to estimate the lifetime of the chiller. In the next step, operating modes or cycles can be defined as they would occur in normal operation too such as start-stop intervals. The operating modes can, but do not necessarily have to be in high stress operating modes. By relating the number of this cycles in under field conditions to the number of cycles under test conditions, the accelerated life can be calculated.

### **1.2.3 FDD modeling**

Previous research efforts reported in the literature focused both on developing transient models of chillers and on implementing automated fault detection and diagnosis (FDD) approaches (either model-based or data-driven) to monitor the health state of a chiller and predict maintenance requirements or detect anomalies during its operation. Data-driven modeling relies on historical

data of the equipment and can be quite powerful in identifying emerging behaviors based on data patterns of the chiller. In the literature, only a limited number of studies deals with time-dependent performance analysis of chillers and prediction of performance degradation.

For instance, Browne and Bansal [26] developed a transient simulation model employing a thermal capacitance approach for chillers with screw compressors to investigate optimal control strategies and implement FDD algorithms under transient conditions. The model was validated by the experimental data of two different chiller setups, a 185-*RT*-chiller (650.6 *kW*) with single-screw compressor using the refrigerant R-22 and an 85-*RT*-chiller (298.9 *kW*) with a twin-screw compressor with the refrigerant R-134a, respectively. Using this very different chillers with modulating and on/off-control for the validation and tuning of the model ensures the possibility of a precise dynamic performance prediction on a wide range applicability in this field.

Fu and Ding [27] follow a two-stage approach by first showing a steady-state simulation model development and validation for a Shanghai Yileng Carrier screw liquid chiller with and without economizer using R-134a as a working fluid in their paper. Based on that model, an analysis of configuration parameters was made which affect the performance of a chiller in full and part load conditions at most.

Subsequently the work was augmented by Fu and Ding [28] with a dynamic model of an air-to-water dual mode heat pump with a screw compressor in the second modeling step which is closer to the real-life application of a chiller. The dynamic simulation used predictor-corrector and integration step methods to predict the capacities and compressor work inputs of the system within 10% of the empirical collected data [27]. The validated dynamic model for further employed to analyze the performance at off-design conditions with a wide range of condensation temperatures [29]. A technical solution was introduced to overcome the problem of decreasing capacity at low condensation pressure by bypassing the thermostatic expansion valve in parallel with an auxiliary capillary tube to increase the superheat. Furthermore, a fan control strategy was implemented on the air-to-refrigerant heat exchanger that was used as the condenser. A field study was conducted to monitor year-long performance of a chiller installed in Shanghai that is in operation over a whole year.

Besides physics-based modeling techniques, researchers have proposed data-driven model to better capture the dynamic behaviors of chillers. Among data-driven models, Artificial Neural Networks (ANNs) have been employed in a wide range of engineering and scientific fields.

Chang [30] applied a Hopfield Neural Network (HNN) model on a centrifugal chiller plant to calculate the best optimal chiller loading as well as the best load distribution. A special feature of the HNN model is that it does not rely on an operating data memory with whole load patterns but remembers characteristics from training examples. To verify the capabilities of the HNN, the trained model was applied in different customized versions for a four-chiller-system of an office building and a six-chiller-system of a semi-conductor factory. The water-cooled chillers have cooling capacities of between 960 *RT* and 1,440 *RT* (between 3,376.2 *kW* and 5,064.3 *kW*). In the test application, a reduction of the energy consumption of between 1.02% to 8.60% depending on operation and load range could be achieved. Lee and Lu [31] presented an all-statistical based solution for the performance prediction of chillers. They used the large dataset from over 1000 chillers to provide six models with different application and calculation approaches. The models were mainly based on the water side temperatures and the flow rates which are made usable as factors and parameters by regression methods. The database reflected a wide range of operating conditions and was a broad mix of test data, field test data and manufacturer data. The model was not validated on a test or field system, but the calculated root mean square error in comparison to the data base is 2.20%.

Recent papers, such as Tian et al. [32] focus their evaluation on COP prediction to optimize the systems efficiency and aligned with that, the energy consumption of their investigated chiller. Therefore, they create an artificial neural model (ANN) using Levenberg-Marquardt-algorithm with the target to gain a higher accuracy in their efficiency prediction than commonly known modeling approaches. The ANN is based on two main processes which are training and learning what combines the approaches described by Chang [30] as well as Lee et al. [31]. Training means an adjustment by previously known, measured data. An available on-site system provided the data base for model. Learning means an on-site prediction process that uses a back propagation algorithm to establish a COP model. The back propagation algorithm was able to estimate the operating behavior of the chiller by detecting load and performance patterns from previously recorded empirical test data. This procedure is also known as comparison and cross-validation test run. Tian et al. [32] also introduced the tests that were done to certify a validity of the efficiency prediction within almost  $\pm 5\%$  (maximum deviation 5.8%). For the validation, a water-cooled variable frequency screw water chiller was tested in different operating conditions but with a focus

on a part load of 75%-85% which is the main operating range. The chiller was a Carrier 30XWV-303 providing a cooling capacity of 300 *RT* (1,055.1 *kW*) using the refrigerant R-134a.

The predictive model of Sala-Cardoso et al. [33] also relied on a neural network learning methodology that is supplemented by a hybrid load forecasting scheme. The thermal demand forecasting calculated the load profiles based on a performance map and a multi-layer pre-training strategy of the overall system. The model was validated with a chiller installed in a 2,400 *m*<sup>2</sup> (25,833 *ft*<sup>2</sup>) campus building in Barcelona, Spain. During the field demonstration of the algorithm with chillers of a thermal capacity of between 34 *RT* and 122 *RT* (between 119.6 *kW* and 429 *kW*) that are operating together in a multi chiller plant, an average performance gain of 19.54% to the initial controller could be achieved.

Zhu et al. [34] proposed a deep learning-based model using a deep believe network (DBN). They developed a library of operating conditions to recognize patterns in the chiller operations by working with density clustering. A water-cooled screw chiller with a rated capacity of 100 *RT* (351.7 *kW*) and R-22 as refrigerant is used to create a database and to validate the model. The model was capable of evaluating and analyzing failures and performance changes of the refrigeration system by using numerous statistical and machine learning algorithms. Those findings can for example be used to further generate predictive maintenance algorithms or to adjust the machine use to the remaining capacity.

Bao et al. [35] pointed out that today's research cannot just focus on the modeling aspects, but also needs a reliable and precise database which is important to create and validate accurate models. Their development of a Hong Kong-specific integrated part load value (IPLV) to rate the performance and efficiency of cooling and refrigeration systems in that area is an important step to precise the data base. For the Hong Kong-specific IPLV, they do not define a whole new formula but adjust the weighting of the load ranges based on real building operations as you can see in Formula 1. As common for IPLV equations the letters A, B, C, and D in this equation represent the test load ranges of 100%, 75%, 50%, and 25% of the full load capacity. The new part is the numerator over the letter. These values are adjusted to the annual fraction of this load range specifically for Hong Kong.

$$\text{IPLV}_{\text{Hong Kong}} = \frac{1}{\frac{0.012}{A} + \frac{0.682}{B} + \frac{0.257}{C} + \frac{0.049}{D}} \quad (1.1)$$

To calculate this numerators, 20 buildings systems were investigated after their representativeness was verified by a statistical analysis using regression methods like the Monte Carlo analysis. Aim of the local IPLV is to avoid the need of a chiller simulation for specified comparisons by just using this local value.

The cited literature provides a general overview of the trends in approaches for modeling of transients of chillers in the past twenty years. A combination of detailed dynamic modeling and reduced order models have been proposed to predict time-varying performance of chillers. Recent studies combined the empirically based simulation models with the probability calculation and focus on training which is based on the empirical data which is usually measured in standardized load ranges as well as on learning which allows the chiller to optimize its operation and gain a higher efficiency in the installed operation [19]. This combination provides the possibility of a manufacturer provided efficiency optimization with the possibility of a customization within the application. This approach can be supplemented by different preselected application parameters [33]. The transient models help to create algorithms to predict the performance degradation or to perform FDD.

All findings of the literature review above have in common, that their described performance or efficiency calculation just provides a short-term forecast that only focusses on the system-based load characteristics like daily performance curves, chiller maps or regular upcoming peaks [26]. Complex phenomena such the performance degradation of the compressors due to mechanical friction and torque in long-term operation have not been investigated thus far. The research on emerging behaviors and prognostics is still wide open. A long-term performance degradation study is needed to gain a more detailed understanding of the performance degradation characteristics and mechanics of a chiller. The investigation should include a time-based operation in different load and operation modes as they can or could appear in a real-life application without any performance reducing modification on the chiller system itself. To further improve the chiller controls and to provide deeper insight in the mechanical condition of the compressor, the data collected can be analyzed in real-time and used for either more energy efficient operation or also in fields like predictive maintenance and life-time prediction. This is especially interesting facing the fact early recognized faults in a chiller can reduce the repair costs by 26% [34].

### 1.3 Thesis objectives and approach

The approach presented in this thesis focuses on the first step of this task that main target is to build up a data base that can be used as foundation for an accurate performance degradation model. The work starts with the setup of a test stand that is capable to perform long-term test runs as well as standard conform baseline tests that can be used as a reference for later performance degradations. Test modes must be developed for the long-term tests which reflect a wide variety of operation modes as they could occur in real life applications too.

The setup of the test system was the first main task that needed to be conducted. Aim was a test stand that is capable of performing baseline tests according to the AHRI 550/590 standard with the delivered water-cooled screw chiller. A part of the system was already existing from a former project where a 90 *RT* centrifugal chiller (316.5 *kW*) was investigated. That was positive on the one side since the overall system scheme was already existing, on the other side, it was hard to correctly size and install new components. At the beginning of the work, a thermodynamic model of the system and the components was created. Due to a lack of information especially for older components like valves and some heat exchangers, this needed to be done in two steps. The system first needed to get running and then, the component models could be adjusted or corrected by the gained operational data. In the second step all components were re-calculated and sized correctly.

After the system was set up, it could be commissioned and prepared for the baseline and long-term operation. This included a calibration of the thermocouples but also an adjustment of the operating valves that are used for water flow, cooling load, and temperature control in the system. Also, here it was important that the test stand can fulfill the accuracy requirements of the AHRI standard. At a later stage, the commissioning also included the testing and implementation of the accelerated life testing modes at the test stand which included smaller adjustments and tuning on the test stand.

Once the system operated as intended, an initial baseline test was conducted according to the requirements of the standard AHRI 550/590. The tests are needed to gain a capacity and performance baseline of the chiller as a base for all further performance degradation investigations. To gain this baseline, steady-state tests in the load ranges of 25%, 50%, 75% and 100% load need to be conducted. Since the investigated chiller has an operational safety function that shuts down the chiller at loads below 30%, the 25% test run was set higher. After the tests were finished, an

analysis was done that interpolated/extrapolated the test values according to the AHRI standard and the baseline was created. In addition, the integrated part load value was calculated. The IPLV gives feedback over the efficiency of the chiller in part load operation. At the end of the analysis, the calculated values were compared to the information in the manufacturer's specification.

After the baseline tests were conducted, the focus was on the development of an accelerated life testing mode for the chiller. A sufficient accelerated life test was not available in literature, so an own test mode was created. The test mode consists of operating conditions that could occur during the chiller operation without manipulating the refrigeration system. To accelerate the life cycle of the device during the test the operating modes were selected in a way that they were not ideal for the chiller. Here it was important to find an operating mode where the lubrication pressure is low, or the fraction and mechanical stress is the highest. Two test modes could fulfill these requirements. These are explained in this thesis. The test modes are switched in regular intervals.

While the accelerated life testing is conducted for several weeks. The test modes are interrupted by recurring baseline test. This baseline tests and the measured performance degradation give an update on the current condition of the chiller and the screw compressor. By inserting the baseline tests between the accelerated-life test modes of the chiller, they create an ongoing picture of the performance behavior over time.

This thesis is organized five main chapters that describe the work progress over time. Chapter 1 provides background to the conducted research by showing the motivation that led to the project and as well as a detailed literature review on research in this field. Also, it includes a description of the work approach. Chapter 2 focusses on the test stand and the chiller itself. Beginning with an introduction of the water-cooled screw chiller in the system. This is followed by an explanation of the first generation of the system and the problems that came with it as well as the current, second generation of the system with a detailed overview of the used components and the system scheme. Also, the water quality testing that impacts the test system accuracy is explained. In Chapter 3, the tests that were conducted on the chiller test stand are explained, the standard conform analysis is displayed and the results are shown for the baseline testing as well as for the accelerated life testing and the first recurring performance test. Chapter 4 gives an overview of the modeling work done so far. Finally, Chapter 5 concludes the work and gives an outlook for the next steps of the research project especially into the continuation of the accelerated life testing and the dynamic modeling.

## 2. DESIGN OF THE TEST SYSTEM

### 2.1 Selection of a water-cooled screw chiller

The main object of this study is to conduct an accelerated performance degradation study on a water-cooled variable speed chiller featuring an oil-injected twin-screw compressor typically employed in space conditioning of commercial buildings as well as cooling of process water streams. In a nutshell, chillers are vapor compression systems that provide chilled water at the desired temperature setpoints. Chillers also be used as heat pumps to provide warm water supply for heating applications, but this research work focuses on cooling applications. Commercially available chillers can feature both positive displacement and centrifugal compressor types depending on the capacity range and designs, but the scope of this research is limited to positive displacement compressors. To select a chiller to be tested at the Herrick Labs, the following criteria have been identified:

- it was important to acquire a state-of-the-art variable-speed chiller available with a capacity range below 150 *RT* (527.5 *kW*) in water chilling mode.
- The selected chiller should be able to be integrated within an existing test apparatus that was previously employed to conduct experimental work on a 90 *RT* centrifugal chiller (316.4 *kW*) [14]
- It was desired to procure a chiller with ice making capabilities to provide a greater range of operating conditions that could be tested during the accelerated life testing.

Based on these reasonings, a York YVWA water-cooled variable speed twin-screw chiller has been selected. The chiller employed refrigerant R-134a with a nominal rated capacity of 145.9 *RT* (513.1 *kW*) in the regular water chilling mode and 97 *RT* (314.1 *kW*) in a special ice making mode with lower water temperatures. Table 1 provides an overview of the operating conditions and nominal performance and Table 2 reports the nominal performance in water chilling mode at the AHRI conditions. Figure 6 shows the physical setup of the chiller.

Table 1: Operating conditions and nominal performance [36]

Evaporator Data			Condenser Data			Performance Data	
EWT (°F)	32.00		EWT (°F)	88.00		Full Load Efficiency (kW/ton.R)	0.9805
LWT (°F)	25.00		LWT (°F)	94.30		NPLV.IP (kW/ton.R)	0.6643
Flow (USGPM)	356.1		Flow (USGPM)	475.0		Heat Rejection (MBH)	1489
Pressure Drop (ft H2O)	8.68		Pressure Drop (ft H2O)	9.31		Physical Data	
Fluid	Ethylene Glycol (%)	20	Fluid	Water		Rigging Wt. (lb)	7727
Fouling Factor (h.ft <sup>2</sup> .F/Btu)	0.000100		Fouling Factor (h.ft <sup>2</sup> .F/Btu)	0.000100		Operating Wt. (lb)	8367
Fluid Volume (USGAL)	46.00		Fluid Volume (USGAL)	44.00		Refrigerant Charge (lb)	280
Min Fluid Flow Rate (USGPM)	280.0		Min Fluid Flow Rate (USGPM)	240.0		Length (in)	116.6
Max Fluid Flow Rate (USGPM)	870.0		Max Fluid Flow Rate (USGPM)	910.0		Width (in)	55.6
Evap Type	Hybrid Falling Film		Cond Type	Water Cooled Condenser		Height (in)	72.7
Chiller Type	Water Cooled VSD Screw		Compressor Type	VSD Screw - Semi Hermetic			
Number Passes	2		Number Passes	2			

Table 2: Nominal performance under AHRI 550/590 test conditions [36]

Performance at AHRI Conditions					
Evaporator Data		Condenser Data		Performance Data	
EWT (°F)	54.00	EWT (°F)	85.00	Full Load Efficiency (kW/ton.R)	0.6610
LWT (°F)	44.00	LWT (°F)	94.30	IPLV.IP (kW/ton.R)	0.3996
Flow Rate (USGPM)	349.1	Flow Rate (USGPM)	449.3	Heat Rejection (MBH)	2079
Pressure Drop (ft H2O)	8.31	Pressure Drop (ft H2O)	8.46	Cooling Capacity (ton.R)	145.9
Fluid	Water	Fluid	Water		
Fouling Factor (h.ft <sup>2</sup> .F/Btu)	0.000100	Fouling Factor (h.ft <sup>2</sup> .F/Btu)	0.000250		
Fluid Volume (USGAL)	46.00	Fluid Volume (USGAL)	44.00		



Figure 6: Physical setup of the York YVWA chiller [37]

A schematic of the York YVWA series chillers vapor compression cycle is shown in. The numbers in the following description refer to the state points in this figure. Generally, the cycle is not very complex since it is realized within a small physical space. The main component of the cycle is the direct-drive semi-hermetic rotary screw compressor which is has a speed control by a frequency inverter that gets a load related signal from the main control of the chiller. For a simplified maintenance, the compressor has a ball valve at the inlet and outlet side. The compressor raises the refrigerant pressure from evaporation to condensation level (1→2). After the compression, the refrigerant-oil-mix is separated in the centrifugal oil separator (2→3) to avoid the transport of oil into the system and especially in the heat exchangers. The oil is returned to the compressor while the refrigerant is liquified in the condenser (3→4) which is designed as water-refrigerant shell and tube heat exchanger. The water flows through the pipes while the refrigerant condenses in the shell. The heat exchanger has a discharge gas baffle to reduce the gas flow through the heat exchanger and a sub-cooling part. After subcooling in the economizer plate which is a heat exchanger (4→5), the main part of the refrigerant is then expanded by an electronic expansion valve (5→6) into an evaporator (6→1) that is also a shell and tube heat exchanger. The evaporator is a partly flooded falling-film heat exchanger to reduce the refrigerant charge [37]. The refrigerant vapor leaves the evaporator through the suction line in the compressor (1). A fraction of the refrigerant is expanded in the economizer (4→7) where the evaporation (7→8) is used for subcooling the refrigerant in the liquid line to raise the system efficiency before it returns to the compressor (8).

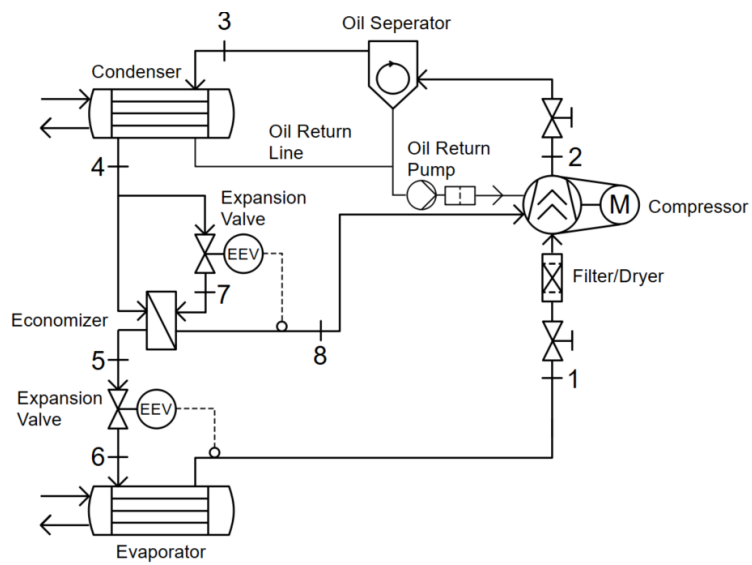


Figure 7: Simplified refrigeration cycle of the York YVWA chiller series

## 2.2 Development of the test stand design within setup steps

### 2.2.1 Overview and original test setup

A new test stand is designed and build up in the east wing of the old Herrick Labs building (HERL) at Purdue University to simulate various loading conditions and collect chiller performance data. The test facility includes a new selected water-cooled variable speed screw chiller. The new experimental setup leveraged the cycle configuration and several major components of an existing experimental system developed in the 1990's to test a 90 *RT* centrifugal chiller [14]. As illustrated in Figure 8, the water in the condenser loop was passed a fixed speed pump right after the chiller exit (C1→C2) which provided a flow of 270 *GPM* to the condenser. From there it entered the chilled water heat exchanger (C2→C3). to dissipate the heat that was added to the system by the compressor. After passing the flow meter, the working fluid passes the regenerative heat exchanger (C4→C5). The experimental setup used a single shell and tube heat exchanger to transfer heat between the closed condenser water and evaporator water loops. This regenerative heat exchanger allowed to provide enough load to the chiller evaporator to reach the rate cooling capacity. A bypass line (C3→C6) was installed in the condenser water loop to bypass the regenerative heat exchanger. Control of the flow through the bypass line provided control over the loading condition. This load control was realized by a three-way valve (C5/C6→C7) and a flow control valve (C7→C8). In the evaporator water loop, the water also first passed the pump (E1→E2) after exiting the chiller. The fixed speed pump provided a flow of 216 *GPM* to the evaporator. The flow rate could be adjusted by a motor valve (E2→E3) before the liquid entered the regenerative heat exchanger (E3→E4). A hot water cycle could provide additional load (E4→E5) to the system before the water flowed back to the evaporator inlet. Water supplied by the city utility system and steam provided by the heating system of the laboratory were used to provide additional means of capacity control. Water was used to reject the heat load generated (CH1→CH2) by the compressor and to precisely control the condenser water return temperature. This city water was discarded down the drain after passing through the shell and tube heat exchanger to cool the condenser water; as a result, the centrifugal chiller experimental system used significant amounts of city water. The steam (ST1→ST2) was used to provide additional heat input to the evaporator water loop and could be used to rapidly increase the loading condition on the chiller. An intermediate loop circulated hot water between the evaporator water loop and the steam

heat exchanger. The design process begins with an in-depth review of the existing experimental system and with a check of what components could be potentially repurposed for the new system design. Shell and tube heat exchangers were used exclusively throughout the design of the system and the system was plumbed primarily with DN4 schedule 80 PVC pipe. Further components were the two fixed speed pumps of the evaporator and the condenser loop as well as a third fixed speed pump that was used to circulate water between the steam heat exchanger and the chilled water heat exchanger. The test stand design also aimed for a reuse of the given motor valves.

After reviewing the existing system, a new test stand design is generated based on thermodynamic calculations. The numerical results were used to size and select the different components.

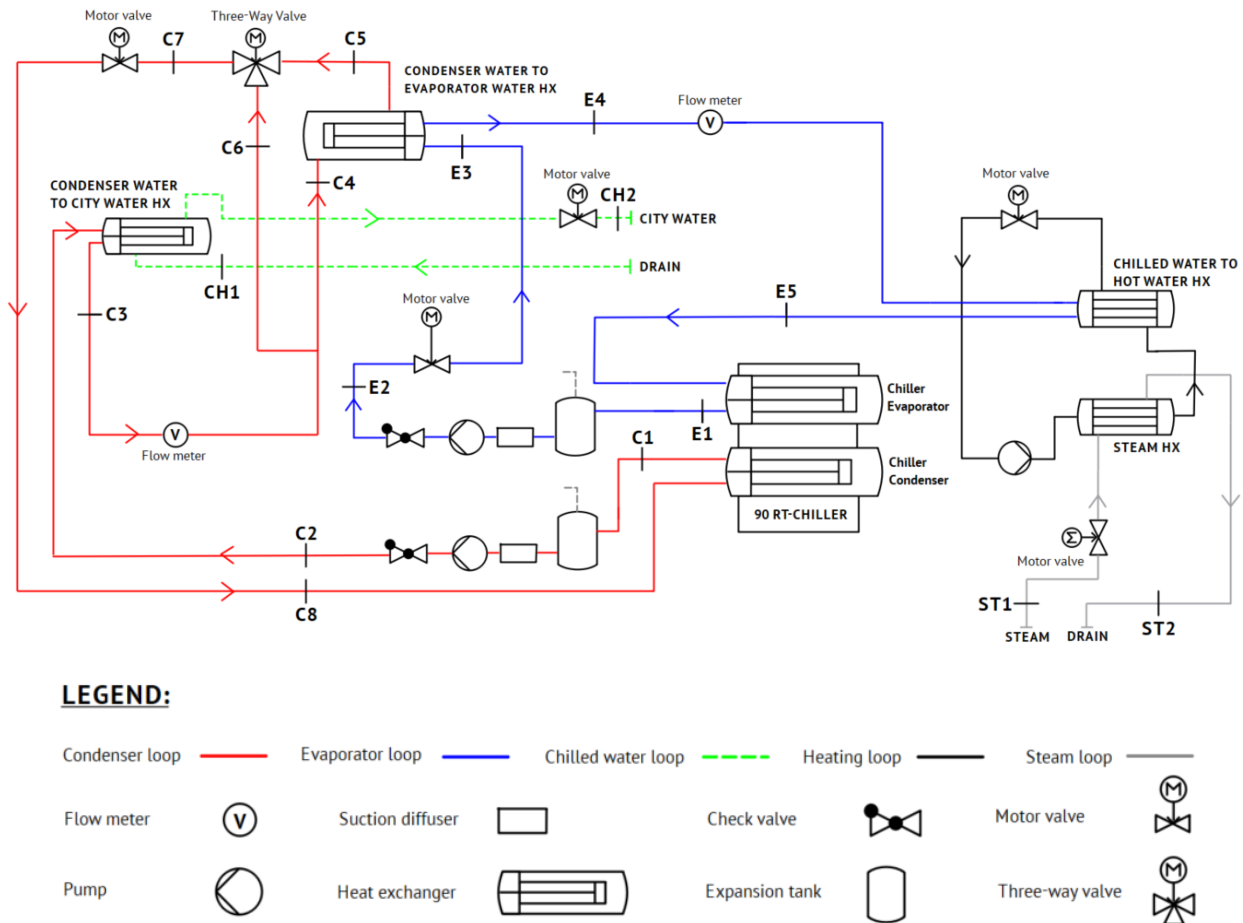


Figure 8: Schematic of the original experimental system (based on [14]; [46])

### 2.2.2 Standard requirements and design targets

The new experimental setup needed to be designed to meet the testing requirements according to AHRI Standard 550/590 [38] which describes the performance rating of water-chilling vapor compression systems and the calculations of the Integrated Part Load Value (IPLV). To this end the following requirements have been identified:

- provide adequate water flow rates for both the condenser and evaporator loops.
- Simulate loading conditions from 25% to 100% of the nominal load.
- Maintain the required entering and leaving temperatures of the evaporator and condenser water loops at each loading condition. IPLV is the AHRI and industry standard method which defines the average chiller efficiency.

The standard defines a reference flow rate for water chilling mode of  $2.4 \text{ GPM/RT}$  ( $0.043 \text{ kg/s}\cdot\text{kW}$ ) at the nominal rating condition. However, this is a reference value and priority during testing is given to maintaining the adequate entering and leaving water temperatures. A reference flow rate is not provided for the condenser loop as the condenser heat rejection required for a given evaporator capacity will vary depending on the design of the chiller refrigeration circuit. However, during testing priority should be given to maintaining the proper entering and leaving water temperatures. The flow rates and water temperatures defined in Standard 550/590 [38] are listed in Table 3. Considering the reference flow rate provided in the standard and the flow rates provided in the chiller data sheet from York, the test stand should be able to provide a water flow rate of  $356 \text{ GPM}$  ( $22.46 \text{ kg/s}$ ) for the evaporator loop and  $475 \text{ GPM}$  ( $29.97 \text{ kg/s}$ ) for the condenser loop.

Table 3: AHRI 550/590 standard rating conditions [38]

Evaporator			Condenser		
Entering Temperature $^{\circ}\text{F}$ ( $^{\circ}\text{C}$ )	Leaving Temperature $^{\circ}\text{F}$ ( $^{\circ}\text{C}$ )	Flow Rate $\text{GPM/RT}$	Entering Temperature $^{\circ}\text{F}$ ( $^{\circ}\text{C}$ )	Leaving Temperature $^{\circ}\text{F}$ ( $^{\circ}\text{C}$ )	Flow Rate $\text{GPM/RT}$
54.00 (12.22)	44.00 (6.67)	2.4	85.00 (29.44)	94.30 (34.61)	-

The standard rating for part-load conditions includes four tests at 25%, 50%, 75%, and 100% load, respectively. The required entering and leaving water temperatures of the evaporator and condenser are defined for each of these conditions in the standard. If the chiller due to its capacity control logic is unable to achieve any of these specific test conditions, then the chiller efficiency at the specific rating condition can be determined by interpolation using two closest neighboring points. A test run must have a length of at least 15 minutes of steady state operation and the temperatures are allowed to deviate maximum  $\pm 0.5$  °F ( $\pm 0.28$  K) from the target temperature within this time.

### 2.2.3 First generation test system

After the old system setup and components was reviewed and the standard requirements have been clarified, it was determined that a similar approach would be suitable for the new experimental system. A schematic of the new experimental system for testing the screw chiller is shown in Figure 9.

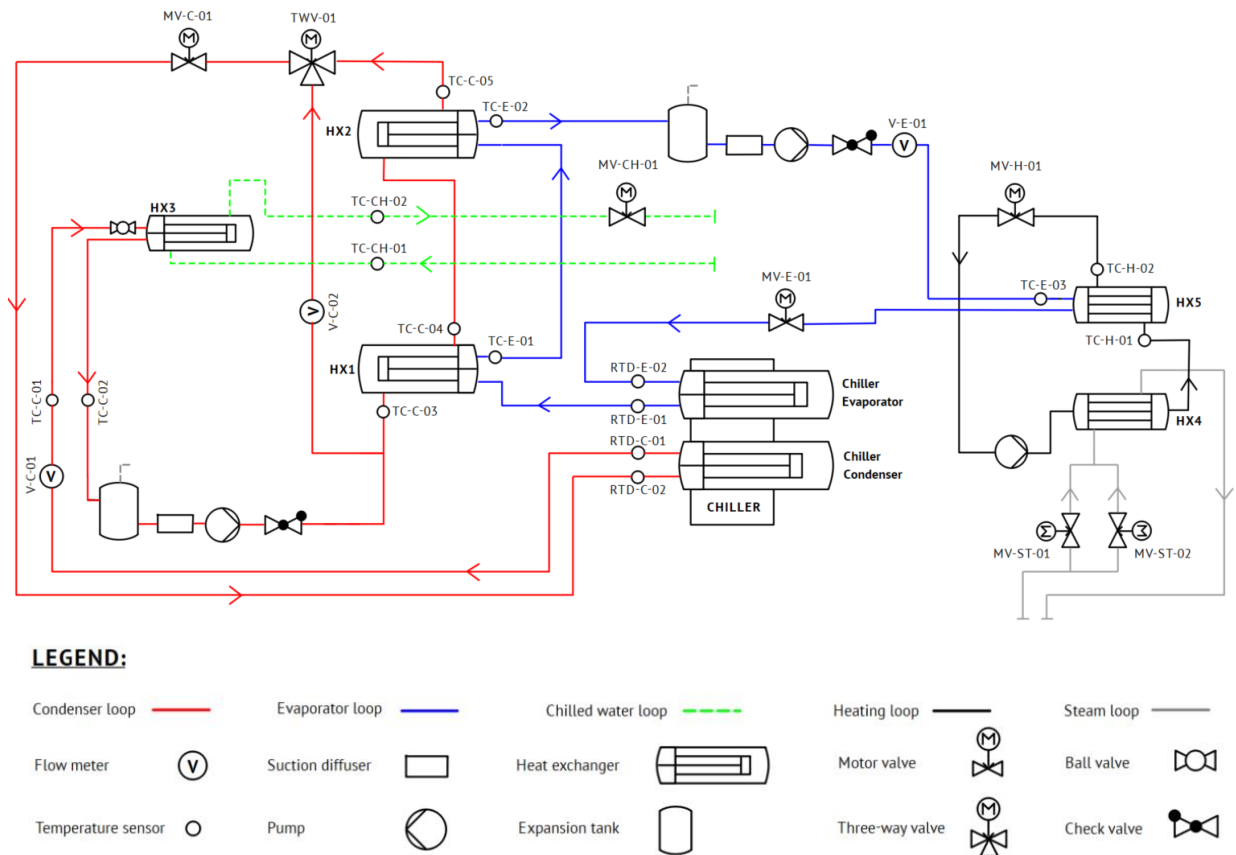


Figure 9: PI-Diagram of the first-generation system setup [46]

The condenser loop is shown in red; the evaporator loop is shown in blue; a chilled water supply and return are shown in green; and the steam and hot water loops are shown in grey and black, respectively. Two regenerative shell and tube heat exchangers, labeled HX1 and HX2, are used in series to transfer heat between the closed condenser and evaporator water loops. Two heat exchangers were used in series to increase total heat exchanger capacity while taking advantage of existing shell and tube heat exchangers which were already on hand. The condenser water is cooled by a separate chilled water heat exchanger, labeled HX3, as in the 90 *RT*-system design, however chilled water provided by the campus utilities is used instead of city water. The campus chilled water provides water at a lower temperature than the city utility and does not require water to be dumped down the drain. Finally, the entire steam and hot water heat exchanger loop assembly, labeled HX4 and HX5, will be repurposed in this design to provide precise control over the evaporator inlet temperature while also providing the ability to rapidly increase the loading condition. Most of the components have been repurposed for the new system design except for the condenser and evaporator pumps which needed to be sourced new to support the higher flow rates required by the higher capacity chiller. To enable the series regenerative heat exchanger setup, two Bell & Gossett WU104-2 heat exchangers are used in series. An available Bell & Gossett WU105-2 heat exchanger is used for the campus chilled water/condenser loop heat exchanger.

New instrumentation and data acquisition equipment were acquired for the new test stand. All the sensors for temperature and flow rate measurements are indicated in Figure 9. Table 14 lists the properties of all measuring devices including band range and uncertainties. A National Instruments cRIO-9057 is used to acquire data and to enable remote control of the experimental system using a LabVIEW VI [47]. Control over the system is accomplished by using the flow control valves that were in use in the previous test stand. By changing the position of the condenser three-way valve and the two-way flow control valves on the steam and campus chilled water lines, one can control the simulated loading condition on the chiller.

A first law energy balance model was developed using the Engineering Equation Solver (EES) software [48] to verify that the selected heat exchanger configuration could support full load testing of the chiller. The heat exchangers used in the system are U-Tube type shell and tube heat exchangers similar to that shown in Figure 10 with water as working medium in the shell and the tube side.

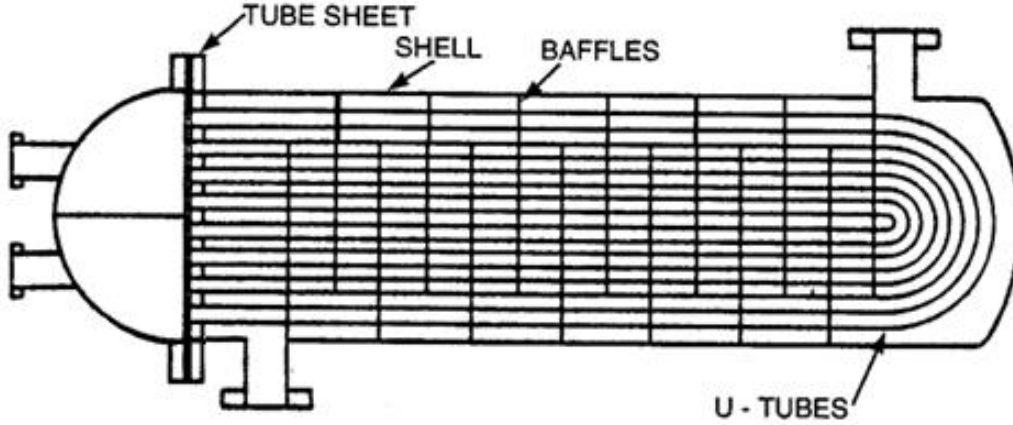


Figure 10: U-tube heat exchanger geometry (adapted from [39])

The effectiveness-NTU approach was used to model the shell and tube heat exchangers, and the heat exchanger models were validated against manufacturer specifications. The three generic governing equations for the NTU method are given by Equations 2.1, 2.2, and 2.3. Equation 2.4 is used to determine the overall heat transfer coefficient for a shell and tube heat exchanger, which is a function of the shell and tube side heat transfer coefficients. Experimental correlations from Kern [40] were used to solve for the heat transfer coefficients.

$$NTU = \frac{U \cdot A}{C_{\min}} \quad (2.1)$$

$$\varepsilon = f(NTU, C_r) \quad (2.2)$$

$$\dot{Q} = \varepsilon \cdot C_{\min} \cdot (T_{h,i} - T_{c,i}) \quad (2.3)$$

$$\frac{1}{U} = \frac{1}{h_s} + \frac{1}{h_t} \quad (2.4)$$

The tube side heat transfer coefficient ( $h_t$ ) requires fluid properties, inlet temperature, flow rate, and inner pipe diameter ( $d_i$ ). The thermodynamic library in EES is used to compute the necessary properties such as density ( $\rho$ ), tube and wall dynamic viscosities ( $\mu_t, \mu_{t_w}$ ), mass flow rate ( $\dot{m}$ ), thermal conductivity ( $k_t$ ), specific heat ( $c_t$ ), and Prandtl number ( $Pr_t$ ). A 20 psi (137.9 kPa) pressure is assumed to retrieve the properties since this was the operating pressure in the former

system setup [14] and therefore the closest value to what can be achieved. The Nusselt number is computed using Equation 2.5 by considering turbulent and fully developed flow conditions.

$$\text{Nu}_t = 0.023 \cdot \text{Re}_t^{\frac{4}{5}} \text{Pr}_t^{0.4} \quad (2.5)$$

A correction factor,  $j_h$ , is calculated as suggested by Kern [40] in Equation 2.6, and the convective heat transfer coefficient is computed in Equation 2.7.

$$j_h = \text{Nu}_t \left( \frac{c_t \mu_t}{k_t} \right)^{-\frac{1}{3}} \left( \frac{\mu_t}{\mu_{t_w}} \right)^{-0.14} \quad (2.6)$$

$$h_t = j_h \frac{k_t}{d_t} \left( \frac{c_t \mu_t}{k_t} \right)^{\frac{1}{3}} \left( \frac{\mu_t}{\mu_{t_w}} \right) \quad (2.7)$$

The shell side computation is more complex due to the shell's geometry (Table 4). In addition to requiring the same fluid information as the tube side, the correlation from Kern [40] requires geometry details of the heat exchanger such as baffle distance ( $B$ ), pitch ( $P_r$ ), tube spacing ( $C'$ ), shell diameter ( $d_s$ ), and tube arrangement. The baffle dimensions were measured when the heat exchangers were disassembled for cleaning. All other measurements were provided in the manufacturer spec sheet. Equations 2.8 to 2.11 are used to solve for the shell side Reynolds number ( $\text{Re}$ ) where ( $\alpha_s$ ) is the effective cross-sectional area, ( $G_s$ ) is the effective mass flow rate, and  $d_e$  is the effective shell diameter.

$$\alpha_s = \frac{d_s \cdot C' \cdot B}{P_r} \quad (2.8)$$

$$G_s = \frac{\dot{V}_s \cdot \rho_s}{\alpha_s} \quad (2.9)$$

$$d_e = \frac{4 \left( 0.86 \frac{P_r^2}{2} - \frac{1}{8} \pi d_s^2 \right)}{\frac{1}{2} \pi d_s} \quad (2.10)$$

$$\text{Re}_s = \frac{d_e \cdot G_s}{\mu_s} \quad (2.11)$$

Table 4: Geometric information of the heat exchangers

		<b>WU104</b>	<b>WU105</b>
Length of tube	<i>in (cm)</i>	48 (121.92)	60 (152.4)
Number of tubes		76	76
Area	<i>ft<sup>2</sup> (m<sup>2</sup>)</i>	58.4 (5.43)	73.3 (6.81)
Baffle distance	<i>in (cm)</i>	16 (40.64)	20 (50.8)
Pitch	<i>in (cm)</i>	0.9374 (2.38)	0.9374 (2.38)
Tube diameter	<i>in (cm)</i>	0.680 (1.73)	0.680 (1.73)
Tube wall thickness	<i>in (cm)</i>	0.035 (0.89)	0.035 (0.89)

The correlation provided by Kern [40] for determining the shell side Nusselt number (Nu) is given in Equation 2.12. Finally, the shell side heat transfer coefficient is solved using Equation 2.13.

$$\text{Nu}_s = 0.36 \cdot \text{Re}_s^{0.55} \cdot \left( \frac{C_s \cdot \mu_s}{K_s} \right)^{\frac{1}{3}} \cdot \left( \frac{\mu_s}{\mu_{sw}} \right) \quad (2.12)$$

$$h_s = \frac{\text{Nu}_s k_s}{d_e} \quad (2.13)$$

Table 5: Comparison with specified heat exchanger data and model predictions

		<b>Results</b>				
<b>Fluid Combination</b>	<b>U Specs</b>	<b>U Model</b>	<b>U-Error</b>	<b>Capacity Specs</b>	<b>Capacity Model</b>	<b>Capacity Error</b>
	<b>Btu/(hr ft<sup>2</sup> °F)</b>	<b>Btu/(hr ft<sup>2</sup> °F)</b>	<b>%</b>	<b>Btu/hr</b>	<b>Btu/hr</b>	<b>%</b>
<b>WU-104</b> Water/Water	315.9	313.6	<b>1%</b>	1.09E+09	1.08E+06	<b>1%</b>
<b>WU-105</b> Water/Water	377.4	384.8	<b>2%</b>	1.63E+09	1.65E+06	<b>1%</b>

By knowing the heat transfer coefficients,  $U$  is computed as outlined in Equation 2.4, and the NTU-method is employed to solve for the capacity of the heat exchanger. This model was validated using the Bell and Gossett (B&G) specifications for both internal heat exchangers in the system. Both, the overall heat transfer coefficient, and capacity were below a 2% error with respect to the rating conditions. Table 5 shows the comparison between the heat exchanger specifications and the model predictions.

After completing the numerical verifications on the heat transfer rate capabilities of the system and the system assembly, the new experimental setup was ready for commissioning.

## 2.2.4 Commissioning and performance limits

The commissioning of the new chiller test setup had two main purposes: ensuring a leak-free system and assess the operations of the components including actuated valves. The shake-down testing phase was particularly important to verify the correct operation of the components. Heat exchangers were of particular concern due to possible fouling from previous testing. During the startup phase, the major components performed as expected. However, after analyzing the data, it was clear that three components (i.e., a heat exchanger and two pumps) were undersized for the current test setup. One was the shell and tube heat exchanger that is used to dissipate heat via the campus chilled water cycle. The first test runs showed that the heat exchanger could not dissipate as much heat as needed. This led to the problem that especially in higher operations, the working fluid temperatures raised slightly during the test runs and a steady state could not be achieved as Figure 6 shows. In the diagram, the condenser inlet temperature, shown in green, consistently diverges from the constant temperature level shown with a dashed black line. Since the maximum allowed temperature deviation in a 15-minute steady state is just  $\pm 0.5$  °F ( $\pm 0.28$  K), the heat rejection capacity needed to be investigated closer.

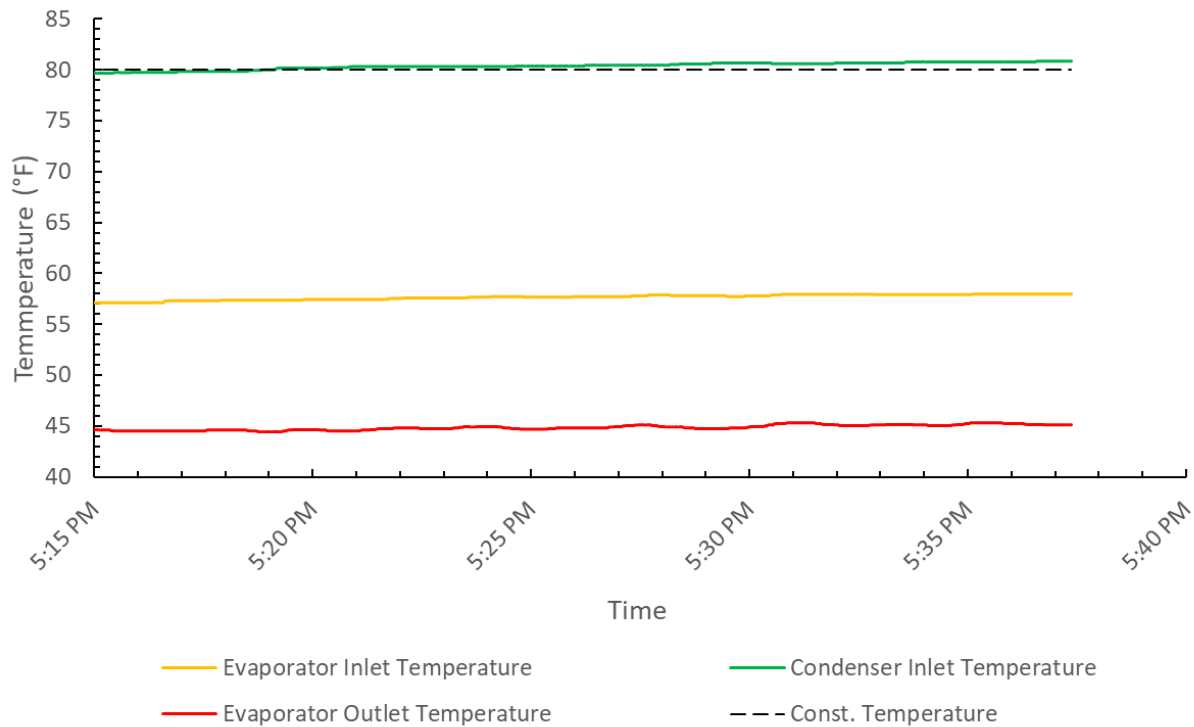


Figure 11: 90% Load test run with first-generation test stand

The other two components that did not perform as calculated were the pump of the condenser water loop and the pump of the evaporator water loop. The condenser water loop pump just provided a flow rate of about 290 *GPM* (18.27 *kg/s*) while the evaporator loop pump just provides a flow of about 245 *GPM* (15.46 *kg/s*). These values are far of the targets described in Section 2.2.2. The explanation for this is, that the pressure drops within both loops of the system changed more than initially calculated. The AHRI 550/590 standard [38] allows a certain deviation of the target flow rates depending on the system, but to ensure comparable performance data to the manufacturer specification, the pump needed to be upgraded.

For a proper operation of the test stand, the heat rejection via the campus chilled water cycle must cover at least the electrical power input of the compressor to avoid an uncontrolled raise of the working fluid temperatures. At maximum capacity with a cooling load of 145.9 *RT* (513.1 *kW*) the electrical energy consumption of the chiller is 79.53 *kW* according to the specification [36]. Due to the constant temperature increase at higher load operations (Figure 11), the effectiveness of the Bell & Gossett WU-105 heat exchanger was calculated to get a better understanding of the operation of the heat exchanger. The heat exchanger is installed in the condenser water cycle of the test stand (HX3 in Figure 9).

The effectiveness of a heat exchanger is defined as [40]:

$$\varepsilon = \frac{\dot{Q}}{\dot{Q}_{\max}} \cdot 100\% \quad (2.14)$$

Where  $\dot{Q}_{\max}$  is the theoretically maximum heat transfer rate in *kW* and the actual heat transfer rate  $\dot{Q}$  is the heat capacity that the heat exchanger dissipates via the chilled water cycle in *kW*. It is calculated as the product of mass flow  $\dot{m}_{V-C-01}$  on the condenser water cycle side of the heat exchanger, the specific heat  $c_p$  and the temperature gradient between the inlet temperature  $T_{TC-C-01}$  and the outlet temperature  $T_{TC-C-02}$  using the equation

$$\dot{Q} = \dot{m}_{V-C-01} \cdot c_p \cdot (T_{TC-C-01} - T_{TC-C-02}) \quad (2.15)$$

Table 6 indicates the calculated values for the loads during the commissioning test runs. The second column shows the actual heat transfer rate that is used for the effectiveness calculation. The other columns show the load levels that were achieved in the tests, the mass flow (V-C-01) and the measured temperatures TC-C-01 (inlet) and TC-C-02 (outlet).

Table 6: Actual heat transfer rate for different load levels during the commissioning

<b>Load</b>	<b><math>\dot{Q}</math></b>	<b>V-C-01</b>	<b><math>c_p</math></b>	<b>TC-C-01</b>	<b>TC-C-02</b>
<i>%</i>	<i>kW</i>	<i>kg/s</i>	<i>kJ/kg</i>	<i>°C</i>	<i>°C</i>
34	22.407	18.73	4.19	18.76	18.47
42	25.943	18.19	4.19	21.41	21.07
48	32.311	17.70	4.19	21.84	21.40
56	36.456	17.27	4.19	22.92	22.41
74	65.521	17.33	4.19	29.69	28.78
79	70.520	17.01	4.19	30.02	29.03
90	85.495	18.43	4.19	34.12	33.02

Then, the maximum possible heat transfer rate must be calculated. It is a theoretical value that describes the heat exchanger capacity that could be achieved, in a heat exchanger of infinite length. If such a heat exchanger would be installed in the test stand set up, the maximum possible temperature difference could be achieved. The maximum possible temperature gradient in this case is the difference of the temperature of the water at the inlet of the heat exchanger on the condenser water cycle and the temperature at the inlet of the heat exchanger on the chilled water cycle. This maximum possible temperature difference is valid for both sides of the heat exchanger. Since the temperature difference and the specific heat ( $4.19 \text{ kJ}/(\text{kg}\cdot\text{K})$ ) is the same on both fluid sides of the heat exchanger, the different mass flows are the significant dimensions for the maximum possible heat transfer rate.

Due to varying mass flows in both cycles (condenser water cycle and chilled water cycle), the maximum possible heat transfer rate is different for every cycle. For the effectiveness-NTU method, the smaller heat transfer rate value should be used as indicated by Equations 2.16 and 2.17.

$$\dot{Q}_{\max-C-\text{Cycle}} < \dot{Q}_{\max-CH-\text{Cycle}} \rightarrow \dot{Q}_{\max-C-\text{Cycle}} = \dot{Q}_{\max} \quad (2.16)$$

$$\dot{Q}_{\max-CH-\text{Cycle}} < \dot{Q}_{\max-C-\text{Cycle}} \rightarrow \dot{Q}_{\max-CH-\text{Cycle}} = \dot{Q}_{\max} \quad (2.17)$$

As the first one of this two possible maximum capacities, the maximum transfer rate for the chilled water mass flow  $\dot{Q}_{\max-CH-\text{Cycle}}$  gets calculated. Since there is now mass flow meter to acquire the mass flow of the chilled water from the campus supply, the value must be computed initially. To get the mass flow for the different load levels, the actual heat transfer rate of the conducted test runs as calculated previously in this chapter. The actual heat transfer rate is then

divided by the product of the specific heat of the chilled water  $c_p$  and the temperature difference between the inlet and the outlet of the campus chilled water at the heat exchanger.

$$\dot{m}_{CH} = \frac{\dot{Q}}{c_p \cdot (t_{TC-CH-02} - t_{TC-CH-01})} \quad (2.18)$$

Based on equation 2.18 and the measured values, the mass flow can be calculated as shown in Table 7. The results are the base for the heat transfer calculation of the chilled water side of the heat exchanger.

Table 7: Mass flow in the chilled water cycle

<b>Load</b>	<b><math>\dot{m}_{CH}</math></b>	<b><math>\dot{Q}</math></b>	<b><math>\Delta T_{ch}</math></b>
<i>%</i>	<i>kg/s</i>	<i>kW</i>	<i>K</i>
34	1.320	22.41	4.04
42	1.183	25.94	5.22
48	1.684	32.31	4.57
56	2.385	36.45	3.64
74	3.310	65.52	4.71
79	3.960	70.52	4.24
90	6.474	85.49	3.14

By using the computed mass flow for the campus chilled water supply the maximum heat transfer rate  $\dot{Q}_{max-CH}$  of the chilled water cycle can be calculated. Besides the computed mass flow, the maximum possible temperature gradient is used. The maximum capacity of the chilled water cycle is calculated as

$$\dot{Q}_{max-CH} = \dot{m}_{CH} \cdot c_p \cdot (T_{TC-C-01} - T_{TC-CH-01}) \quad (2.19)$$

Table 3 displays the results for the maximum possible heat transfer of the chilled water site of the heat exchanger. The  $\dot{Q}_{max-CH}$  increases strongly with the load levels. The reason for that is the sharp increase of the temperature difference and the increasing mass flow.

Table 8: Maximum heat transfer rate on the chilled water side

<b>Load</b> %	$\dot{Q}_{\max\text{-CH}}$ <i>kW</i>	$\dot{m}_{\text{CH}}$ <i>kg/s</i>	<b>TC-C-01</b> °C	<b>TC-CH-01</b> °C
34	60.74	1.32	18.76	7.80
42	69.11	1.183	21.41	7.50
48	105.50	1.684	21.84	6.92
56	149.50	2.385	22.92	7.99
74	335.32	3.31	29.69	5.56
79	414.02	3.96	30.02	5.12
90	724.45	6.474	34.12	7.48

The following step demonstrates the calculation of the maximum heat transfer rate of the condenser cycle  $\dot{Q}_{\max\text{-C}}$ . The maximum possible temperature gradient and the specific heat remains the same as in the previous step. A measured value is provided for the mass flow on the condenser cycle side. Based on this, the equation

$$\dot{Q}_{\max\text{-C}} = \dot{m}_{\text{V-C-01}} \cdot c_p \cdot (T_{\text{TC-C-01}} - T_{\text{TC-CH-01}}) \quad (2.20)$$

allows a calculation of the  $\dot{Q}_{\max\text{-C}}$ .

The maximum capacity for the condenser water cycle  $\dot{Q}_{\max\text{-C}}$  calculated, using the formula above is listed in Table 9. Together with Table 8 it is the basis of the comparison for the  $\dot{Q}_{\max}$  that can be used for the effectiveness calculation.

Table 9: Maximum heat transfer rate on the condenser loop side

<b>Load</b> %	$\dot{Q}_{\max\text{-C}}$ <i>kW</i>	<b>V-C-01</b> <i>kg/s</i>	<b>TC-C-01</b> °C	<b>TC-CH-01</b> °C
34	862.01	18.730	18.76	7.80
42	1062.61	18.190	21.41	7.50
48	1108.43	17.700	21.84	6.92
56	1082.34	17.270	22.92	7.99
74	1755.57	17.330	29.69	5.56
79	1779.06	17.010	30.02	5.12
90	2062.72	18.430	34.12	7.48

Table 10: Load dependent effectiveness of the chilled water heat exchanger

<b>Load</b>	$\epsilon$	$\dot{Q}_{\max-C}$	$\dot{Q}_{\max-CH}$	$\dot{Q}$
%	%	<i>kW</i>	<i>kW</i>	<i>kW</i>
34	36.89	862.01	60.74	22.41
42	37.54	1062.61	69.11	25.94
48	30.62	1108.43	105.50	32.31
56	24.39	1082.34	149.50	36.46
74	19.54	1755.57	335.32	65.52
79	17.03	1779.06	414.02	70.52
90	11.80	2062.72	724.45	85.50

In the final step, the effectiveness is evaluated load dependent according to equation 2.14 as shown in Table 10. The results support the initial suggestion that the effectiveness of the heat exchanger is generally too low and is further decreasing with higher load operation. A possible reason for this might be corrosion. That leads to the problem, that not enough heat can be dissipated from the system in higher load conditions. As a result of that the temperatures in the whole test system start raising with higher load and the chilled water heat exchanger cannot compensate this trend. This makes it impossible for the user to hold the values and temperatures mentioned in the test plan in an appropriate and suitable precision.

To solve this problem, an additional heat exchanger was designed to supplement the heat dissipation. Since the effectiveness is reduced to 11.8% in high-capacity levels, the new heat exchanger is selected with a nominal capacity that equals the heat input by the compressor. The temperatures on the chilled water side are assumed to be 44 °F (6.67 °C) on the inlet side and maximum 54 °F (12.22 °C) on the outlet side. The mass flow on the condenser loop side was taken from the measurements of the commissioning test runs and, on the campus chilled water side, from the effectiveness calculation (Table 7). A shell and tube type heat exchanger was preferred to maintain the pressure drop in the system relatively low. Given the design data, the manufacturer recommended the heat exchanger Bell & Gossett WU84-24 with steel shell and copper tube. This heat exchanger was installed in parallel to the existing heat exchanger on the condenser loop side to keep the pressure drop low and in series on the chilled water cycle due to the simpler installation.

The flow rates turned out to be too low in both water loops during the commissioning of the first-generation setup. To select a bigger pump size in both cycles, the actual pressure drops the actual pressure drop ( $\Delta p_1$ ) of the system needs to be calculated first with the help of Equation 2.21 by using the design pressure drop ( $\Delta p_2$ ) and the design flow rate ( $\dot{m}_2$ ) of the pumps and the flow rates that were achieved in the commissioning test runs ( $\dot{m}_1$ ).

$$\frac{\Delta p_2}{\Delta p_1} = \left(\frac{\dot{m}_2}{\dot{m}_1}\right)^2 \quad (2.21)$$

By using the actual pressure drops of the two water loops, new pumps could be selected that are capable of providing higher flow rates with the given pressure drop. The pressure drop for the condenser water loop was calculated as 46 *psi* (317 *kPa*). The pressure drop for the evaporator water loop was calculated as 25 *psi* (172.4 *kPa*).

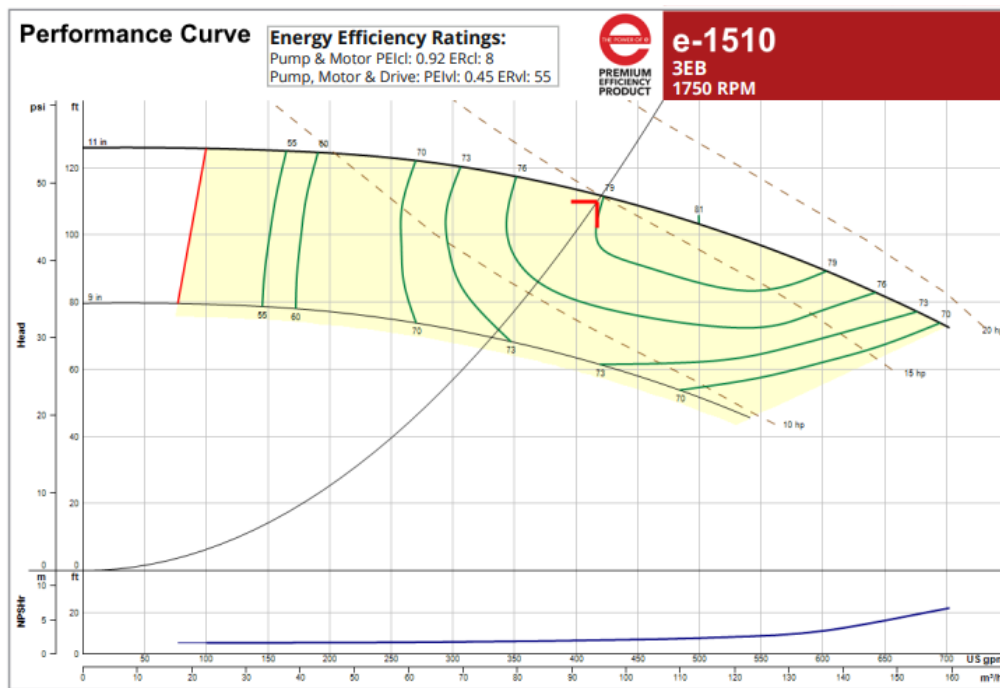


Figure 12: Performance curve of the condenser water pump [41]

For the condenser water loop, the pump Bell & Gossett e-1510 3EB was selected. This pump can provide a flow of 420 *GPM* (26.50 *kg/s*) in the condenser loop according to the performance curve (see Figure 12). This flow rate could also be achieved in later test runs. The limiting factors that led to the selection of this pump are the maximum current draw given by the

research facility and the pipe diameter which is given with 4 inches (10.16 cm) by the system that made it not possible to fit a bigger pump into the system.

The Bell & Gossett E-1531 3BD pump, that was in the condenser water loop in the first-generation setup and that has been replaced was installed as replacement for the evaporator water loop for the second-generation setup. According to the performance curve in Figure 13 a flow of about 435 GPM (27.44 kg/s) at a head pressure of 25 psi or 58 ft (172.4 kPa).

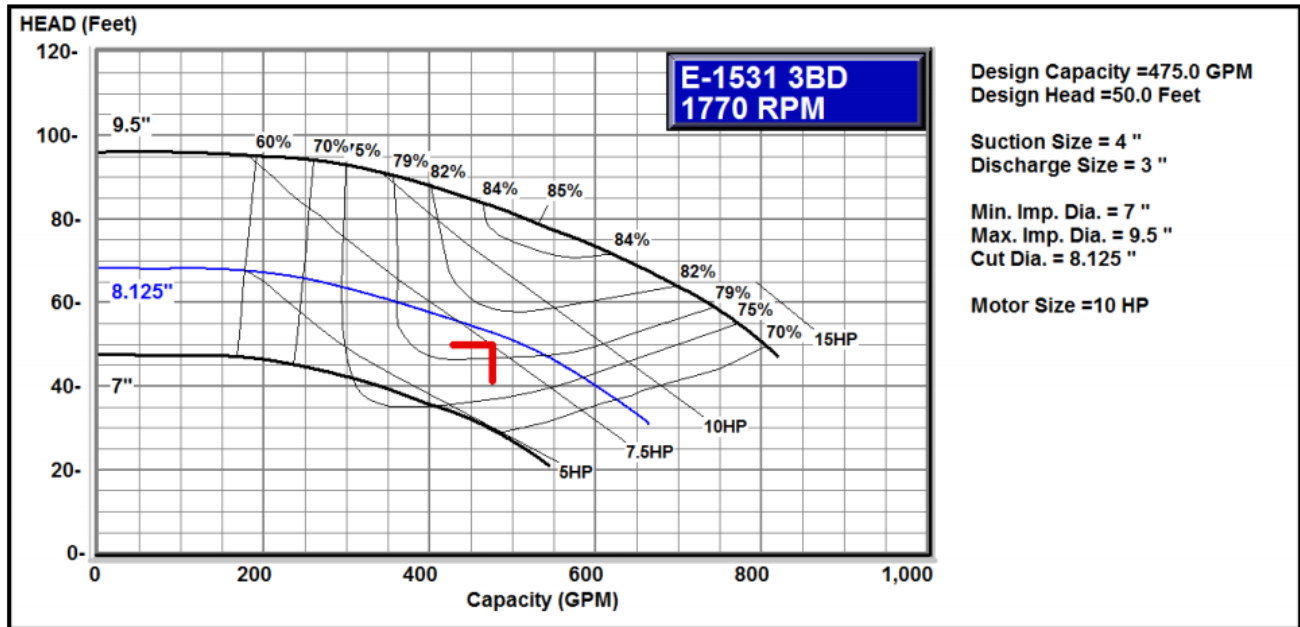


Figure 13: Performance curve of the evaporator loop water pump [42]

Later test runs showed that just a flow of not higher than 310 GPM (19.56 kg/s) is possible to achieve in the evaporator water loop. This is far of the flow rate that results from the performance curve of the pump (see Figure 13). That flow is not high enough to perform suitable baseline tests since a flow of 300 GPM (18.93 kg/s) is needed for that but to exclude serious technical problems that may cause a later break down of the system, the deviation between actual flow rate and performance curve flow rate was investigated closer with focus on the factors

- power supply
- motor shaft *RPM*
- pressure losses

All values concerning the electrical power supply like the voltage, current draw, and frequency did not indicate any irregularities when they were professionally checked by a technician. Also,

the check of the number of revolutions per minute of the motor shaft with a strobe light did not identify any malfunction. In operation, a motor speed of 1768 *RPM* was measured. Based on the data sheet value of 1770 *RPM* a failure or problem on the electrical side can be excluded.

The third point was to check whether the pressure drop rates are reasonable within the evaporator loop. The pressure difference based on the gauges on the inlet and the outlet of the pump was 25 *psi* or 58 *ft* (172.4 *kPa*) pressure head. In order to check this value for correctness and to determine the pressure losses of the individual components, the operating pressure within the system (Figure 14) was mapped at a flow of 310 *GPM* (19.56 *kg/s*).

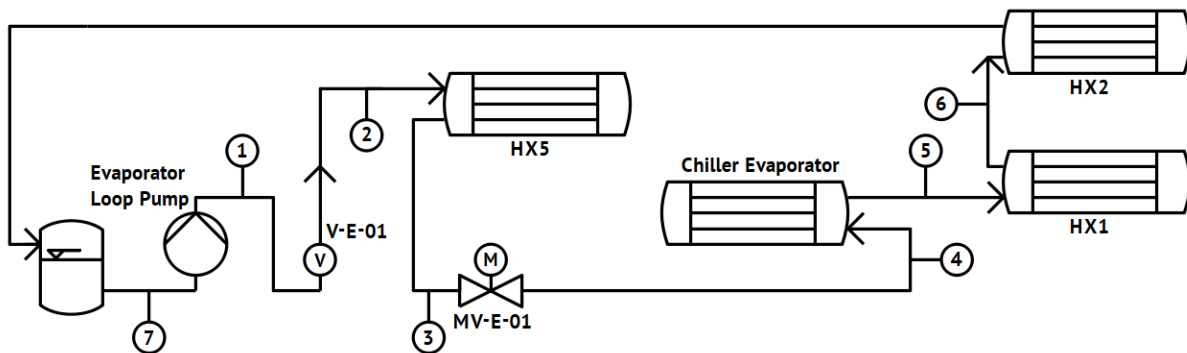


Figure 14: Simplified flow diagram of the evaporator loop with probe positions [46]

Table 11: Pressure drops of the single components within the evaporator loop

Component	Pressure drops in <i>ft</i> ( <i>kPa</i> )
Piping	9 (26.75)
Heat exchanger HX 5	3 (8.82)
Motor valve and piping	13 (38.68)
Chiller evaporator	12 (35.71)
Heat exchanger HX1	9 (26.75)
Heat exchanger HX2	12 (35.71)

Table 11 summarizes the pressure drop caused by every individual component within the evaporator water loop. The investigation does not show any excessively high pressure drop or indicate a failure of the permanently installed pressure gauges in the system.

Finally, a reason for the reduced flow could not be specified in the investigation. Since a selection of bigger pumps was not possible for the mentioned reasons a solution was requested to enable the chiller testing. One option was, to test the chiller at a lower maximum capacity. This is

possible because the same chiller is also sold as 125-RT chiller just with lower flow rates. The components and technical setup are all the same. A review the operating conditions and nominal performance (Table 12) as well as the AHRI test conditions (Table 13) came to the conclusion that the requirements for this test with a flow of 300 *GPM* (18.93 *kg/s*) in the evaporator loop and a flow of 382.7 *GPM* (24.14 *kg/s*) in the condenser loop could be met and therefor a standard conform performance rating was possible.

Table 12: Operating conditions and nominal performance [36]

Evaporator Data		Condenser Data		Performance Data	
EWT (°F)	54.00	EWT (°F)	85.00	Full Load Efficiency (kW/ton.R)	0.6363
LWT (°F)	44.00	LWT (°F)	94.30	IPLV.IP (kW/ton.R)	0.4063
Flow (USGPM)	299.2	Flow (USGPM)	382.7	Heat Rejection (MBH)	1771
Pressure Drop (ft H2O)	6.31	Pressure Drop (ft H2O)	6.33	Physical Data	
Fluid	Water	Fluid	Water	Rigging Wt. (lb)	7727
Fouling Factor (h.ft².F/Btu)	0.000100	Fouling Factor (h.ft².F/Btu)	0.000100	Operating Wt. (lb)	8367
Fluid Volume (USGAL)	46.00	Fluid Volume (USGAL)	44.00	Refrigerant Charge (lb)	280
Min Fluid Flow Rate (USGPM)	280.0	Min Fluid Flow Rate (USGPM)	240.0	Length (in)	116.6
Max Fluid Flow Rate (USGPM)	870.0	Max Fluid Flow Rate (USGPM)	910.0	Width (in)	55.6
Evap Type	Hybrid Falling Film	Cond Type	Water Cooled Condenser	Height (in)	72.7
Chiller Type	Water Cooled VSD Screw	Compressor Type	VSD Screw - Semi Hermetic		
Number Passes	2	Number Passes	2		

Table 13: Nominal performance under AHRI 550/590 test conditions [43]

Performance at AHRI Conditions					
Evaporator Data		Condenser Data		Performance Data	
EWT (°F)	54.00	EWT (°F)	85.00	Full Load Efficiency (kW/ton.R)	0.6363
LWT (°F)	44.00	LWT (°F)	94.30	IPLV.IP (kW/ton.R)	0.4064
Flow Rate (USGPM)	299.2	Flow Rate (USGPM)	382.7	Heat Rejection (MBH)	1771
Pressure Drop (ft H2O)	6.31	Pressure Drop (ft H2O)	6.33	Cooling Capacity (ton.R)	125.0
Fluid	Water	Fluid	Water		
Fouling Factor (h.ft².F/Btu)	0.000100	Fouling Factor (h.ft².F/Btu)	0.000250		
Fluid Volume (USGAL)	46.00	Fluid Volume (USGAL)	44.00		

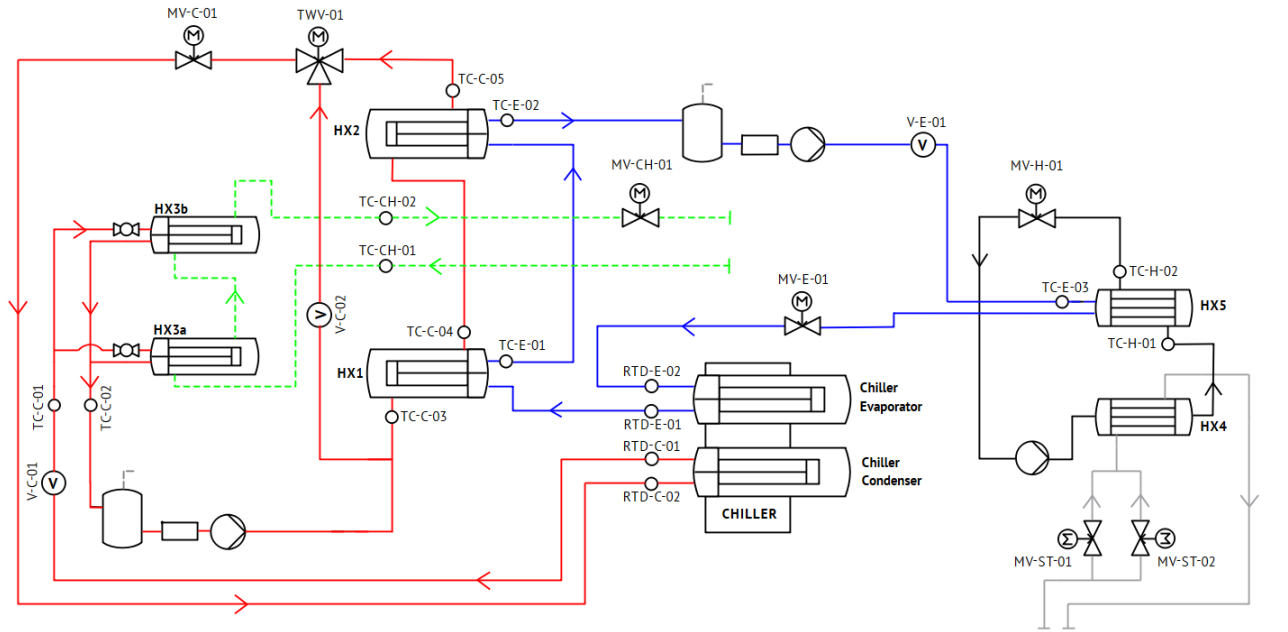
### 2.2.5 Second generation test system

The upgrade of to a standard conform test system required some component and setup changes. Figure 15 shows the PI-diagram of the test system on the latest status (November 2021). The showed system contains water and not refrigerant. The vapor compression cycle is integrated in the chiller. The test system consists of two main cycles. One is the evaporator water loop that is

marked in blue in the PI-diagram. Beginning from the chiller, the water leaves at setpoint temperature. From there it passes two internal heat exchangers HX1 and HX2 where the temperature is raised as needed for the aimed load condition. The heat that is needed for this step is directly reused from the condenser water loop to keep the input of external energy as low as possible. When the fluid passes the internal heat exchanger, the pressure is raised in the pump that is installed in this loop. After the fluid passes the pump, there is the possibility to additionally add load on the cycle in HX5 by utilizing the auxiliary heating loop marked in black, that is connected to the steam heating system of the lab facility shown in grey in the diagram. The external heating is not used in regular test runs and just helps to allow faster temperature changes. Before the water finally enters the chiller again, a motor valve provides the possibility to control the flow rate in the loop. Usually, full flow is maintained. Then, the working fluid enters the chiller on the correct inlet temperature.

The second main loop is the condenser water loop that is marked in red in the diagram. After the water leaves the chiller in this loop, the fluid first passes the heat exchangers HX3a and HX3b that allow a heat rejection via the campus chilled water cycle marked in green. The capacity of the two heat exchangers can be controlled by a motor valve in the campus chilled water line. This valve is also used to control the condenser inlet temperature during the test operation. The heat exchangers just dissipate the heat load that is added by the compressor since the rest is recharged as load to the evaporator loop in the internal heat exchangers HX1 and HX2. To control the load on the evaporator loop by changing the evaporator inlet temperature, the condenser loop has the option to bypass the internal heat exchangers with a bypass line. The fraction of the flow that is bypassed, is controlled by the three-way valve in the loop. The following motor valve offers the option to reduce the flow in the condenser cycle before the water flows back to the condenser at a specified temperature.

The current setup status (generation two) allows not just tests according to the AHRI 550/590 standard but also baseline tests that allow a comparison with the manufacturer tests. In addition, the installations are able to process in a long term operation such as is an accelerated life test. Figure 16 shows a photograph of the current test set up. On the left side of the picture are the heat exchangers that are used in the condenser cycle. On the center-right is the chiller that is used for the test runs.



**LEGEND:**

Condenser loop		Evaporator loop		Chilled water loop		Heating loop		Steam loop	
Flow meter		Suction diffuser		Heat exchanger		Motor valve		Ball valve	
Temperature sensor		Pump		Expansion tank		Three-way valve		Check valve	

Figure 15: PI-diagram of the second-generation test stand [46]



Figure 16: View on the test stand in the configuration of the second generation

Table 14: List of all sensors used in the second-germination setup

Value	Signal Output Range	Name	Manufacturer	Type	Principle	Measurement Range	Accuracy
	4-20 mA	RTD-C-01	ProSense	RTD1-C06-02	RTD to mA	Pt100 (Class A)	$-58 - 572^{\circ}F$ $\pm (0.15 + 0.002 T)$ $^{\circ}C$
	4-20 mA	RTD-C-02	ProSense	RTD1-C06-02	RTD to mA	Pt100 (Class A)	$-58 - 572^{\circ}F$ $\pm (0.15 + 0.002 T)$ $^{\circ}C$
Temperature	$\Omega$	TC-C-01	ProSense	THMK-C06-02	Thermo Couple	Type K	$32 - 1,700^{\circ}F$ $\pm 2.2^{\circ}C$ or $0.75\%$
	$\Omega$	TC-C-02	ProSense	THMK-C06-02	Thermo Couple	Type K	$32 - 1,700^{\circ}F$ $\pm 2.2^{\circ}C$ or $0.75\%$
	$\Omega$	TC-C-03	ProSense	THMK-C06-02	Thermo Couple	Type K	$32 - 1,700^{\circ}F$ $\pm 2.2^{\circ}C$ or $0.75\%$
	$\Omega$	TC-C-04	ProSense	THMK-C06-02	Thermo Couple	Type K	$32 - 1,700^{\circ}F$ $\pm 2.2^{\circ}C$ or $0.75\%$
	$\Omega$	TC-C-05	ProSense	THMK-C06-02	Thermo Couple	Type K	$32 - 1,700^{\circ}F$ $\pm 2.2^{\circ}C$ or $0.75\%$
Volume flow	4-20 mA	V-C-01	Badger Meter	M2000	Electromagnetic	Pulsed DC	$0.1 - 40$ ft/s $\pm 0.25\%$
	4-20 mA	V-C-02	Badger-Meter	SDIIDIN11-0200	Impeller Sensor	n/A	$3.2 - 20$ ft/s $\pm 1\%$
	4-20 mA	V-E-01	Badger Meter	M2000	Electromagnetic	Pulsed DC	$1 - 40$ ft/s $\pm 0.25\%$
Temperature	4-20 mA	RTD-E-01	ProSense	RTD1-C06-02	RTD to mA	Pt100 (Class A)	$-58 - 572^{\circ}F$ $\pm (0.15 + 0.002 T)$ $^{\circ}C$
	4-20 mA	RTD-E-02	ProSense	RTD1-C06-02	RTD to mA	Pt100 (Class A)	$-58 - 572^{\circ}F$ $\pm (0.15 + 0.002 T)$ $^{\circ}C$
	$\Omega$	TC-E-01	ProSense	THMK-C06-02	Thermo Couple	Type K	$32 - 1,700^{\circ}F$ $\pm 2.2^{\circ}C$ or $0.75\%$
	$\Omega$	TC-E-02	ProSense	THMK-C06-02	Thermo Couple	Type K	$32 - 1,700^{\circ}F$ $\pm 2.2^{\circ}C$ or $0.75\%$
	$\Omega$	TC-E-03	ProSense	THMK-C06-02	Thermo Couple	Type K	$32 - 1,700^{\circ}F$ $\pm 2.2^{\circ}C$ or $0.75\%$
Power Consumption	$\Omega$	TC-CH-01	ProSense	THMK-C06-02	Thermo Couple	Type K	$32 - 1,700^{\circ}F$ $\pm 2.2^{\circ}C$ or $0.75\%$
	$\Omega$	TC-CH-02	ProSense	THMK-C06-02	Thermo Couple	Type K	$32 - 1,700^{\circ}F$ $\pm 2.2^{\circ}C$ or $0.75\%$
	$\Omega$	TC-H-01	ProSense	THMK-C06-02	Thermo Couple	Type K	$32 - 1,700^{\circ}F$ $\pm 2.2^{\circ}C$ or $0.75\%$
	$\Omega$	TC-H-02	ProSense	THMK-C06-02	Thermo Couple	Type K	$32 - 1,700^{\circ}F$ $\pm 2.2^{\circ}C$ or $0.75\%$
	$\Omega$	Chiller-03	Ohio Semitronics	GW5-072EG	Transducer	n/A	$0 - 20 A$ (AC) $\pm 0.2\%$ Rdg./PF, $\pm 0.04\%$ F.S.

Table 14 lists in detail the used sensors in the system. For every sensor, the kind of signal and signal range is described, a detailed manufacturer and type name is provided, and accuracy is displayed to give an exact overview of the components used in the system. The list is supplemented by Table 15 that shows the actuating components like pumps and valves as well as the used heat exchangers.

Table 15: Component list of second-generation test stand

<b>Component</b>	<b>Manufacturer/Model</b>	<b>System Location</b>
Condenser pump	B&G 1510 3EB	Condenser loop
Evaporator pump	B&G 1531 3BD	Evaporator loop
Hot water pump	B&G 1531 2AC	Hot water loop
Regenerative HX	B&G WU104-2	Condenser/evaporator loop
	B&G WU105-2	Condenser/evaporator loop
Chilled water HX	B&G WU104-2	Condenser loop
	B&G WU84-24	Condenser loop
Hot water HX	B&G WU105-2	Hot water loop
Three-way-valve	JCI VB-4322-13	Condenser loop
Two-way control valves	JCI VB-3970-17	All water loops
Two-way steam control valves	JCI VG7241ST	Steam supply
Valve actuators	JCI Y20EBD-3	All valves

## 2.2.6 Water testing

For the first 23 months of the setup, commissioning and use of the test stand, untreated tap water was used in the water loops. Both, the evaporator water loop, and the condenser water loop are closed cycles there was the assumption that fouling is not a big factor in the system. Since the baseline testing (paragraph 3.1) showed performance deviations in comparison with the data specified by the manufacturer, fouling came into discussion even when and that event led to initial water quality deceptions in the beginning of September 2021.

The analysis of the water samples showed no concerning results at the beginning, just some values were slightly out of range. To inhibit further fouling and corrosion in the test system, a chemical treatment was started in the system beginning November 2021. Three different agents are in use to keep improve the water quality and keep it on a continuous level. The first agent is the Suez Depositrol BL6502 which is inserted against the corrosion of steel components. The target

concentration in the system is 12-24 *ppm*. Also in use is the Suez Corrshield BT4301. This is a pH buffer and water stabilizer that is used in a concentration of 100-400 *ppm*. The last chemical is the Suez Inhibitor AZ8101 that is used to avoid corrosion on copper and brass materials. The target concentration is 20-25 *ppm*.

The analysis focuses on the eight parameters. The main parameters are displayed in Figure 17. The values for the evaporator cycle are in blue while the values for the condenser cycle are displayed by the orange dots. One is the conductivity which shows the quantity of particles in the water samples. The desired range for the conductivity value is <750 *ppm*. The conductivity gives general feedback of the fluid quality and the condition of the components in the system. The measured values are high but not concerning. The diagram in Figure 17 shows that the values in both water loops, the conductivity could be slightly reduced by flushing the system at the end of October 2021 and replacing the water with new tap water. Another peak could be measured, after the start of the chemical water treatment which might be refer to chemical reactions in the system such as the solution of dirt and calcium that formatted on surface. The conductivity values stabilized after a month and remained constant.

The second parameter is the pH value with a desired range from 5.5 to 7.5. The results from the water samples appear to be at the higher. Reason for this is the high pH value that the tap water in the facility already has. The Calcium in the tap water causes an alkaline ambient. The pH value did not decrease so far but remains on a stable level. It can be seen that the pH values become more uniform and controlled since the water treatment with chemicals was started.

The third and fourth values under investigation is the total hardness and the Calcium hardness of the water. Those two values are used to calculate a ratio which should be constant. Along with the measured total alkalinity, the Langlier Saturation Index (LSI) is also retrieved. The LSI provides indications on presence of Calcium that can lead to corrosion over time. The normal range for the LSI is between 1.5 and 3.0. The LSI ratio is low but on a consistent level. The low ratio could be a sign that calcium already formatted in the system. This theory would also explain that there were especially low peaks in January 2022. In this time, the low load/high head mode was started on the test stand. The higher operating temperatures support the formation of Calcium additionally and therefore drop the LSI ratio.

As a last value the iron in the water is measured to see the impact of corrosion in the system. This measurement has the most inconsistent outcome, especially in the condenser loop.

The inconsistency is hard to explain, but also when the water samples are taken from the system, the water does not always have the same iron-caused red color. The high peaks followed by a very low measured iron content could be a sign that bigger particles that get loose by corrosion in the system, first solve in the water and then migrate to other surfaces like the heat exchanger. This theory should be considered when the heat exchangers are opened to clean them.

Since a maintenance break with a cleaning of the heat exchangers will be executed shortly, the theories can be controlled during the system check. Also, the amount of all inhibitors that are used can be increased for the next refill of the system. That should lead to a better adjustment of the values in the future.

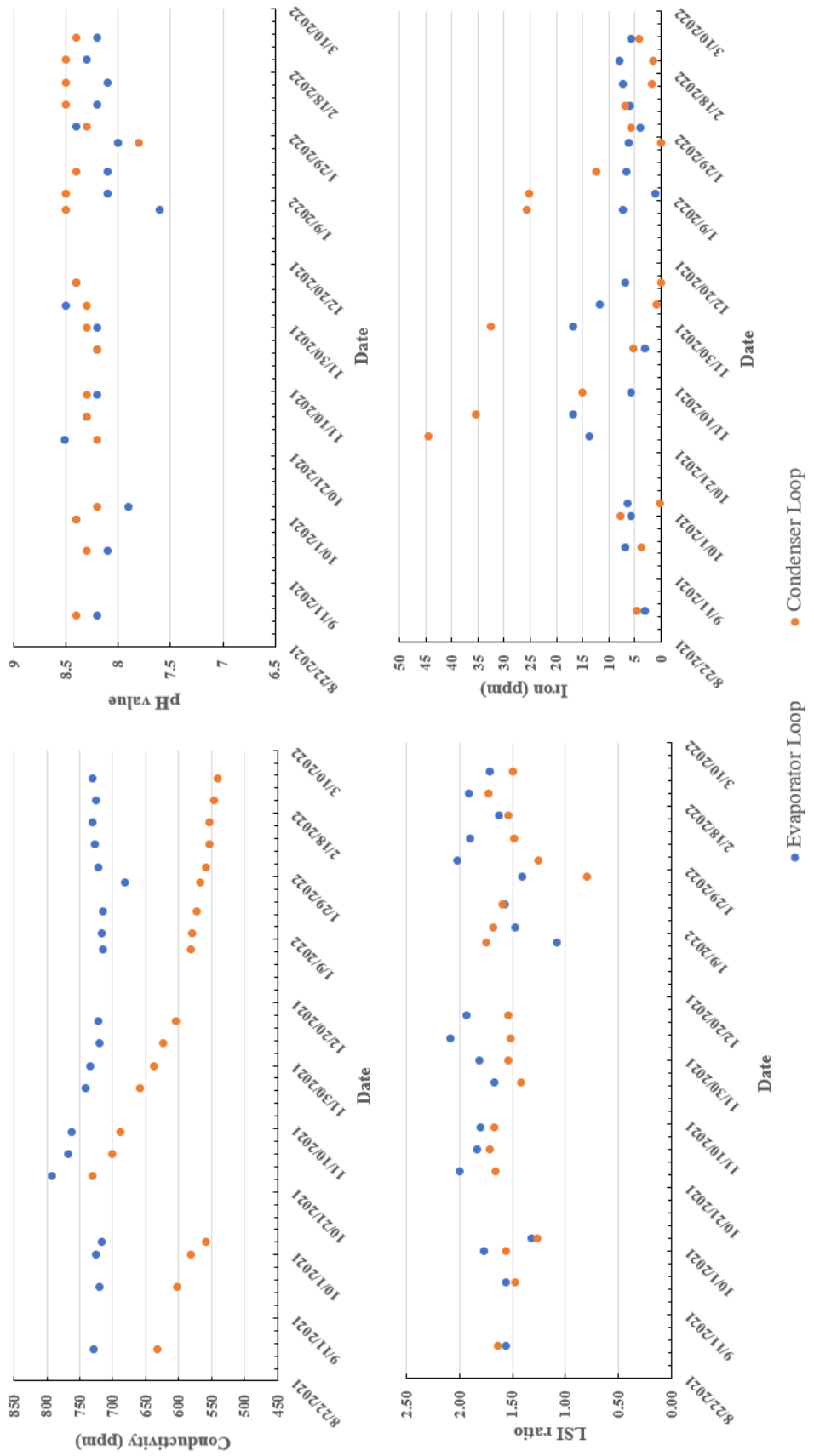


Figure 17: Water test results

### 3. EXPERIMENTAL TESTING

#### 3.1 Baseline testing

##### 3.1.1 Testplan

As previously mentioned, the baseline testing was conducted according to the AHRI 550/590 standard [38]. This standard does not just regulate the minimum steady-state length for a valid test run of 15 minutes but also specifies the maximum temperature deviation in a steady state of  $\pm 0.5$  °F (0.28 °C). 30 or more data points are required to be collected within 15 minutes. The time between two data points must be equal. A minimum of for test runs is needed to calculate the IPLV value. This test runs must be conducted at 25%-, 50%- and 75%-part load as well as in full load operation. To allow a suitable comparison with the manufacturer specification, an evaporator flow of 300 *GPM* (18.93 *kg/s*) was necessary. The temperature range and the load steps led to test plan with the target temperatures for the baseline test in Table 16. Since the chiller has a shutdown automatic that stops the operation at loads lower than 30% due to the low oil pressure differential, the lowest test run could not be conducted at 25% and therefore was set higher. The lowest measured test efficiency is then used for an extrapolation to the 25%-load point. The standard [38] describes the procedure in detail. The evaporator inlet temperatures are calculated for an evaporator loop water flow of 300 *GPM* and refer to the required load steps. The evaporator outlet temperature remains constant for all measurements. The condenser inlet temperatures change in three steps as outlined by the AHRI 550/590 Standard [38].

Table 16: Test plan for 125 *RT* (439.6 *kW*) baseline testing

Target Load	Target Capacity	Evaporator Temperatures		Condenser Temperatures
		Outlet	Inlet <sup>1</sup>	Inlet
%	<i>RT</i> ( <i>kW</i> )	° <i>F</i> (° <i>C</i> )	° <i>F</i> (° <i>C</i> )	° <i>F</i> (° <i>C</i> )
30	38 (133.6)	44.0 (6.7)	47.0 (8.3)	65.0 (18.3)
50	63 (221.6)	44.0 (6.7)	49.0 (9.4)	65.0 (18.3)
75	94 (330.6)	44.0 (6.7)	51.5 (10.8)	75.0 (23.9)
100	125 (436.6)	44.0 (6.7)	54.0 (12.2)	85.0 (29.4)

<sup>1</sup> Evaporator inlet temperature calculated from the setpoint temperature and target capacity assuming a flow rate of 300 *GPM* (18.93 *kg/s*)

### 3.1.2 Data analysis

To accurately analyze and compare the collected test data, a reliable data processing procedure must be established. The following steps summarize how the evaluation of the tests at different load conditions of the chiller were carried out. For all the time-dependent data collected, the first step entails identifying suitable steady-state time windows for the given load condition. If suitable steady-state data is identified, then the file is transferred to a csv-format manually and the time frame of the steady-state conditions is separated or highlighted.

Since the measured data is given in IP units and a part of the equations in the analysis requires SI units, the temperature and flow rate data need to be converted. For the temperature, this is done with the equation 3.1.

$$T_{\text{C}} = (T_{\text{F}} - 32) \cdot \frac{5}{9} \quad (3.1)$$

The flow rates that are given in *GPM* are multiplied with a factor that equals the water mass in *kg/s* following equation 3.2.

$$\dot{m}_{\text{kg/s}} = \dot{m}_{\text{GPM}} \cdot 0.063 \quad (3.2)$$

Once this is done, the actual performance evaluation can be carried out. One of the key values of the evaluation is the cooling capacity of the chiller. It is calculated as a product over the mass flow through the evaporator, the specific heat of the fluid and the temperature difference between the inlet ( $T_{E_{in}}$ ) and the outlet ( $T_{E_{out}}$ ) of the evaporator.

$$\dot{Q}_E = \dot{m}_E \cdot c_p \cdot (T_{E_{in}} - T_{E_{out}}) \quad (3.3)$$

Next, a relative chiller load is determined as the ratio of the cooling capacity calculated in equation 3.4 and the nominal design cooling capacity of 125 *RT* mentioned in the chiller specification.

$$\text{Load} = \frac{\dot{Q}_{E_{PL}}}{\dot{Q}_{E_{max}}} \cdot 100\% \quad (3.4)$$

Finally, the efficiency of the chiller is calculated from the measurements. One common efficiency metric is the coefficient of performance (COP) defined as the ratio of the cooling capacity to the electrical power input of the chiller. The Cooling Coefficient of Performance ( $\text{COP}_R$ ), *kW/kW*, is calculated by Equation 3.5.

$$\text{COP}_R = \frac{\dot{Q}_E}{P_{\text{input}}} \quad (3.5)$$

In addition, the AHRI Standard 550/590 [38] defines a chiller efficiency as the ratio of the power consumption of the chiller in kilowatts to the cooling capacity in  $RT$  calculated as given by Equation 3.6.

$$\text{Efficiency} = \frac{P_{\text{input}}}{\dot{Q}_E} \quad (3.6)$$

If the load steps 50%, 75% and 100% cannot be achieved exactly, the efficiency values can be calculated by linear interpolation with the help of the two closest measured values. According to the AHRI 550/590 standard, linear extrapolation is not allowed when there are no test results for a load lower than 25% available. Instead, a degradation correction factor is used as given by Equation 3.7. to obtain the efficiency values at the load range border.

$$\text{Efficiency}_{CD} = \text{Efficiency}_{\text{Test}} \cdot C_D \quad (3.7)$$

By applying this  $C_D$  values to the closest existing test values, the values can be extended to 25%. This degradation correction factor can be calculated based on the load factor LF as in Equation 3.8.

$$CD = (-0.13 \cdot LF) + 1.13 \quad (3.8)$$

The load factor is the ratio of the load at the border load (load-% times the maximum capacity) in  $RT$  over the capacity at the closed test point following the formula 3.9.

$$LF = \frac{\text{Load\%} \cdot \dot{Q}_{\text{max}}}{\dot{Q}_{\text{test}}} \quad (3.9)$$

To allow a comparison of the chillers in part load condition, the integrated part load value (IPLV) is defined by AHRI 550/590. The IPLV can be calculated according to equation 3.7. where A is the efficiency value for 100% load, B for 75%, C for 50% and D for 25%.

$$\text{IPLV.IP} = \frac{1}{\frac{0.01}{A} + \frac{0.42}{B} + \frac{0.45}{C} + \frac{0.12}{D}} \quad (3.10)$$

### 3.1.3 Test results

The necessary 4 reference points could be measured within 4 valid test runs in which a steady state length of between 16 minutes and 35 minutes. The 25% effectiveness value can be extrapolated as described in the previous chapter. The effectiveness for 50%, 75% and 100% cannot be taken directly from the measurement since those are not within 0.2% of the standard

load. To provide an accurate comparison to the manufacturer’s chiller specification, also these efficiency values will be interpolated to the exact target load. All test runs were aiming for the temperature values given in Table 16. Table 17 and Figure 18 shows the measured and processed values in detail. visualizes the chiller efficiency depending on the load level. The green triangles represent the unit efficiency in  $kW/RT$  while the COP is given in with blue circles.

The following sections provide an overview of the conducted test runs. Beside a short description of the tests, the calculated performance values are reported the performance calculation was performed according to the AHRI 550/590 standard [38]. Further thermodynamic data is provided in Appendix I.

Table 17: Summary of the baseline test results

Load	Total operating hours at start	Cond. flow rate	Evap. flow rate	Cond. EWT	Evap. EWT	Evap. LWT	Cooling Capacity	Unit Power	COP	Unit Efficiency
32	144	383.3	299.8	64.79	47.30	44.09	40.32	15.10	9.39	0.3745
51	142	381.3	301.3	64.97	49.18	44.01	64.13	23.74	9.50	0.3702
76	145	382.5	302.1	75.11	51.61	44.04	95.61	49.38	6.81	0.5165
101	153	383.9	300.4	84.78	54.23	54.23	126.56	88.01	5.06	0.6954

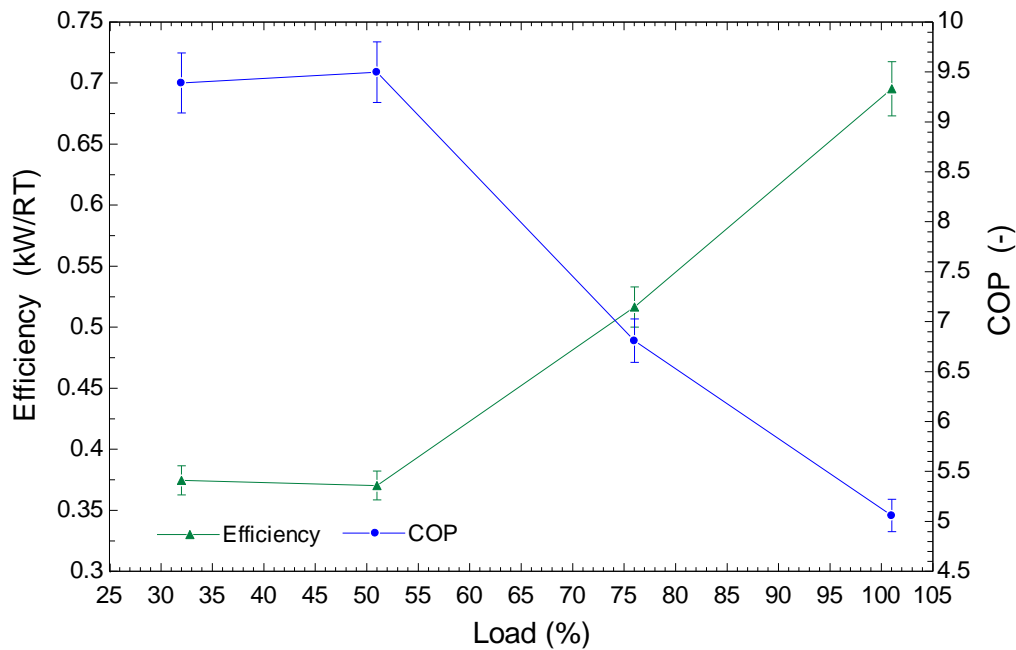


Figure 18: Efficiency values on the baseline test

**32% Part Load (Date: 08/03/2021)**

At the minimum load measurement, the chiller could be charged with 32% load. The measured steady state (Figure 19) had a length of 41 *minutes*. The measured temperature range for the condenser inlet temperature was between 64.66 °F and 65.00 °F (between 18.14 °C and 18.33 °C) and therefore within the allowed range of 65±0.5 °F (18.33±0.28 °C). The evaporator inlet temperatures were measured between 47.24 °F and 47.38 °F (between 8.47 °C and 8.54 °C) and within the allowed tolerance of 47±0.5 °F (8.33±0.28 °C). Also, the evaporator outlet temperature was within the limits of 44±0.5 °F (6.67±0.28 °C) with a range of between 44.03 °F and 44.13 °F (between 6.68 °C and 6.74 °C).

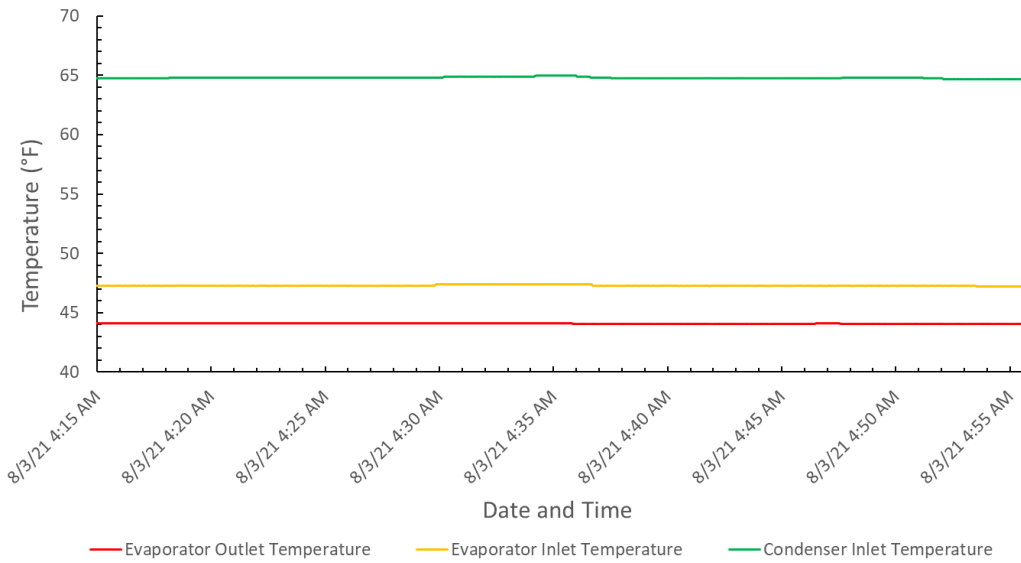


Figure 19: Fluid temperatures during 32% test run

Table 18: Evaluated data at 32% load

<b>Load Rate in %</b>	<b>32</b>
Flow Rate over the Evaporator in <i>GPM</i>	299.80
Mass Flow (Evaporator) in <i>kg/s</i>	18.91
Cooling Capacity in <i>kW</i>	141.81
Cooling Capacity in <i>RT</i>	40.32
Average Temperature in the Evaporator in °C	7.61
Evaporator Inlet Temperature in °C	8.50
Evaporator Outlet Temperature in °C	6.72
Electrical Input Power Value in <i>kW</i>	15.10
Coefficient of Performance COP	<b>9.39</b>
Unit Efficiency according to AHRI 550/590 Standard in <i>kW/RT</i>	<b>0.3745</b>

**51% Part Load (Date: 08/03/2021)**

The second load rating was done at 51% of the 125-RT chiller capacity. The steady state in the measurement could be hold for 35 *minutes*. The condenser inlet temperature had some fluctuation within the recording but with a minimum value of 64.57 °F (18.09 °C) and a maximum value of 65.21 °F (18.45 °C) the deviations where within the tolerance range of 65±0.5 °F (18.33±0.28 °C). The fluctuation also impacted the evaporator inlet temperatures with a range from 49.09 °F to 49.29 °F (9.49 °C to 9.61°C) and the evaporator outlet temperature slightly with a temperature range between 43.89 °F and 44.18 °F (6.61 °C and 6.77 °C). Both stayed within their ±0.5 °F (±0.28 K) limit too.

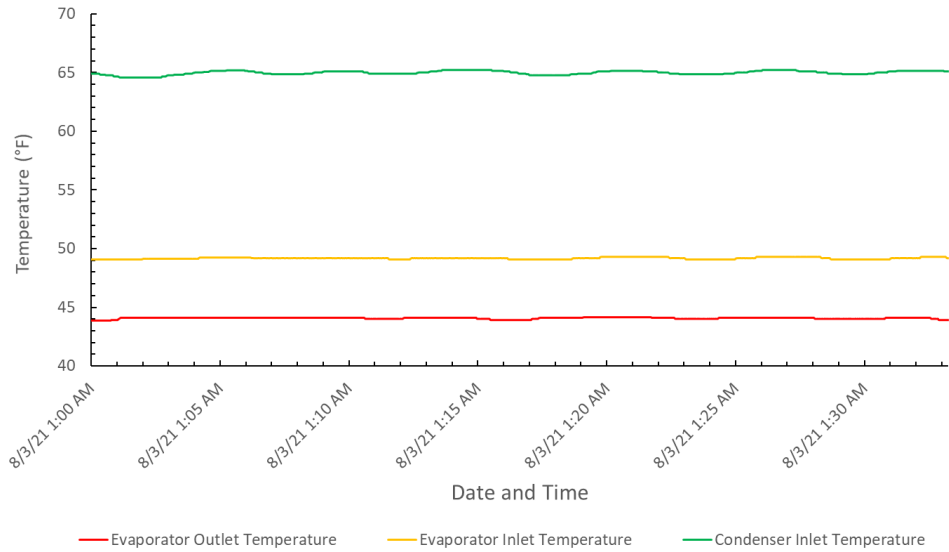


Figure 20: Fluid temperatures during 51% test run

Table 19: Evaluated data at 51% load

<b>Load Rate in %</b>	<b>51</b>
Flow Rate over the Evaporator in <i>GPM</i>	301.30
Mass Flow (Evaporator) in <i>kg/s</i>	19.00
Cooling Capacity in <i>kW</i>	225.53
Cooling Capacity in <i>RT</i>	64.13
Average Temperature in the Evaporator in °C	8.13
Evaporator Inlet Temperature in °C	9.54
Evaporator Outlet Temperature in °C	6.72
Electrical Input Power Value in <i>kW</i>	23.74
Coefficient of Performance COP	<b>9.50</b>
Unit Efficiency according to AHRI 550/590 Standard in <i>kW/RT</i>	<b>0.3702</b>

**76% Part Load (Date: 08/13/2021)**

In the third step, the chiller was charged with 95.61 RT (336.25 kW) which is 76% of the maximum chiller load. The valid steady state with a maximum allowed temperature deviation of  $\pm 0.5$  °F (0.28 K) could be kept up for 30 minutes. The condenser inlet temperatures fluctuated between 74.71 °F and 75.42 °F (between 23.73 °C and 24.12 °C) and therefore was in the tolerance limits. The same is true for the evaporator inlet temperatures which were between 51.49 °F and 51.73 °F (between 10.83 °C and 10.96 °C) and the evaporator outlet temperatures which were between 43.89 °F and 44.18 °F (between 6.61 °C and 6.77 °C).

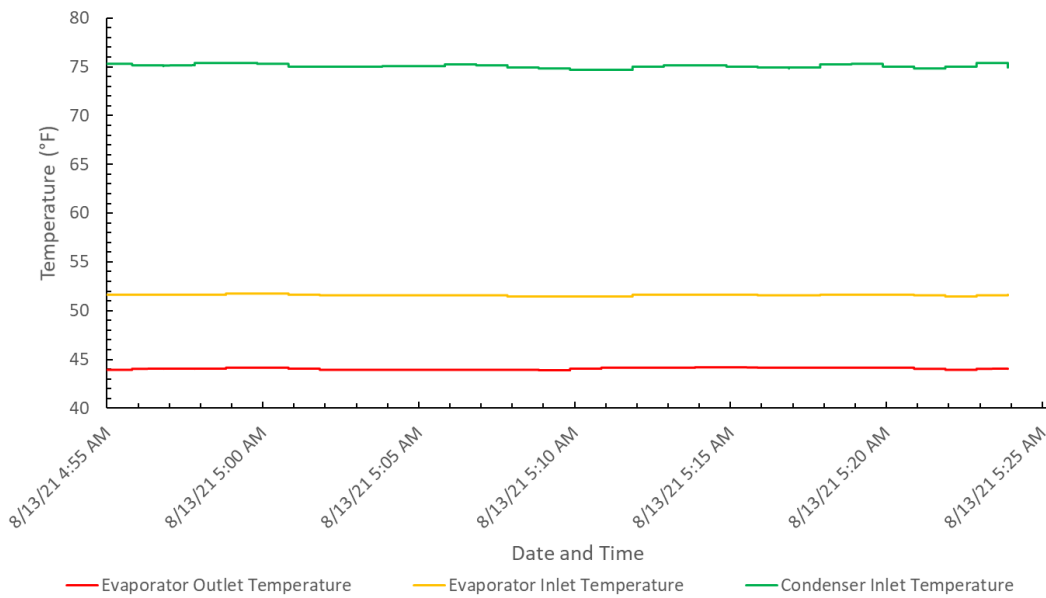


Figure 21: Fluid temperatures at 76% test run

Table 20: Evaluated data at 76% load

<b>Load Rate in %</b>	<b>76</b>
Flow Rate over the Evaporator in <i>GPM</i>	302.13
Mass Flow (Evaporator) in <i>kg/s</i>	19.05
Cooling Capacity in <i>kW</i>	336.25
Cooling Capacity in <i>RT</i>	95.61
Average Temperature in the Evaporator in °C	8.79
Evaporator Inlet Temperature in °C	10.89
Evaporator Outlet Temperature in °C	6.69
Electrical Input Power Value in <i>kW</i>	49.38
Coefficient of Performance COP	<b>6.81</b>
Unit Efficiency according to AHRI 550/590 Standard in <i>kW/RT</i>	<b>0.5165</b>

**101% Full Load (Date: 08/17/2021)**

The highest efficiency rating was done at 101% load. The 101% refer to the 125 *RT* specification. Technically this was possible due to the slightly higher flow rate than specified in the rating of the manufacturer. The values that were measured during the steady state were within the limits for 16 *minutes*. Since the vapor compression system was operating at its maximum the fluctuations were stronger again. The condenser inlet temperature changed between 84.51 °F and 85.26 °F (between 29.17 °C and 29.59 °C) within the test run. The deviations of the evaporator inlet temperature where slightly smaller with a minimum value of 54.11 °F (12.28 °C) and a maximum value of 54.50 °F (12.50 °C). Which a range from 44.00 °F to 44.50 °F (from 6.67 °C to 6.94 °C), also the evaporator outlet temperature reached its allowed borders but was within the limits.

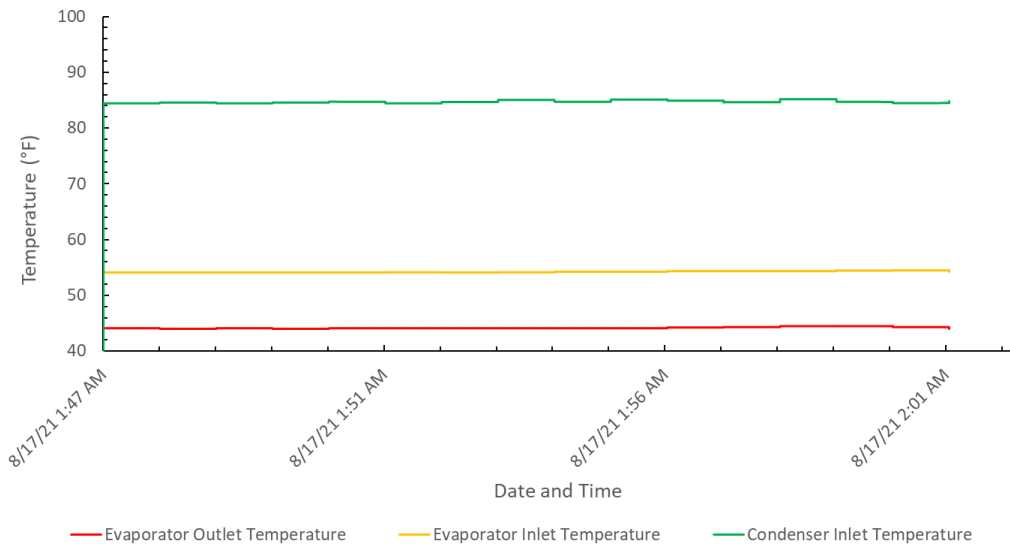


Figure 22: Fluid temperatures at 101% test run

Table 21: Evaluated data at 101% mode

<b>Load Rate in %</b>	<b>101</b>
Flow Rate over the Evaporator in <i>GPM</i>	300.40
Mass Flow (Evaporator) in <i>kg/s</i>	18.94
Cooling Capacity in <i>kW</i>	445.100
Cooling Capacity in <i>RT</i>	126.56
Average Temperature in the Evaporator in °C	9.55
Evaporator Inlet Temperature in °C	12.35
Evaporator Outlet Temperature in °C	6.76
Electrical Input Power Value in <i>kW</i>	88.012
Coefficient of Performance COP	<b>5.06</b>
Unit Efficiency according to AHRI 550/590 Standard in <i>kW/RT</i>	<b>0.6954</b>

### 3.1.4 IPLV value

The IPLV.IP value is the integrated part load value. This number gives feedback over the unit efficiency not just at full load but also in part load operation. The way, how to calculate this value and how to interpolate and extrapolate the related efficiencies is described in section 3.1.2. To gain the IPLV.IP value, the reference values for the efficiency at 25%, 50%, 75% and 100% load are needed. While the values for 50%, 75% and 100% can be interpolated linear, the value for 25% needs to be extrapolated with respect to the requirements from the standard.

The calculations below show the extrapolation for that was done for the 25%-unit efficiency value.

$$LF = \frac{0.25 \cdot 125 \text{ TR}}{40.32 \text{ TR}} = 0.7750$$

$$CD = (-0.13 \cdot 0.7750) + 1.13 = 1.0293$$

$$\text{Efficiency}_{CD} = 0.3745 \frac{\text{kW}}{\text{TR}} \cdot 1.0293 = 0.3855 \frac{\text{kW}}{\text{TR}}$$

Table 22 lists the unit efficiency values from the measurements as well as the interpolated and extrapolated values (bold numbers). The bold numbers are used as a base for the IPLV.IP calculation.

Table 22: Measured and interpolated/extrapolated efficiency values as basis for IPLV calculation

<b>Load</b>	<b>Unit efficiency</b>
%	<i>kW/RT</i>
<b>25</b>	<b>0.3855</b>
32	0.3745
<b>50</b>	<b>0.3705</b>
51	0.3702
<b>75</b>	<b>0.5106</b>
76	0.5165
<b>100</b>	<b>0.6882</b>
101	0.6954

The IPLV.IP value is calculated as described in formula 3.10

$$\text{IPLV.IP} = \frac{1}{\frac{0.01}{0.6882} + \frac{0.42}{0.5106} + \frac{0.45}{0.3705} + \frac{0.12}{0.3855}} = 0.4232 \frac{\text{kW}}{\text{TR}}$$

Figure 23 shows a chart with the unit efficiencies and their related load value. The green triangles represent actual measurements while the red squares represent the interpolated and extrapolated values. The orange marker indicates the efficiency value that is specified by the chiller manufacturer at full load operation. The points are connected by a polynomial trendline.

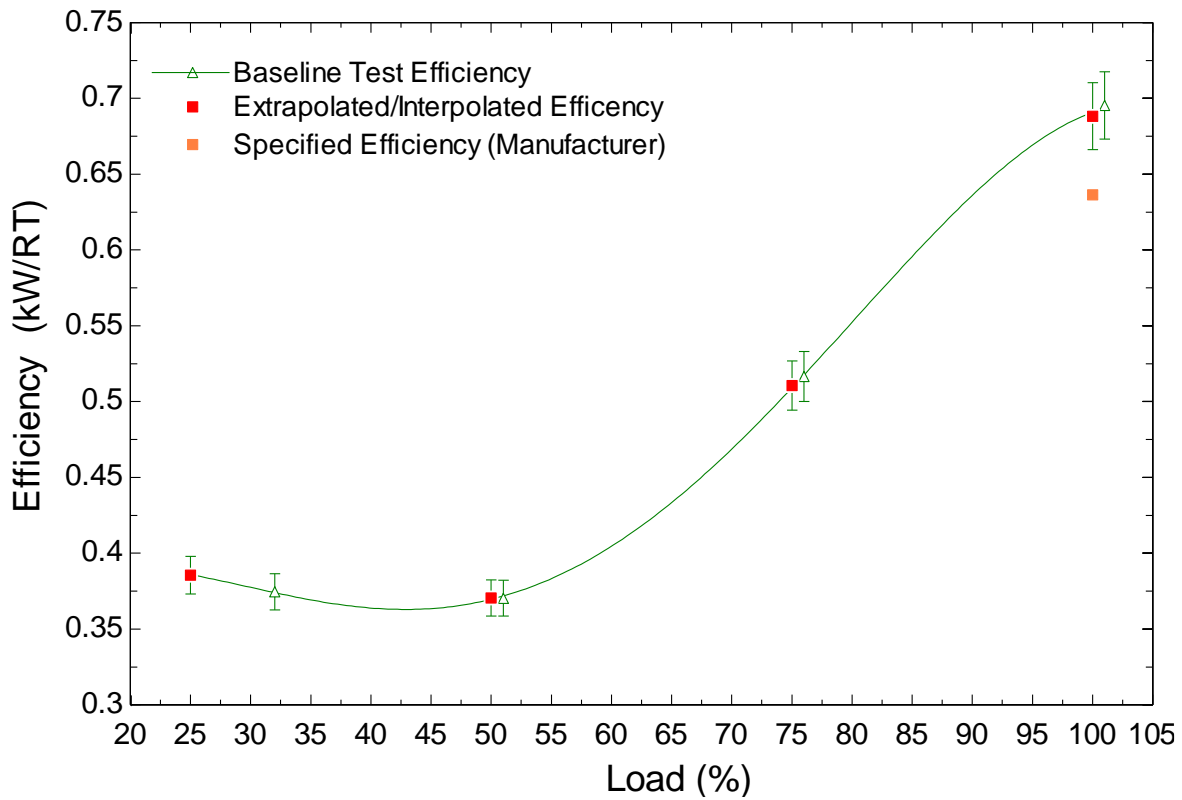


Figure 23: Unit efficiency with interpolated values

Table 23: Chiller efficiency comparison

<b>EFFICIENCY COMPARISON</b>		
	<b>Full load efficiency</b>	<b>Part load efficiency (IPLV.IP)</b>
	<i>kW/RT</i>	<i>kW/RT</i>
Baseline rating	0.6882	0.4232
York specification	0.6363	0.4064
<b>Deviation</b>	<b>-8.16 %</b>	<b>-4.13 %</b>

The deviation at full load results to be 8.16% lower than that given in the manufacturer's specification. As a result, the IPLV.IP value is 4.13% lower than it was evaluated in the measurements. While the deviation in full load efficiency is relatively high (ideally it should have been <5%), the discrepancy in part load efficiency is acceptable.

Overall, there might be various reasons for the measured differences, such as slightly different temperatures (evaporator inlet, evaporator outlet, condenser inlet) within the allowed tolerances in the manufacturer's rating compared to the baseline tests.

If the same result uncertainty of  $\pm 0.02217 \text{ kW/RT}$  that can be seen in Figure 23 is applied to the manufacturer's full load rating point, the highest possible efficiency at the baseline test measurement ( $0.67013 \text{ kW/RT}$ ) and the lowest possible efficiency at the manufacturer measurement ( $0.65847 \text{ kW/RT}$ ) just deviate 1.8% from each other.

Another reason could be the begin of a fouling process in the test stand chiller. Even if the overall number of operating hours is relatively low (162 hours) the shell and tube heat exchangers of the chiller are already exposed to the untreated water for almost 2 years. The fouling factor is the additional thermal resistance that is created due to the accumulation of contaminants on a heat exchanger surface [46]. According to the guideline [44] can be calculated by first calculating the overall heat transfer coefficient (U) with the heat transfer rate (Q), the area (A) and the logarithmic mean temperature difference (LMTD) as explained in Equation 3.11. By using the heat transfer coefficient, the overall thermal resistance (R) can be calculated with Equation 3.12. Finally, the fouling factor ( $R_f$ ) can be extracted with Equation 3.13 from the overall thermal resistance if the water-side heat transfer coefficient ( $h_w$ ), the tube material resistance ( $R_m$ ) and the refrigerant heat transfer coefficient ( $h_r$ ) is known.

$$U = \frac{Q}{A \cdot \text{LMTD}} \quad (3.11)$$

$$R = \frac{1}{U} \quad (3.12)$$

$$R = \frac{1}{h_w} + R_f + R_m + \frac{1}{h_r} \quad (3.13)$$

An approach to calculate the fouling factor based on a heat exchanger NTU model for the shell and tube heat exchangers of the chiller failed due to the high accuracy of the searched value. The fouling factor limitations are between 0.000 and  $0.001 \text{ hr} \cdot \text{ft}^2 \cdot \text{°F/Btu}$ . This values accuracy

could not be reached since the heat exchanger model was unvalidated and significant dimensions of the heat exchangers are unknown.

To create a base for future fouling calculations, the thermal properties of the temperature levels in the heat exchangers (Figure 24) during the baseline tests and during the recurring performance testing were investigated and the logarithmic mean temperature difference or LMTD (Figure 25) was calculated for the operating conditions.

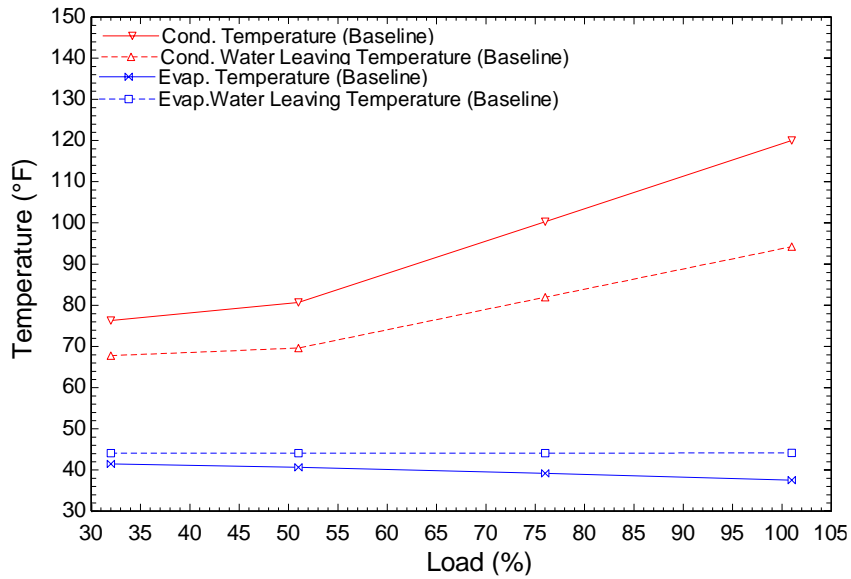


Figure 24: Fluid temperatures during the baseline test runs [48]

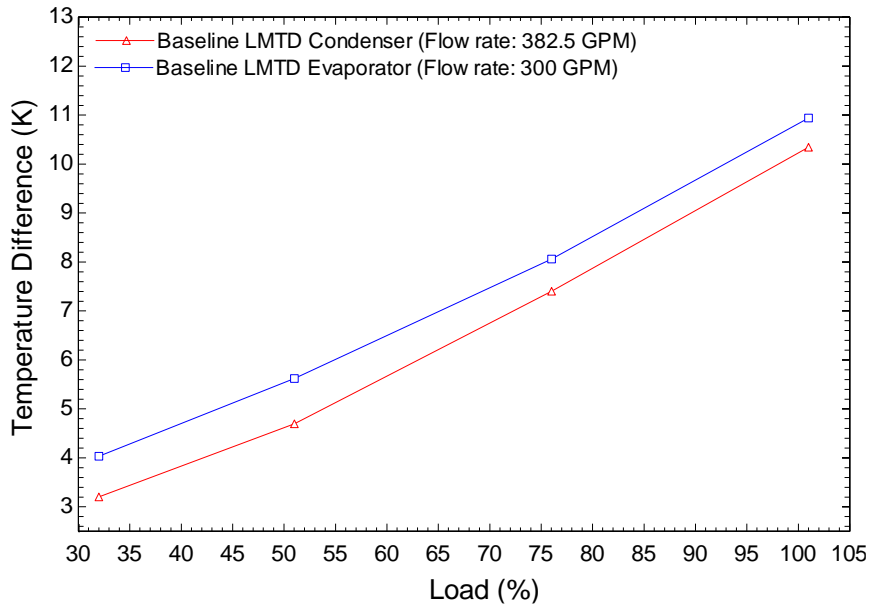


Figure 25: LMTD of the evaporator during the baseline test runs [48]

## 3.2 Accelerated life testing

### 3.2.1 Cycle assumptions

To gain a deeper understanding of the performance degradation of a twin-screw chiller in real life operation, an accelerated life test methodology was developed. Most of the chiller testing is done according to standards and it is well documented. However, accelerated life testing of large capacity refrigeration machines has not been extensively covered in the literature. In fact, most of studies performed simulated analysis and projections on extended operation of chillers under accelerated loading conditions. The studied literature showed that for an accelerated life testing, a usage cycle must be clearly defined based on real operating factors or conditions and if this is not possible, clear assumptions must be made. For HVAC applications, constant usage cycles are hard to define since the application is season and weather dependent. That is why seasonal functional usage cycles [25] were introduced to flatten out peaks in specific seasonal load modes.

The special thing on chillers is, that based on the application, their operation modes and usage cycles offer even more degrees of freedom. Dependent on if a chiller is set up in a single chiller configuration or in a chiller plant, the operation could be in continuous high load operation, characterized start-stop modes, large load fluctuations, or even a lot of downtime (for redundant chillers). Another factor is the chiller control from the building automation side that can severely impact the annual operating hours of a chiller. All these facts, show that an ALT that represent most chiller life is hard to create based on a real chiller's life data.

Still, with the support of our industry partner, a chiller application case was defined in which the chiller has 5.5 Start-Stop intervals per day. The value comes from the idea that one year of chiller operation should be simulated in about 12 *weeks* of continues ALT and one usage cycle should take one hour. To cover a high variety of applications and to load stress on the system, the operating modes within this 1 *hr* usage cycles should simulate extreme operating conditions in steady or almost steady state.

### 3.2.2 Test requirements

To implement an accelerated life cycle testing, different operating modes were investigated to induce increased mechanical stress on the components, in particular the compressor, without altering the correct operation of the chiller (e.g., decrease oil-injection rate, change lubricant oil,

among others). The life cycle testing should emulate the field operation of the chiller. Based on these considerations, three major mechanical behaviors have been identified to have significant impact on the chiller operation:

- increased friction during the start-up of the compressor
- increased mechanical stress due to higher torques at high load operations
- decreased lubrication due to decreased differential pressure.

These three operating conditions were included in two separate loading profiles which are described in the following sections. During the initial phase of the accelerated life cycle testing, each of the test modes is continuously applied for 2 weeks before switching to the other test mode. Moreover, every 8 weeks, a recurring baseline test is conducted to verify the impact of the repeated loading cycles on the chiller performance. The implementation and control of the repeated loading cycles have accomplished in LabVIEW [47] by a means of a virtual instrument (VI) that uses time loops for the restart of the cycles. The details of the control strategy as well as safety features will be covered in the next sections.

### 3.2.3 Test modes

#### *High Load/Low Head*

The first developed test mode is the *high load/low head mode*. As the name suggests, this test mode aims at achieving high mechanical stress due to repeated high load operation. In particular, during each cycle, the chiller is run at full capacity for a certain amount of time and then ramped down to zero load condition and then ramped up to full load. The setpoint of the chiller remains at 44 °F (6.67 °C), the evaporator inlet temperature target is 54 °F (12.22 °C). The chiller inlet temperature was selected specifically low at 60 °F (15.56 °C). Figure 64 in Appendix II shows the single state points drawn in a p-h diagram for R-134a. Due to the low head, i.e., low pressure gradient between condensation pressure and evaporation pressure, the flow of lubrication oil in the compressor is reduced because the lubrication system relies on this pressure difference and does not have an electric oil pump. Every hour, the operation is interrupted by a shutdown of the chiller, followed by an almost immediate startup. With this ON/OFF-set, the friction that is higher at the start up for screw compressors should act on the system. Figure 26 shows the idealized load curve for the high load/low head-mode.

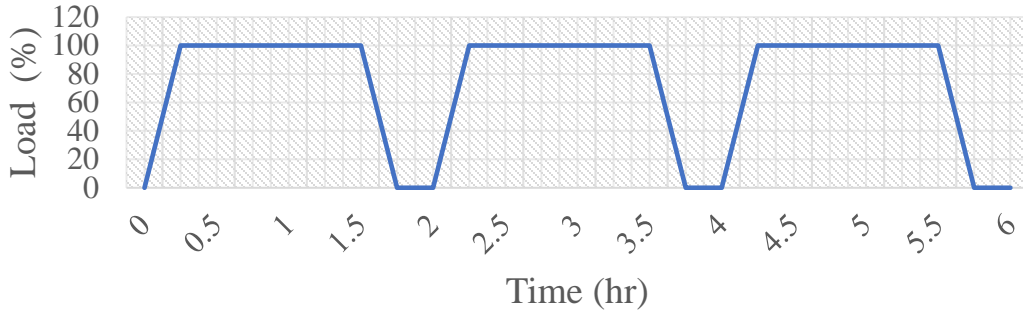


Figure 26: Ideal load curve for high load/low head operation

During the testing, not all target temperatures could be maintained exactly as Figure 27 shows. A stable operation at exact 100% was not possible to realize in long term operation without increasing temperatures. The evaporator inlet temperature fluctuates between 52.5 °F and 54.0 °F (between 11.39 °C and 12.22 °C). Therefore, the chiller operates at about 95% with small fluctuations. The condenser inlet temperature was set higher to 65 °F (18.33 °C). This was necessary since otherwise, low peaks in the temperature control can lead to a shut down in long term operations. Until today, the mode was processed for 336 hr (status 11/30/2021). The OFF-section time could be reduced from the initially planned several minutes to one minute. This time was evaluated after a test run that showed that 60 seconds were enough to shut the system down.

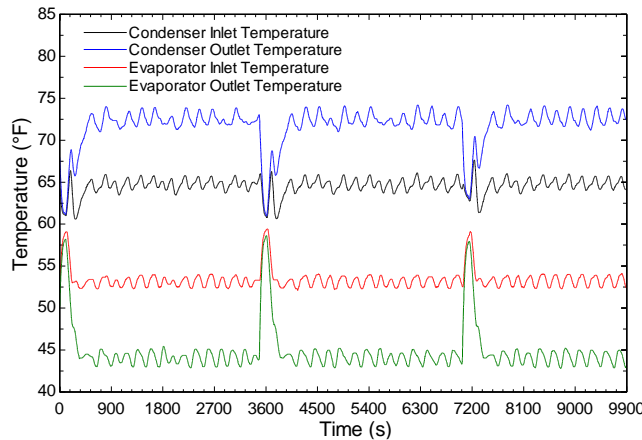


Figure 27: Temperature during operation in high load/low head-mode

A check of the oil pressure values (Figure 27) in comparison with the values during AHRI Standard 550/590-conform operation showed, that a significantly lower oil pressure existed in the

system during the test sets. That supports the initial assumption of additional friction and mechanical wear in this mode.

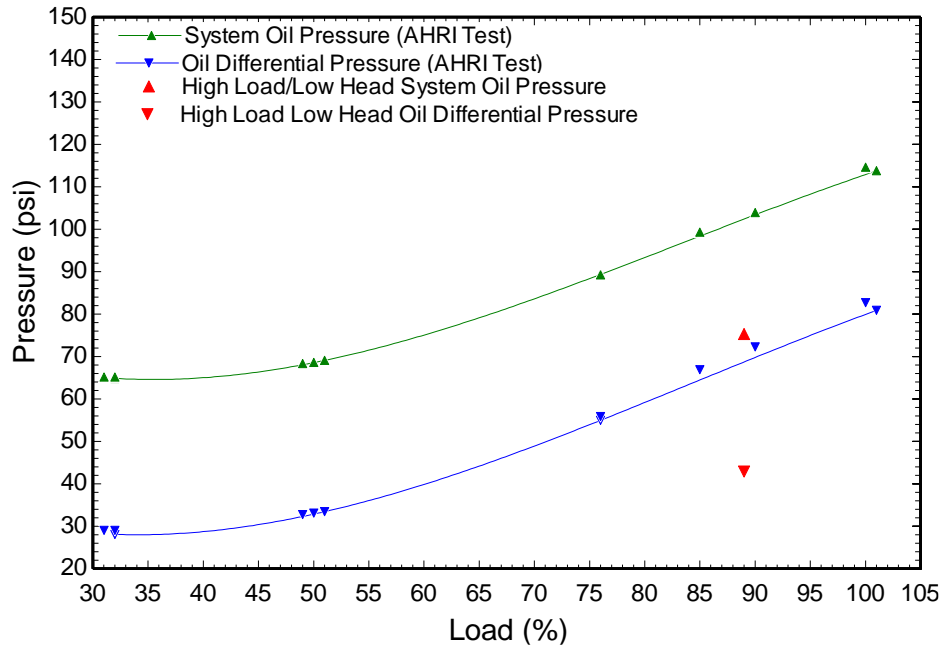


Figure 28: Oil pressure and oil differential pressure during the high load/low head-mode [48]

### ***Low Load/High Head***

The second test mode that was selected is the *low load/high head mode*. In this operating mode, the compressor experiences an increased friction due to part load operation along with the mechanical stress resulting from the high-pressure gradient. The minimum load achievable during operation was set equal to 35%. The chiller setpoint remains at 44 °F (6.67 °C) while the target evaporator inlet temperature is 47.5 °F (7.61 °C). The target temperature for the condenser inlet is 90 °F (32.22 °C). This condenser inlet temperature is selected to avoid the automatic shutdown of the chiller at temperatures above 95 °F (35.00 °C). Figure 65 in Appendix II shows the single state points drawn in a p-h diagram for R-134a. Similar to the previous operating mode, the chiller operation is interrupted by ON/OFF-intervals every hour. The idealized operation curve is shown in Figure 29.

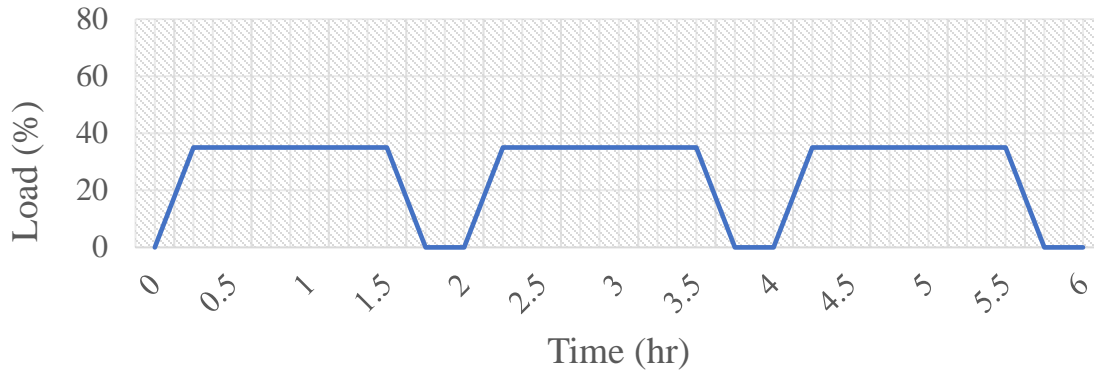


Figure 29: Ideal load curve for low load/high head-operation

Also in this mode, the parameters needed to be adjusted during the actual testing. The condensing temperature was set to  $88\text{ }^{\circ}\text{F}$  ( $31.11\text{ }^{\circ}\text{C}$ ). So, a high temperature shut down of the chiller could be avoided in long term operation. This problem was caused by temperature control peaks. The high condenser inlet temperature caused slightly higher evaporator outlet temperatures of  $44.5\text{ }^{\circ}\text{F}$  ( $6.94\text{ }^{\circ}\text{C}$ ) and also the load level needed to be raised for a reliable operation to 40% so the evaporator inlet temperature was  $49\text{ }^{\circ}\text{F}$  ( $9.44\text{ }^{\circ}\text{C}$ ). The fluid temperatures can be seen in Figure 30. Until today, the mode was operated for  $294\text{ hr}$  (status 11/30/2021). The hourly OFF intervals could be reduced to a length of 1 minute after a test run that showed that this is enough time to bring the compressor to a stop without producing a too big energy change.

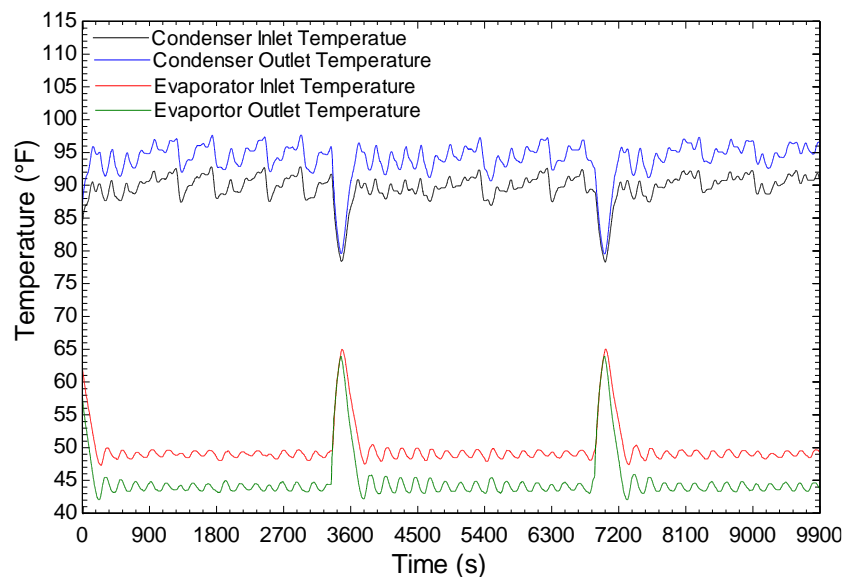


Figure 30: Temperature during operation in low load/high head operation [48]

A plot of the temperatures detected by the motor sensors (Figure 27) in comparison with the values during AHRI 550/590-conform operation clearly shows that the motor temperatures are much higher than under performance test conditions and therefore fulfill the aim of an increased wear of the electrical components over time.

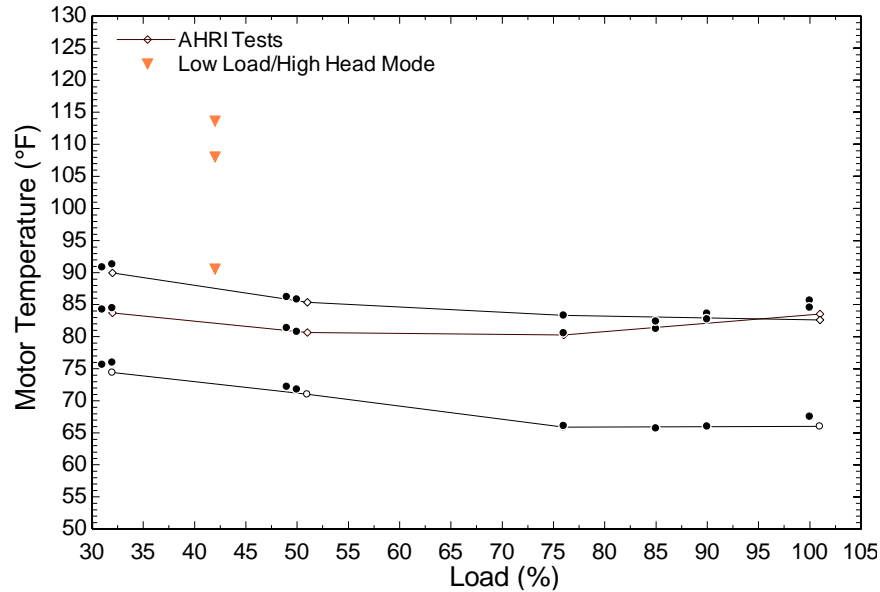


Figure 31: Motor temperatures during low load/high head operation [48]

### 3.2.4 Development of the test mode and test stand automation

The accelerated life testing requires continuous operation during the entire testing time which entails unsupervised testing and the need for ensuring correct and safe operation of the chiller. To enable continuous operation in the laboratory environment, the system required the implementation of a control strategy to impose the cyclic loading to the chiller and safety measures in case of unwanted conditions or other unforeseen circumstances, e.g., loss of power or internet communication. As a first step, the two test mode procedures have been implemented in LabVIEW [47]. To this end, a case structure was implemented within a timed cycle for every test mode. Depending on the preadjusted time since the test interval, the implemented logic switches between the load operation (ON-interval) and the shutoff period (OFF-interval) in an endless loop, unless the test run is stopped. The output values of each case are the evaporator inlet temperature and the condenser inlet temperature since these are the only quantities that are impacted by the control strategy of the test stand during testing mode change intervals. The timed loops of the test modes in the LabVIEW code always run parallel to each other in at the same time. The selection

of which temperature values should be transferred to the system automatically dependent on the test mode selection in the graphical user interface (GUI) in Figure 32. Regarding hardware control, Figure 33 illustrates the three main control loops and the controlled parameters. The first two categories, i.e., temperature control and flow control, are valve controls while the error detection required a risk and failure analysis.

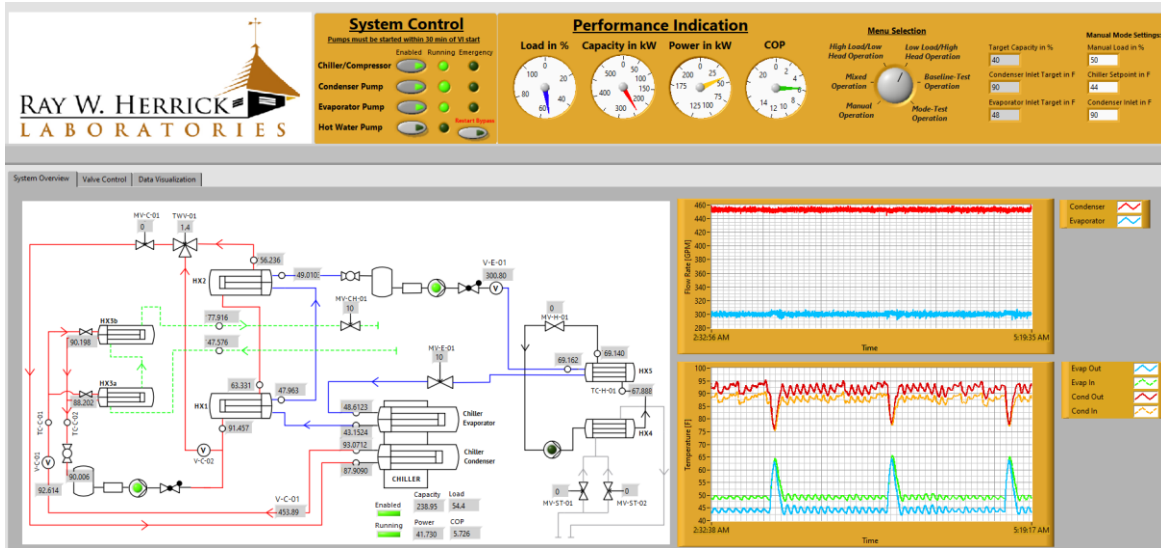


Figure 32: GUI of the test stand controls in LabVIEW [47]

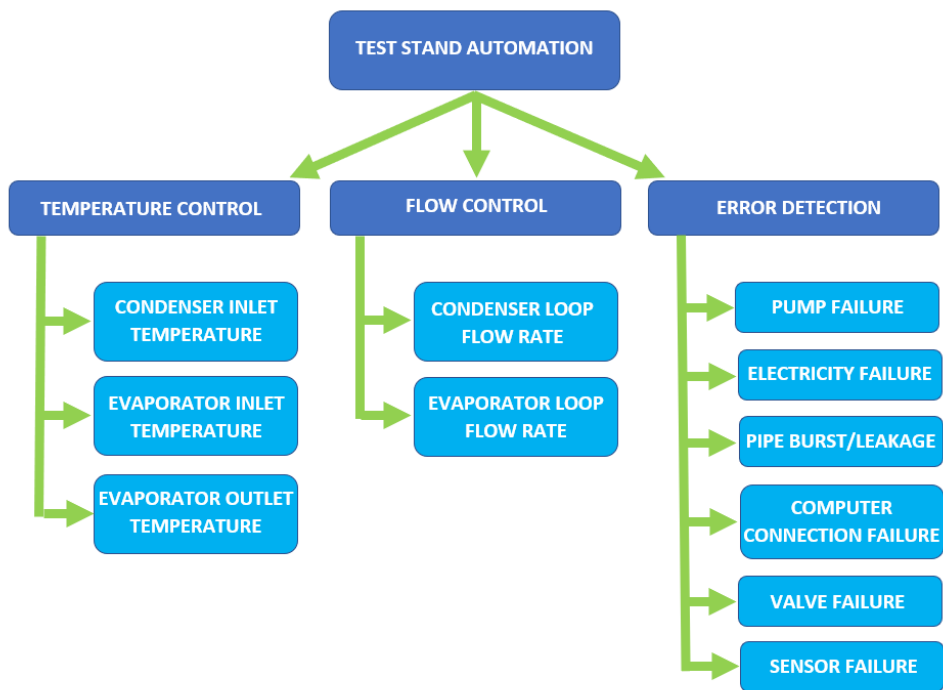


Figure 33: Implementation of the test automation

The temperature at the condenser inlet is controlled by the chilled water flow through the heat exchangers HX3a and HX3b in the system (refer to Figure 15). The chilled water flow can be regulated by the flow control valve MV-CH-01. Since the valve position directly influences the water temperature at the condenser inlet, a feedback control was created with an PID in LabVIEW [47]. Figure 34 shows the control scheme that was applied. The two input values are the setpoint for the condenser inlet temperature which is provided by the timed loops that control the test modes. The second input value is the actual temperature at the condenser inlet which is measured by the temperature sensor RTD-C-02. The PID-function compares these values and adjusts the valve position according to the temperature deviation by giving out a 0-10 V signal to the valve. Depending on the system response, the change is adjusted so that the temperature remains constant within a certain threshold. The control of the evaporator inlet temperature works in a similar way. The evaporator inlet temperature depends on the position of the three-way valve TWV-01. As more water flow is directed through the internal heat exchangers HX1 and HX2, the evaporator inlet water temperature increases. By referring to the control scheme of Figure 34, the temperature setpoint is provided by the case structure of the test modes depending on the current temperature target while the temperature input signal comes from the temperature sensor RTD-E-02 that is positioned on the evaporator inlet. The PID block compares these values and generates an 0-10 V output signal that is continuously readjusted based on the process temperature that is measured on RTD-E-02.

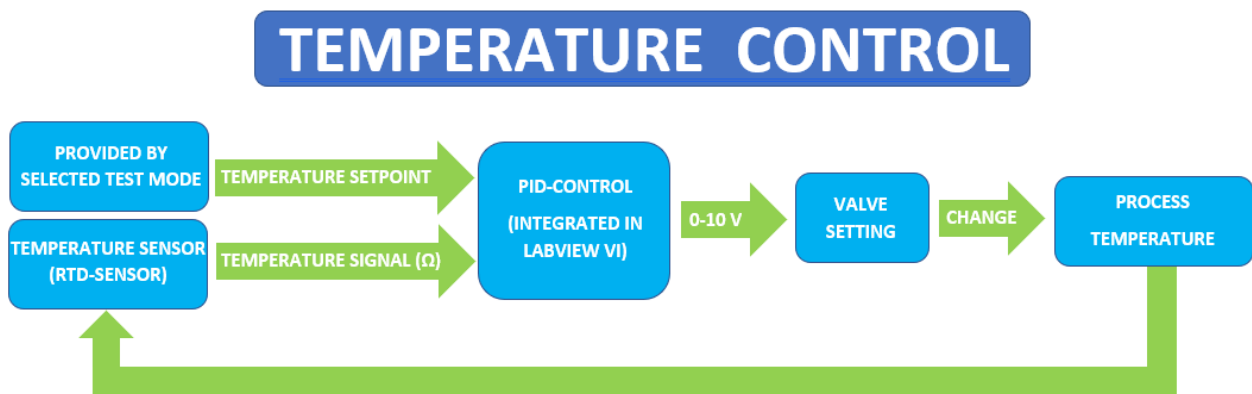


Figure 34: Temperature control scheme

The last temperature control is the evaporator outlet control which is also the chiller setpoint. This temperature can simply be adjusted in the GUI and is transferred to the chiller by a 0-10 V signal. The internal control logic of the chiller modulates the compressor speed to meet the load requirement.

Like the temperature control, the flow control also employs a PID controller. The target flow rate can be adjusted on the user interface. The actual flow rate value is provided to the PID by the electromagnetic flow meters which is V-C-01 in the condenser water loop and V-E-01 in the evaporator water loop via a 4-20 mA signal. The PID calculated an adjustment of the flow if necessary and gives out a 0-10 V signal to change the valve position. The valve MV-C-01 allows a reduction of the flow in the condenser water loop while the valve MV-E-01 can reduce the flow in the evaporator water loop. Feedback is given to the PID by the new measured flow rate that is sensed by the flow meters. The flow control is usually not active since the flow rate in the loops do not significantly change due to the fixed speed pumps.

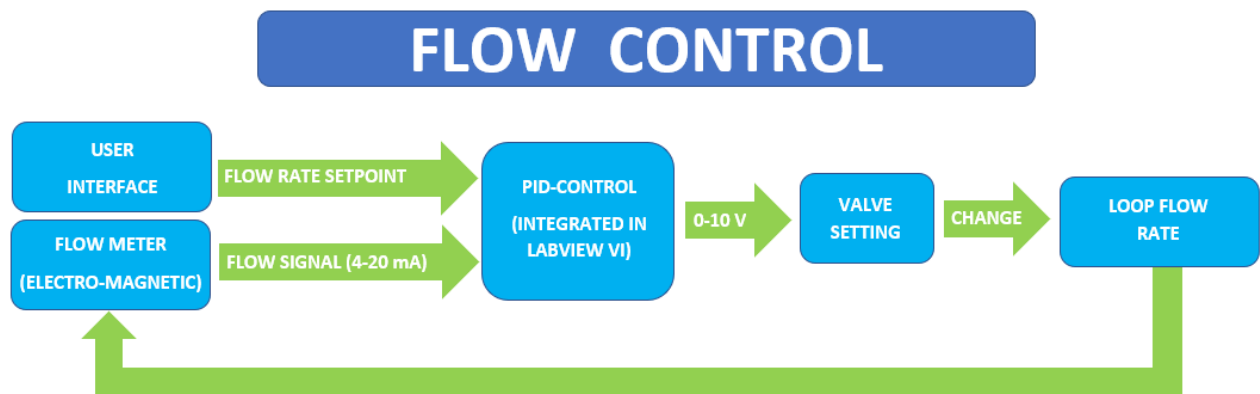


Figure 35: Flow control scheme

The PID components in the LabVIEW VI require the three gains to provide the correct output value reaction based on the input signal:

- Proportional gain ( $K_c$ )
- Integral time ( $T_i$ , min)
- Derivative time ( $T_d$ , min)

To this end, the valve position was logged during the commissioning test runs where the valve adjustment was carried out manually. With the help of a MATLAB script and a Simulink model [50] a control model could be selected from and applied to the Simulink model. From there

the PID gains could be directly retrieved. There are not constant values in use. The PID gains change with the operating mode and the valve readjustments. Also, the values are tuned after a few days of test runs to perform more accurate. Therefore, the input and output values are again applied to the MATLAB script and the Simulink model [50]. The results are slightly different gains that provide a control with a higher accuracy.

To enable continuous unsupervised testing of the chiller, a safety control strategy had to be developed and implemented to detect potential errors or faults. The system operation was analyzed in detail to identify potential risks and mitigation strategies. The chiller itself does not represent a major element of concern since it is a commercial product and has built-in safety controls in case of runaways or unexpected faults. However, the system apparatus used to drive the chiller to the desired loading conditions (i.e., secondary loops and related hardware) has several sources of potential faults. One of the major risks is a pump failure. For instance, there could be a situation where at least one of the pumps does not deliver a constant water flow. A partially reduced or complete absence of water flow rate on the evaporator side could lead to frost formation on the heat exchanger tube what can further lead to a frost damage and the escape of refrigerant to the atmosphere. On the condenser side it could lead to an extremely high refrigerant pressure with a component damage. Also, a pump malfunctioning could be caused by electrical issues that could cause harm to the operator. To avoid these issues, the chiller includes its own internal flow measuring devices and safety regulations. If the flow drops below a minimum threshold, the chiller shuts off immediately. To monitor the operation of the pumps, the flow measurements are included in the LABVIEW VI and integrated into the control strategy. If the measured flow rate drops below 100 *GPM* (6.31 *kg/s*) for more than 5 seconds, the pump with the error and the chiller are stopped to avoid further damage. The other pumps are stopped after 5 more minutes. To avoid that this safety feature impacts the use of the control negatively, there is a function installed that bypasses this safety feature for the first 5 minutes of the run time since there are usually some measurement peaks in the first minutes. That means, the user needs to stay at the system for 5 minutes and then it can run autonomously.

The loss of electrical power to the entire experimental setup could also be another major issue. This is a realistic scenario since the power grid of the laboratory space is a few decades old and the main powerline to which the system is connected to is operating close to its maximum capacity. Also, the damage of a circuit breaker could lead to a breakdown of one or more components. If an

electricity failure shuts down all components including the data acquisition and controls, the test data is safe since it continuously logs the data on a local memory and back-up on a cloud platform every 15 minutes. If only the power supply to the computer or the data acquisition fails, the relays switch to their OFF position so that the chiller and the entire experimental system does not continue to run. In case the chiller is the only component with an electrical fault, the pumps will shut down after 30 minutes without chiller operation. If the chiller is without power for a longer time, the internal chiller controls will also not allow a start before the oil is heated up to operating temperature and therefore no significant amount of refrigerant is solved in the system anymore. A computer connection failure is treated similarly to an electrical problem. If the connection with the computer interrupts and cannot be redistributed, the relays of the system switch to OFF position. No system run is possible without controls.

The secondary loops have been built with thick-wall PVC pipes with screwed, flange and adhesive connections. During operation, the combination of water pressure and vibrations could yield to minor or major leaks. If a leak is not detected early enough, a catastrophic failure could cause significant loss of fluid in the space. In turn, this would cause a drop of the flow rate and the low flow rate emergency shutdown would engage, as previously discussed. That means the pump in the damaged loop as well as the chiller stop running immediately, and the other pump stops shortly thereafter. The operating temperatures during test operation are not to exceed  $95\text{ }^{\circ}\text{F}$  ( $35\text{ }^{\circ}\text{C}$ ), upon which the chiller would shut down due to internal safety control logic. To be noted is that such a temperature level does not cause a problem to the personnel. Also, the lower temperature border is currently at  $44\text{ }^{\circ}\text{F}$  ( $6.67\text{ }^{\circ}\text{C}$ ) which is not a problem. The chemical inhibitors that are used for water treatment and the optional used propylene glycol are not a danger for the environment due to the low concentration. If skin is exposed to them the person should wash or shower the fluid off. In case there is a reaction a medical doctor should be consulted.

The control system relies on the actuation of valves. Valve failures happen usually due to mechanical problems such as a broken pinion gear on the valve linkage of the motor. In case of such an error, there is no direct way to monitor this problem since the valve motor does not give feedback of its position, but the valve issue can be addressed indirectly. If a valve does not move anymore or does not reach the desired position the controlled temperature or flow raises or drops without counteraction. Within a short time, a frame that usually leads to a shut off of the chiller,

followed by a stop of the pumps. So due to the internal safety measures of the chiller, valve problems are not a significant danger.

A breakdown of a sensor can have several reasons, either a cable broke, the sensor has a malfunction, or a connection is loose. If that happens, the controls do not gain a signal anymore. This leads to the shutdown of the test stand.

The described logics help to detect errors and malfunctions and can shut down the system if the situation is dangerous for the user or the system itself. Therefore, the long-term operation can be maintained as safe as possible. Still, the safety logics are never considered as complete, the system is regularly reinvestigated for potential problems and threats so that safety can be improved. Currently not activated but included in the LabVIEW VI is also the option to get an email notification from the system if an emergency shutdown happened. There is also the plan to provide temperature measurements of the pump motors in the future so that a fault can be detected before the pump breaks. The safety measures and logics are supplemented by a daily visual check of the system that focuses leakage by checking pipe connections and water loop pressures.

As mentioned, the GUI allows the adjustment of all important variables during the run and gives detailed feedback of the system condition. Figure 32 shows the user interface with the main controls in the orange field at the top that includes the main switches for the chiller and the pump with a feedback light that indicates operation and a red light in case of an error. Right of that are four gauges (Figure 36) that give a quick overview of the current load in %, the capacity in *kW*, the power consumption in *kW*, and finally the COP under the current conditions. These indicators are placed to give a first impression on the system operation. Right of that is a selection knob (Figure 37) to control the test mode menu. Besides the two described test modes there is the possibility to run the system manually with the input values on the right, another option is a mixed operation that follows a pre-defined load curve. Also, a selection for a baseline test can be made. This mode runs the chiller through all baseline load and temperature conditions. And the last one is a mode for open configurations.

Below this dashboard with the control options, there is a PI-diagram (Figure 38) of the system that includes the measured temperatures and flow rates at the position of the sensor in the system in real time as well as the valve position and feedback of the pump operations.

Right of the PI-diagram is a visualization (Figure 39) of the flow rates and the water temperatures on the chiller inlets and outlets.

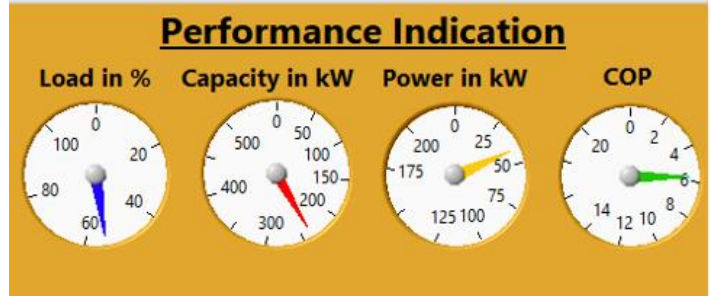


Figure 36: Indicator details of the GUI [47]

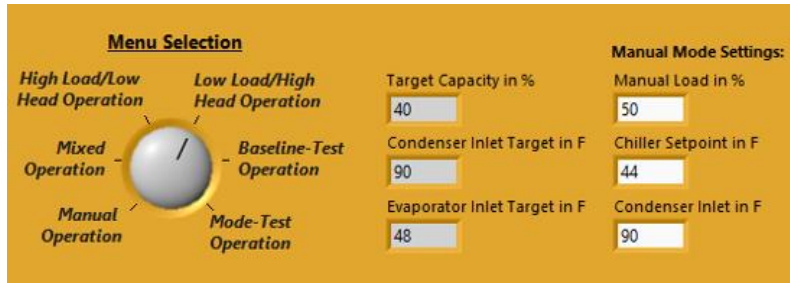


Figure 37: Test menu selection [47]

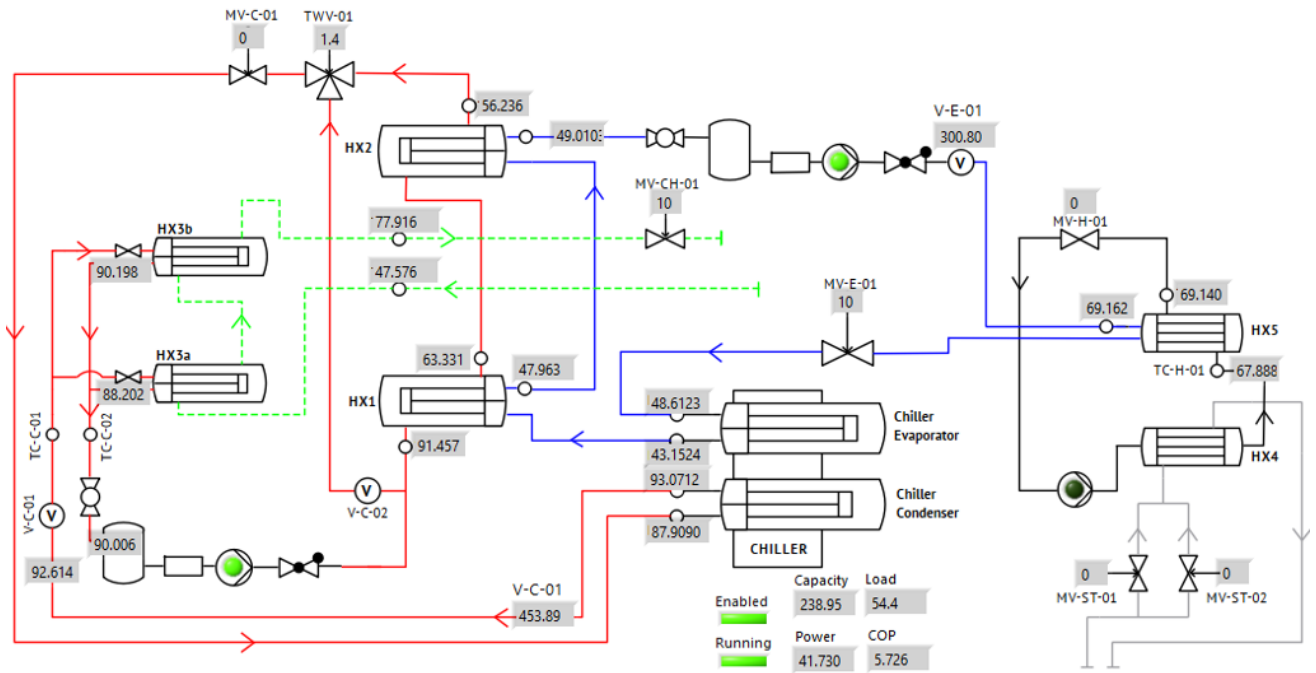


Figure 38: PI diagram with real time measurement indicators in the GUI [46]

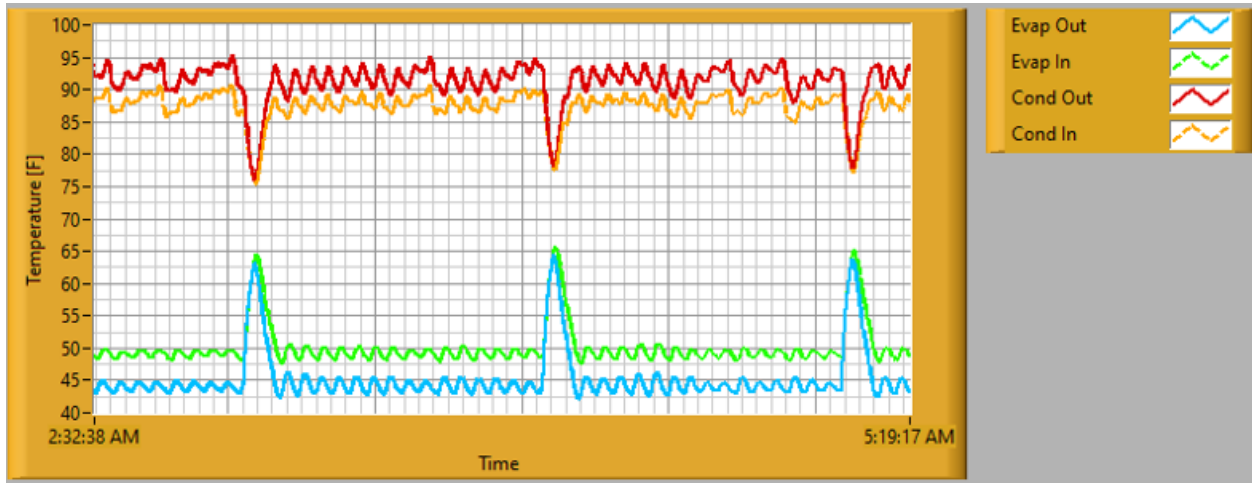


Figure 39: Real time temperature visualization [47]

### 3.3 Recurring baseline testing

To keep track of the performance degradation over time, regular performance tests are necessary. The recurring performance tests are executed after every 1000 operating hours in the accelerated life testing. It is an aim, that both test modes are proceeded 500 *hr* each in that interval. All load levels, the tolerances and the result analyses and processing for this performance test follow the AHRI 550/590 [38] standard and the procedures described in 3.1. This allows a comparison with the initially produced efficiency baseline as well as other system values at every time and avoids deviations based on the operating environment. By overlaying the measured values with the baseline, upcoming deviations, changes in the operating behavior and performance degradation can be identified early on.

After about 6 weeks in the accelerated life test cycles, the first recurring baseline test could be proceeded. There were 8 test runs performed within the allowed tolerances. The load steps were defined close-meshed on purpose to better define the shape of the characteristic compressor line in all load areas. The test results and operating variables are given in Table 24. More details from the tests can be obtained from Appendix III. Figure 40 shows the comparison for the interpolated/extrapolated efficiency according to AHRI 550/590 [38]. The values almost line up at all 4 reference load stages. Just the 100% load values deviate. This deviation can be referred to different operating temperatures during the test runs within the tolerance.

Table 24: Summary of the 1000 h-test results

Load	Total operating hours at start	Cond. flow rate	Evap. flow rate	Cond. EWT	Evap. EWT	Evap. LWT	Cooling Capacity	Unit Power	COP	Unit Efficiency
%	hr	GPM	GPM	°F	°F	°F	RT	kW	-	kW/RT
31	1,120	384.3	300.4	64.92	47.06	43.93	39.27	138.10	9.38	0.3749
32	1,122	383.6	300.4	64.95	47.06	43.89	39.82	140.03	9.65	0.3646
49	1,119	381.4	300.6	64.85	48.97	44.07	61.69	216.96	9.75	0.3608
50	1,116	383.5	301.0	65.00	48.95	44.02	62.07	218.30	9.57	0.3657
76	1,118	382.5	299.9	75.02	51.38	43.80	95.10	334.44	6.79	0.5183
85	1,117	382.0	300.7	79.10	52.37	43.91	106.44	374.34	5.87	0.5995
90	1,131	382.8	300.8	81.00	52.84	43.87	112.93	397.16	5.51	0.6379
100	1,140	381.0	302.1	84.97	54.02	44.13	125.01	439.62	4.99	0.7042

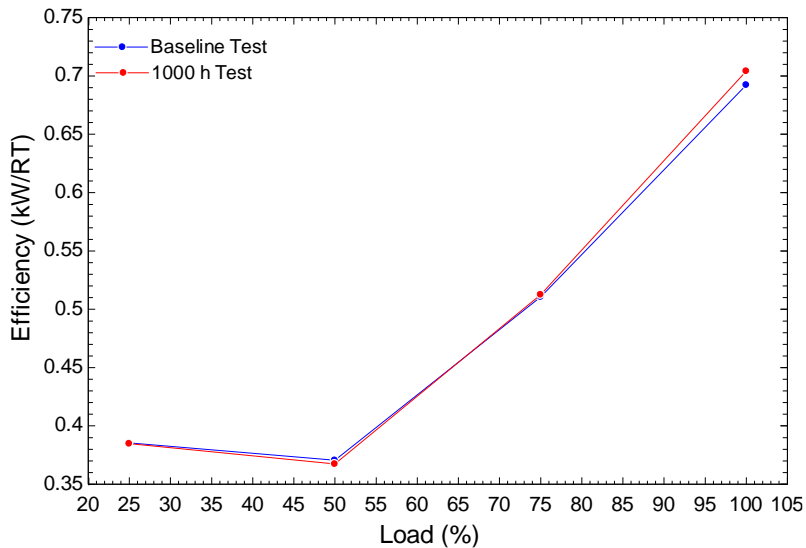


Figure 40: Comparison of measured efficiencies over a baseline test vs 1000 h-test

In Figure 41, the efficiency values that were calculated from the 1000 h-test were plotted over the characteristic line from the baseline tests. Almost all efficiency values line up with a very small or no deviation. The biggest difference exists for the 100% load efficiency values, but they are still within the tolerance.

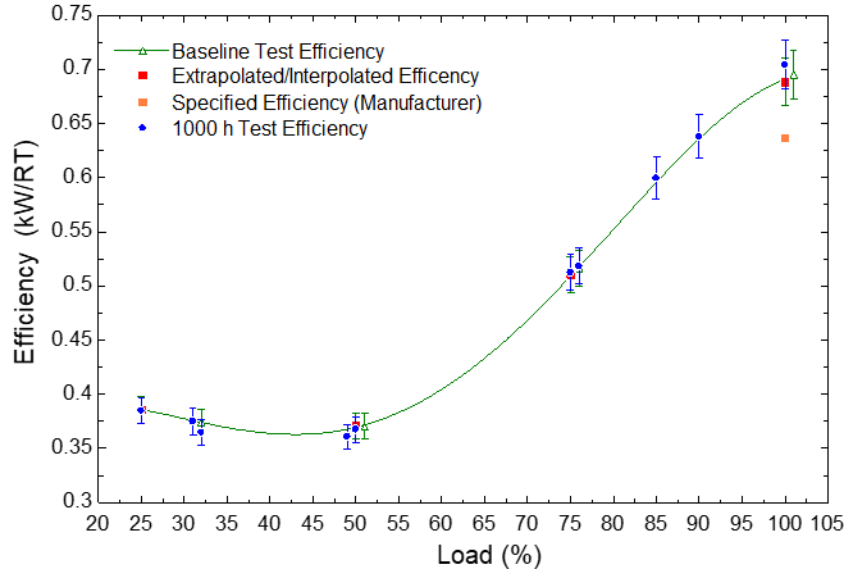


Figure 41: Overlay of 1000-test efficiencies over baseline

Table 25 shows the interpolated/extrapolated efficiencies. This step is necessary to allow a comparison of the test results with the characteristic line of the system. Building up on this, the IPLV value was calculated. Table 26 shows the values of the baseline test, the 1000 h-test and the manufacturer specification for comparison. The IPLV of the recurring performance test was about 0.3% more efficient than the one of the baseline tests while the 100% load efficiency value was 1.72% worse.

Table 25: Measured and interpolated/extrapolated efficiency values as basis for the IPLV calculation

<b>Load</b>	<b>Unit efficiency</b>
<i>%</i>	<i>kW/RT</i>
<b>25</b>	<b>0.3848</b>
31	0.3749
32	0.3646
49	0.3608
<b>50</b>	<b>0.3675</b>
<b>75</b>	<b>0.5125</b>
76	0.5183
85	0.5995
90	0.6379
<b>100</b>	<b>0.7042</b>

Table 26: Efficiency and IPLV value comparison

<b>EFFICIENCY COMPARISON</b>		
	<b>Full load efficiency</b>	<b>Part load efficiency (IPLV.IP)</b>
	<i>kW/RT</i>	<i>kW/RT</i>
Baseline rating	0.6882	0.4232
1000 h test	0.7042	0.4219
York specification	0.6363	0.4064

Summarizing there is to say, that the 1000 h-test did not show a measurable deviation that could directly be transferred to a performance degradation. The measured values are still close to the characteristic line that was formulated on the results of the baseline test. All existing differences in the results can be referred to different operating temperatures and mass flows during the test runs which were within the allowed tolerances. Considering that chillers are defined for several years of operation and thus for several thousand operating hours, this result was to be expected for the early performance test runs.

### 3.4 System and fault analysis

Assessing the performance degradation of the twin-screw chiller is one of the main objectives of the study. Therefore, it is important to analyze the experimental data related to the operation of the sub-systems such as compressor, variable speed drive, motor, and heat exchangers to get a better understanding of the control behavior under different load conditions. The compressor operating parameters are logged internally by the chiller. The analysis shows elaborated baselines from the initial test set and already includes a comparison with the data that was recorded in the 1000 h-test for some values.

#### 3.4.1 System and sub-systems

Following the example of Zhou et al. [19], the system was divided into sub-systems. This step makes the analysis of the system easier and allows an assignment of problems and performance loss to certain components or component groups.

To allow the study of the performance degradation of the whole chiller but especially of the compressor the chiller was grouped in 5 sub-systems which are the motor and electric drive of the compressor (1), the mechanical part of the twin-screw compressor (2), the condenser (3), the

economizer (4), and the evaporator (5). The numbering of the sub-systems is equivalent to the sub-system diagram in Figure 42. Since the focus of the investigation is on the compressor, two sub-systems were assigned to this component so allow an indication of losses on the mechanical and the electrical side. The three heat exchanger sub-systems (3, 4, and 5) are defined to enable the study of the performance loss of the compressor. The theory behind is that the overall performance loss of the chiller mainly comes from heat exchanger fouling and from a performance degradation on the compressor side. To quantify the degradation of the compressor, the fouling or at least the performance loss due to the heat exchanger conditions needs to be known. To calculate this heat exchanger-based performance degradation, all pressure levels need to be calculated separately.

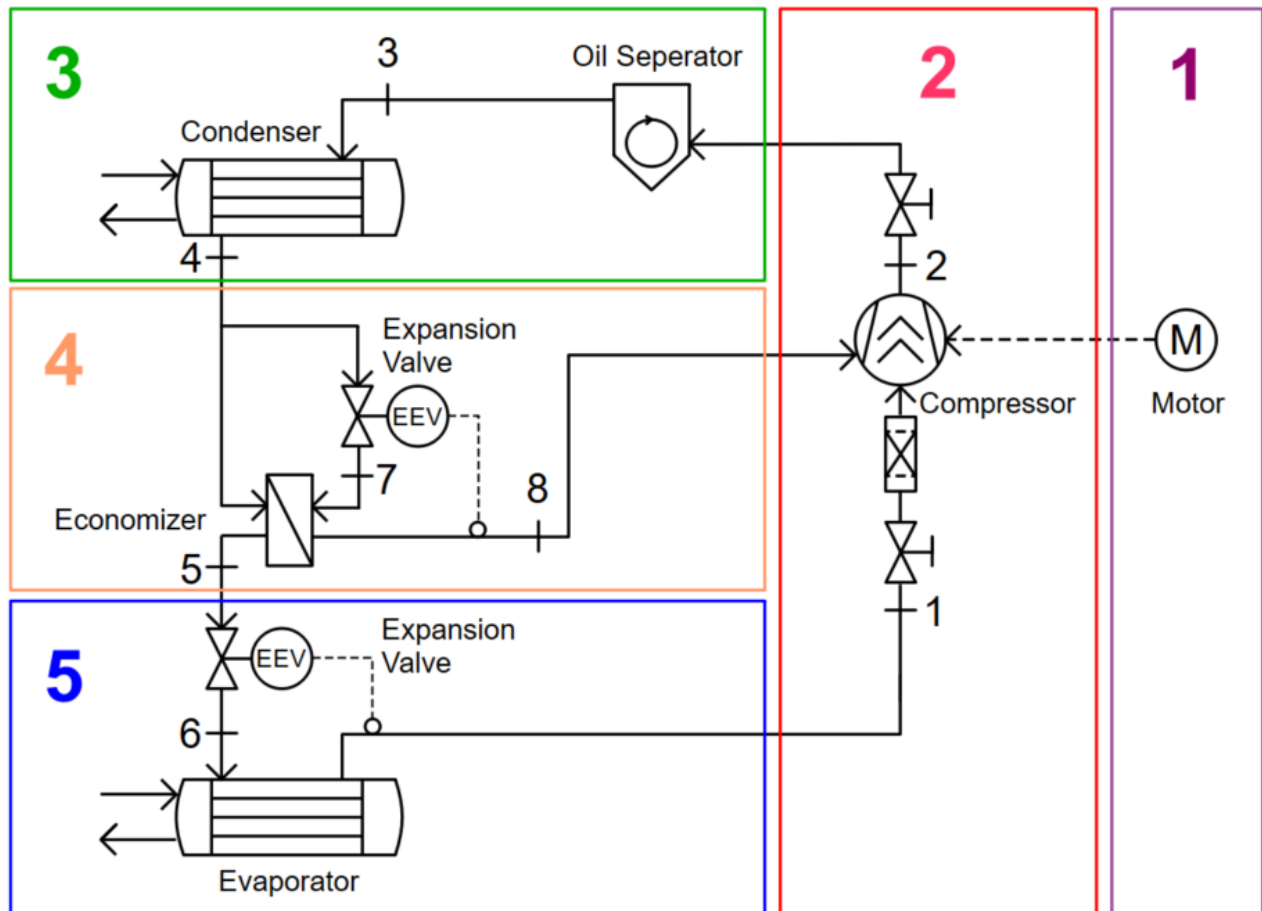


Figure 42: Sub-systems of the chiller [46]

### 3.4.2 Characteristic variables

Even if they use different names like characteristic values, sensitive values or sensitive variables, all approaches that were reviewed in published literature (paragraph 1.2) use measured or calculated values to identify faults and abnormalities of the system. For the analysis, values tracked by the chiller, and values tracked by the data acquisition system can be used. Also processed test values such as efficiencies can be used. Aim is to create the maximum value from these measurements. Adapted from Beghi et al. [20], the following 19 characteristic variables were selected, as listed in Figure 43. This list is not meant to be exhaustive. Should further analysis be necessary at a later point in time, the measurement data can be referred to at any time.

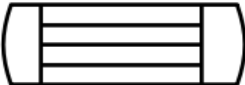
<p>Compressor</p> 	<ul style="list-style-type: none"> <li>Compressor Power Consumption</li> <li>System Pressure Levels</li> <li>Oil Pressure</li> <li>Oil Pressure Differential</li> <li>Isentropic Efficiency of the Compressor</li> <li>Refrigerant Suction Super Heat Temperature</li> <li>Refrigerant Economizer Super Heat Temperature</li> <li>Refrigerant Discharge Superheat Temperature</li> </ul>
<p>Motor</p> 	<ul style="list-style-type: none"> <li>Compressor Efficiency</li> <li>VSD Outlet Frequency</li> <li>VSD Outlet Voltage</li> <li>Compressor current draw</li> <li>Motor Temperature</li> </ul>
<p>Heat Exchangers</p> 	<ul style="list-style-type: none"> <li>Condenser Approach Temperature</li> <li>Evaporator Approach Temperature</li> <li>Evaporator LMTD</li> <li>Condenser LMTD</li> <li>Evaporator Refrigerant Mass Flow</li> <li>Condenser Refrigerant Mass Flow</li> </ul>

Figure 43: Characteristic variables for the fault analysis [46]

### 3.4.3 Compressor

The first variable in a compressor analysis that should be investigated when it comes to performance degradation is the power draw of the compressor for all test runs as plotted in Figure 44. An analysis of the power consumption can give first impressions of the efficiency changes. The diagram displays the power consumption versus the load spectrum of the chiller. The concave increasing graph is the trendline of the baseline test results and the solid red markers are all results from the recurring performance test at 1000 *hr*. It can be clearly seen that the performance values after 1000 hours of operation do not significantly deviate from the baseline.

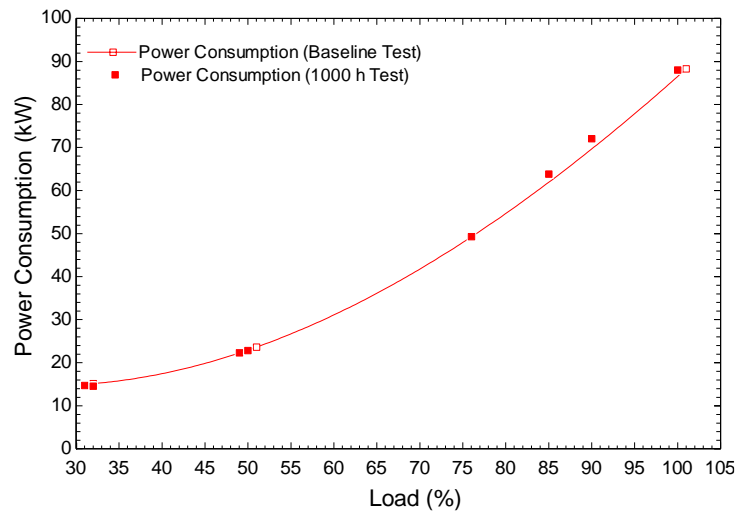


Figure 44: Compressor power consumption [48]

Another important check to estimate the condition of the compressor but also to whole chiller is the analysis of the system pressure levels. Figure 45 shows graphs of the three pressure levels – evaporation pressure, intermediate pressure, and discharge pressure. All three pressure levels have the results of the recurring performance tests (solid markers) plotted over the characteristic lines that were created based on the baseline test results. As mentioned in the literature review (section 1.2.1), the pressure levels are a good indicator to estimate the heat exchanger fouling or refrigerant charge on the one side, but together with the system temperatures they are also an ideal indicator potential compressor issues on the other side. A high discharge pressure could be sign for a clogged filter/dryer unit for example as it is described in the manual [37].

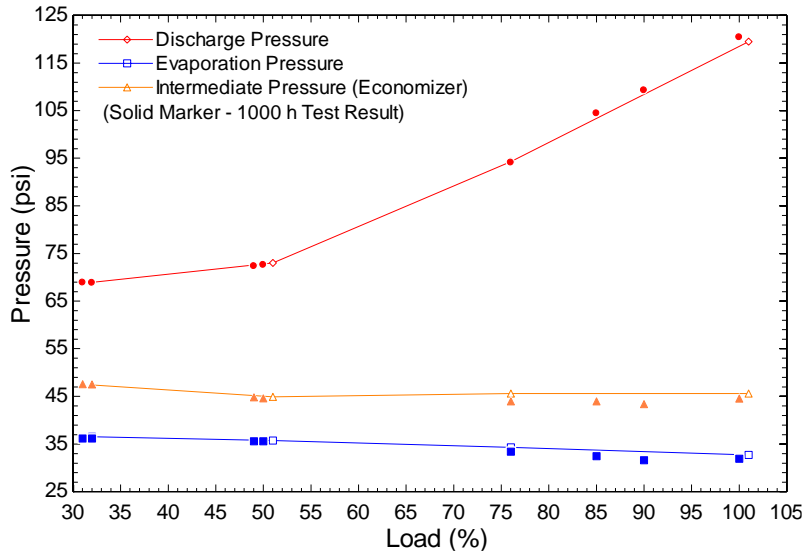


Figure 45: Pressure levels in the systems [48]

The correct operation of an oil-injected twin-screw compressor relies on the lubrication system. The oil injection system consists of pressurized lines that distribute the oil in several locations of the twin-screw compressor housing to provide lubrication to bearings and to seal contact lines between the screw rotors. As previously described in Figure 7, a centrifugal oil separator is installed in the pressure line, right after the compressor to separate the largest fraction from the oil that is mixed with the high-pressure refrigerant. The fraction of the oil that reaches the heat exchangers is pumped back from the sumps of the heat exchanger shells with the help of an electric auxiliary pump. The lubrication system does not have a mechanical pump, but it is driven by the differential pressure. As graphed in Figure 46, the system oil pressure and the oil differential pressure present a similar behavior under different load conditions. The trendlines refer to the baseline test values, while the filled dots represent the values from the 1000-hour test. In particular, the oil line differential pressure increases at higher loads which enable more flow through. However, at lower loads, the low pressure differential could yield to insufficient lubrication. Hence, it can be leveraged to implement an accelerated life cycle testing, this effect can be used. The measured values show no clear deviation after the first thousand test hours yet. Different stages of oil distribution can also be seen on the sight glasses of the oil separator (see Figure 47). While the lower glass is barely covered with oil in the left example during an operation with low pressure differential, the oil level is usually visible in the upper glass during an operation with high pressure differential as the right example shows. This can be referred to a lower oil distribution due to a worse lubrication.

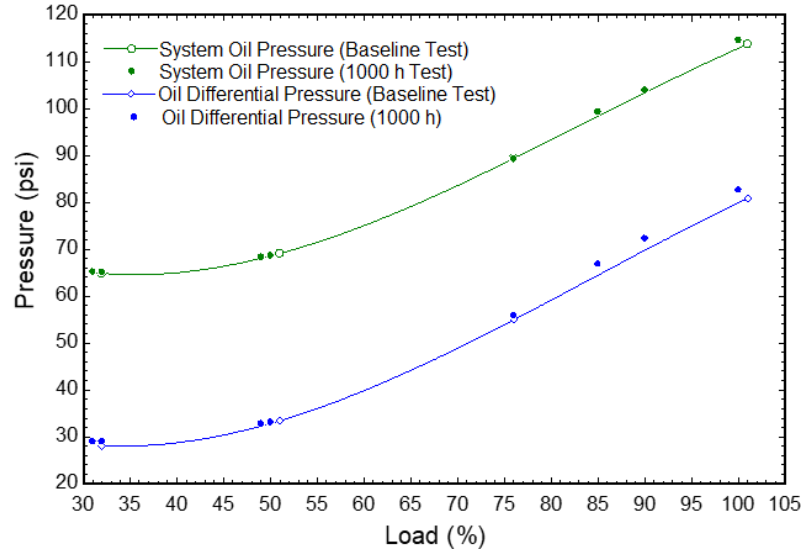


Figure 46: System oil pressure and oil differential pressure [48]

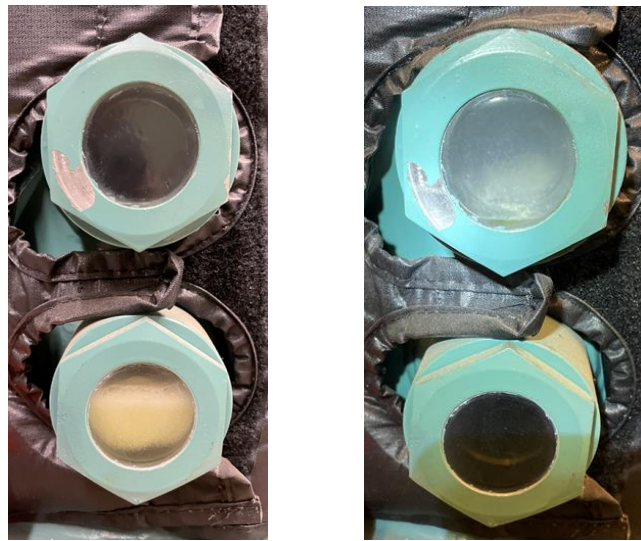


Figure 47: Sight glasses of the oil separator during an operation with low (left) and high (right) pressure differential

The literature review showed that the isentropic efficiency of the compressor is a very relevant variable to judge the condition of a compressor. As the ratio of the actual drawn power over the theoretical, isentropic power draw it represents the second law effectiveness of the compressor.

Since the investigated compressor is a screw compressor with economizer port, it is not sufficient to just investigate the inlet and the outlet conditions of the compressor. It is also

important to consider the mass flow and the temperature decrease that is caused by the economizer or through the economizer port. These considerations were taken into account by the isentropic efficiency formula (3.13) presented by Lambers [45]. The calculation in the numerator of the equation represent to the isenthalpic process where the values with the indexes  $s$  refer to the suction side,  $a$  to the admission or economizer port and  $d$  to the discharge port. Lambers calculates the actual work in this paper to. Since the electrical power consumptions are given from the measurements, they can be used directly. That makes the calculation even more precise since all losses of the compressor are included here.

$$\eta_{\text{ISO}} = \frac{\dot{m}_s \cdot (h(s_s; p_d) - h(s_s; p_s)) + \dot{m}_a \cdot (h(s_a; p_d) - h(s_a; p_d))}{P_{\text{el}}} \quad (3.13)$$

In Figure 48, the calculated isentropic efficiencies are plotted versus the load range of the compressor. The trendline was drawn through the baseline test results, while the solid dots show the results of the 1000 h-test. An interesting trend that was measured here, is that the efficiencies of after 1000 *hr* are roughly 2.5% higher than the same variables of the baseline test. A reason for that could be that the machine parts had to run in first. In this case the isentropic efficiency should stay constant for a bit before it starts to decrease again. Further measurements are needed to proof this theory.

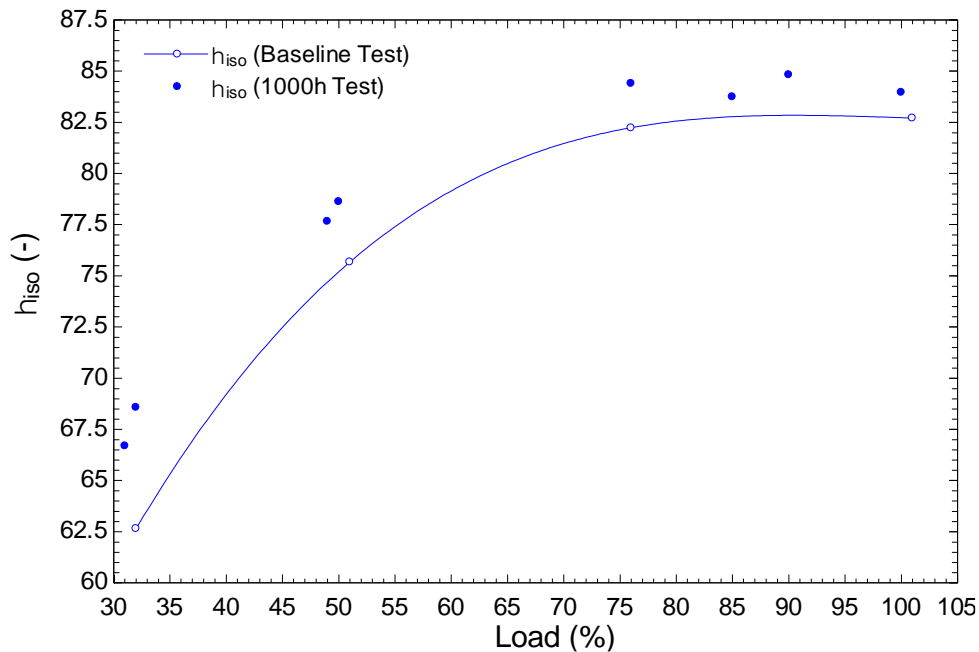


Figure 48: Isentropic efficiency of the compressor

The last measurements that are focused are the superheat temperatures. The superheats are of the chiller are measured for the evaporator or suction superheat (Figure 49), the economizer superheat (Figure 50), and the discharge superheat (Figure 51). The first impression shows already that the superheat temperatures all follow very different trends.

The suction superheat can be an indicator for several system issues. It can indicate refrigerant loss, heat exchanger fouling but also compressor damage since the compressor controls the suction pressure in interaction with the expansion valve. Since the expansion valve can compensate a lot of issues on the evaporator side, the problems are usually severe at the point on which they can be indicated. Figure 49 shows the superheat in Kelvin over the load range of the chiller. The trendline was drawn over the baseline test values. The solid dots are the results of the first recurring performance test. All super heat values of the most recent test are about 1.5 K larger than the baseline. In lower load ranges, the deviation is more significant than in higher load ranges. It is not possible to already correlate a problem to that trend. Since it is a pretty constant deviation, heat exchanger fouling could be the cause what should be considered in further testing and analysis.

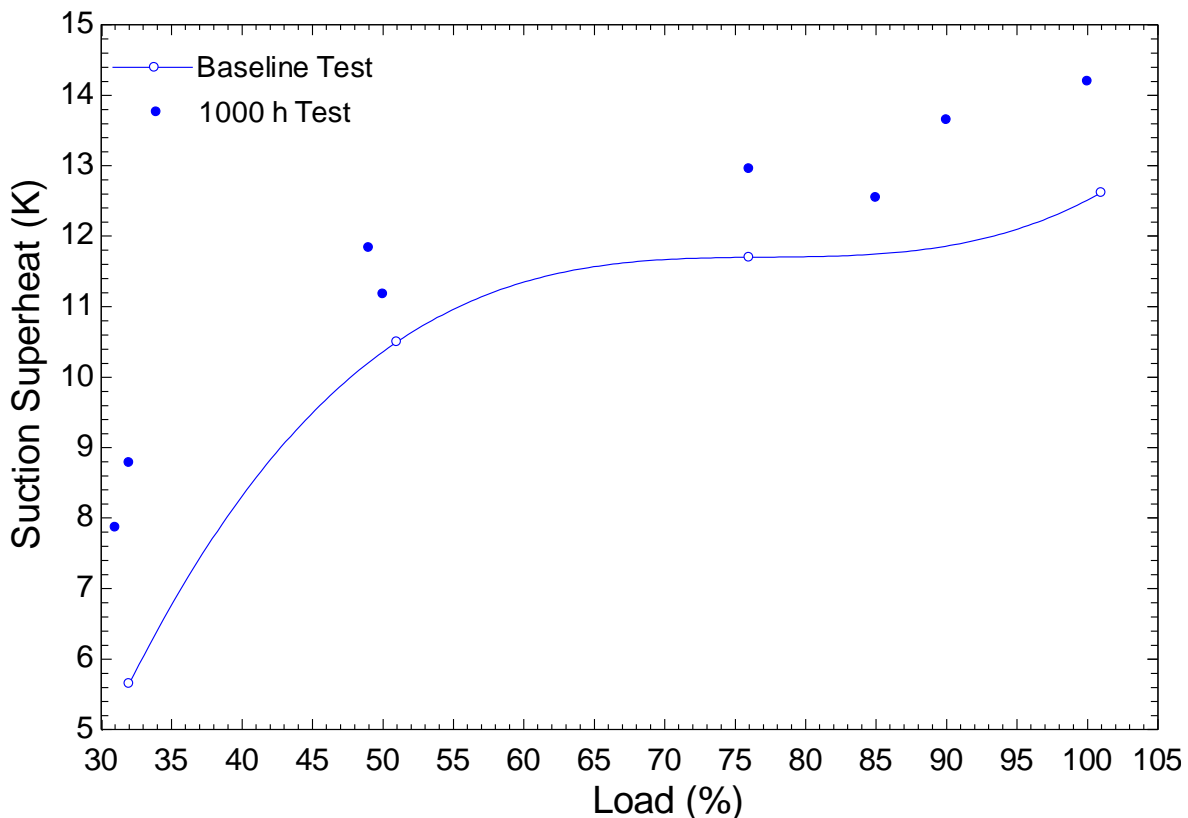


Figure 49: Superheat measured in the suction line

The economizer superheat Figure 50 is almost constant. Even if it looks very fluctuating, the values appear all within a span of 1 K. Notable is that the superheat at the recurring baseline tests (solid dots) in a lot of cases appear to be on exactly the contrary spectrum of the trendline of the baseline tests.

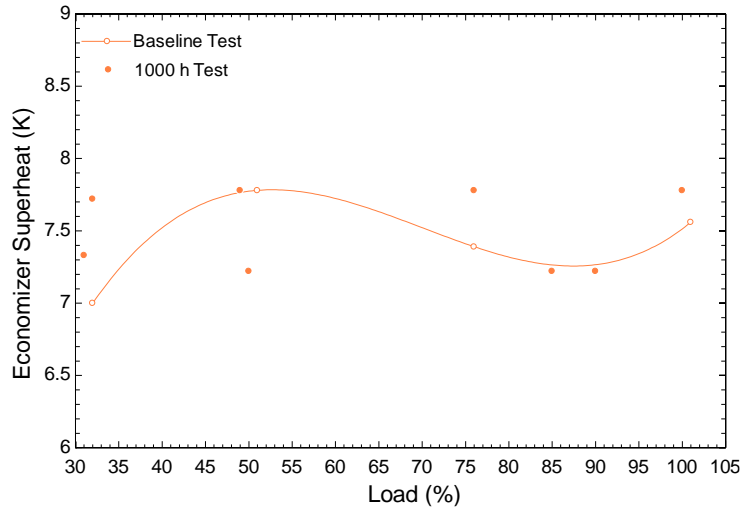


Figure 50: Super heat measured on the economizer port

Figure 51 shows the discharge superheat. It is good to see that the values of the 1000 h-test, which are plotted with solid points, follow the trend line of the baseline tests. Even if there is also a deviation, it is smaller than on the suction side. The discharge superheat as well as the discharge temperature can be indicators for mechanical wear on the compressor or clogged suction filters. The measured values are still in a normal range.

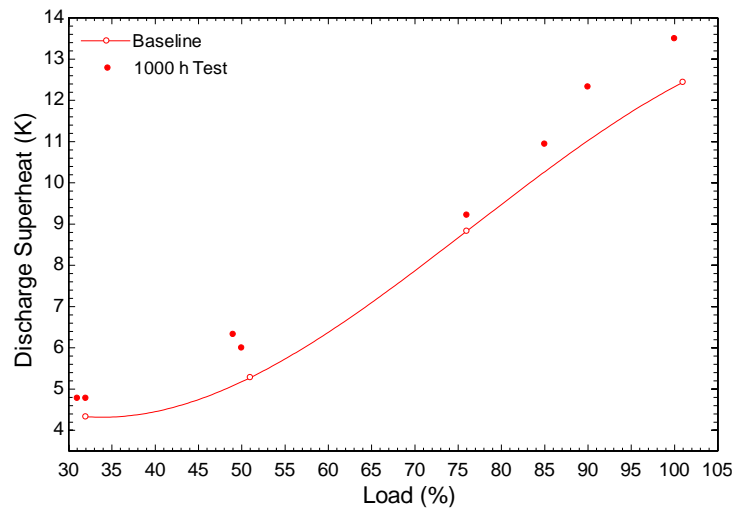


Figure 51: Superheat in discharge line

### 3.4.4 Electric drive system (Motor and VSD)

An important role in the aging and efficiency of a chiller plays the electric drive which consists of the motor and the variable speed drive that controls the motor speed. Figure 52 shows that the output frequency in green and the voltage output of the variable speed drive (VSD) in blue. The graphs are trendlines based on the initial test data while the solid markers are the values from the 1000 h-test. The output frequency raises almost linear over the load range while the output voltage follows the exact same trend. The values of the recurring performance tests are extremely close to the initial test vales in the lower load range (smaller than 85%) and deviate slightly above 85% load.

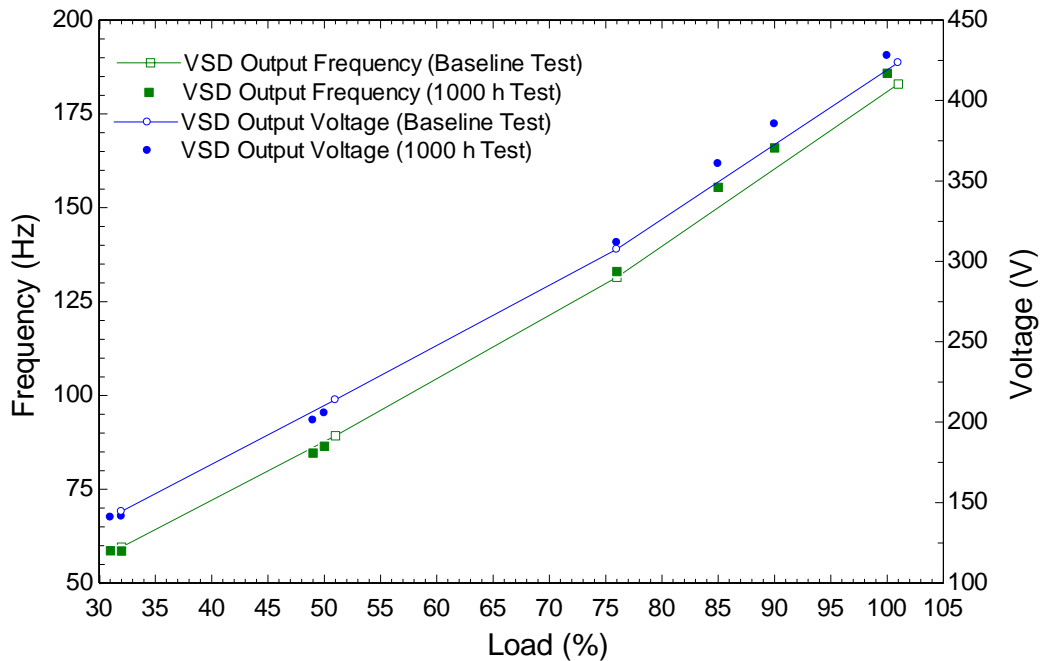


Figure 52: VSD output frequency vs. VSD output voltage [48]

Figure 56 is a diagram that shows the motor phase currents of the electric motor over the load spectrum of the chiller. The trendlines refer to the baseline test results while the solid markers are the 1000 h-test results. Generally, there is to be noted that the current through Phase A is indicated about 5 A higher than the other phases at all loading conditions. The current adjusts based on the increased shaft load of the motor accordingly. Since the current sensor is integrated within the chiller controls, a calibration or functional check might not be possible, but the abnormality should stay under investigation for the following tests.

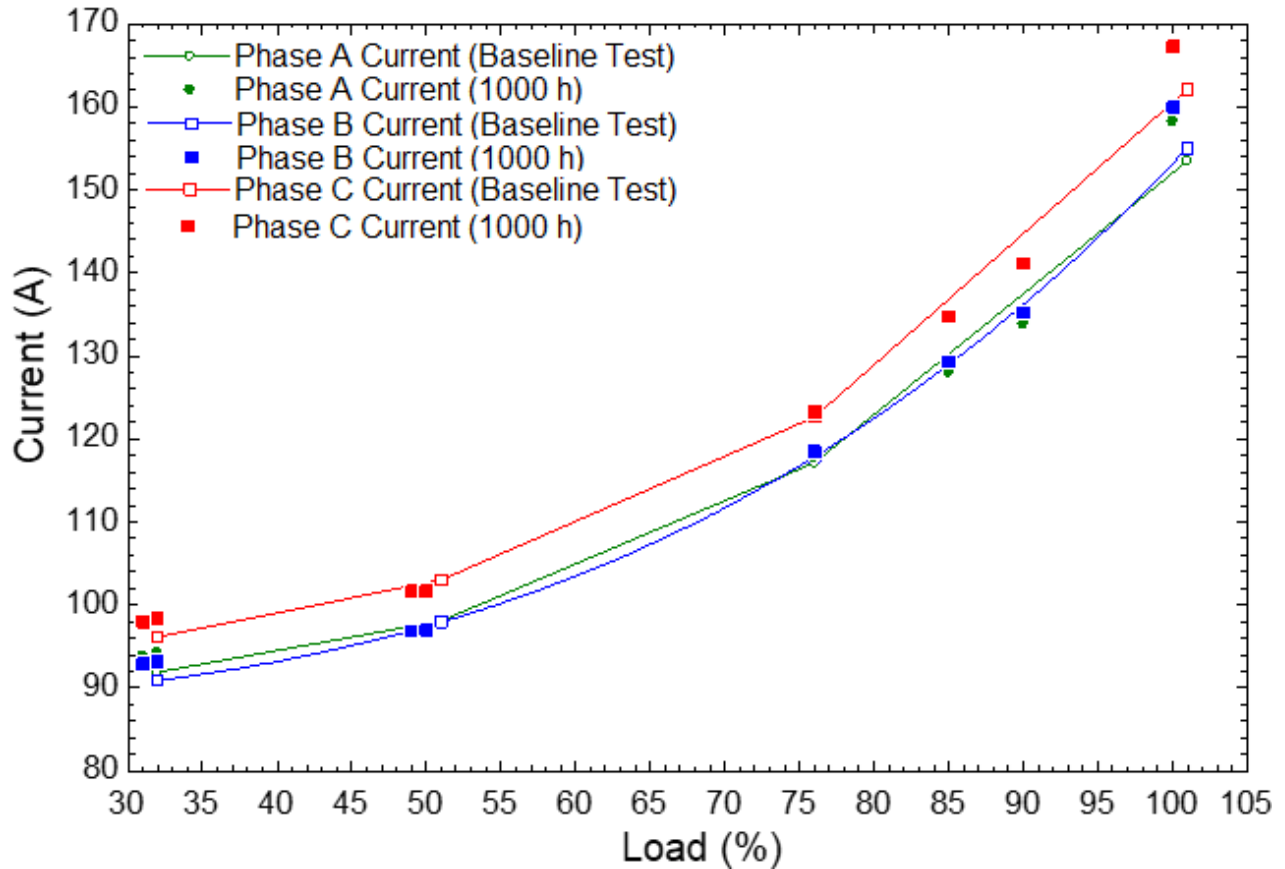


Figure 53: Compressor phase current comparison [48]

In the next diagram (Figure 54), the motor temperatures during the test runs are plotted over the load spectrum of the chiller. The trendline is drawn through the baseline test results while the solid markers are the plotted results of the recurring performance test. The motor has three temperature sensors. The position of the sensors is not defined but probably they are equally distributed over the motor since they are also used to activate the compressor heater which is necessary to avoid the condensation of refrigerant in the compressor at low temperatures.

The temperatures show a notable trend. For loads of less than 50%, the temperature measured by sensor 1 is almost in the center of the Sensor 2 and Sensor 3 values. Above 50% load the Sensor 1 value increases drastically and is higher than the Sensor 2 value. Therefore, Sensor 1 has followed not the trend of Sensor 2 and Sensor 3 which have almost the identical slope over the load course. It is to mention that the values of the 1000 h-test fit into the trendline without bigger deviations.

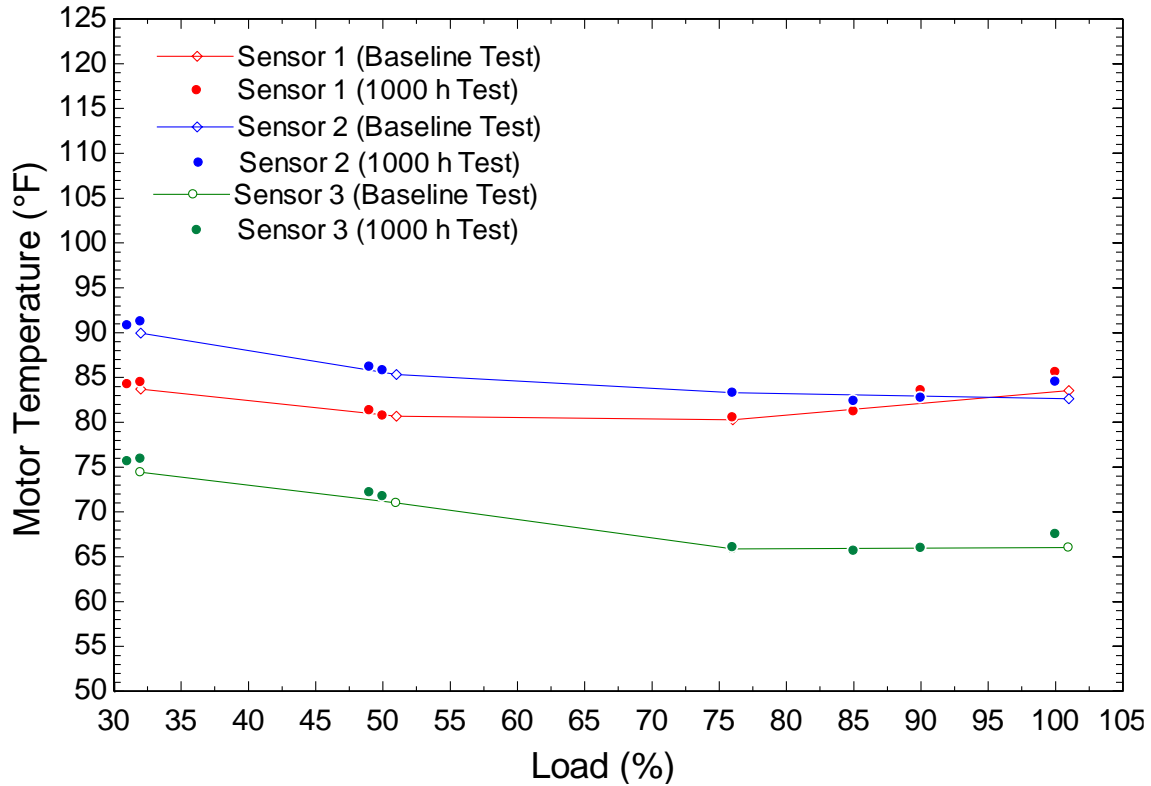


Figure 54: Motor temperatures [48]

### 3.4.5 Heat exchanger

Heat exchangers are sensitive sub-systems when it comes to the analysis of performance degradation of a chiller. Depending on what kind of heat exchangers and heat transfer fluids are used, their performance may highly be affected by fouling. The investigated chiller has two shell and tube heat exchangers with steel shell and copper tubing. The used heat transfer fluid is regular water. At the beginning, untreated water was used in both, the evaporator, and the condenser cycle. Due to concerns regarding the water quality and a potential heat exchanger fouling, chemical water treatment was started later. Check 2.2.6 for further details about the water quality and treatment. Since a mechanistic heat exchanger fouling model 3.1.4 could not achieve the necessary accuracy to give feedback about the surface condition, it was decided to create a baseline of the fluid temperatures and LMTDs at the test runs. This baseline helps to identify changes in the temperature behavior of the system early on, which is a clear indicator for fouling.

Figure 55 shows the refrigerant and water temperatures in both heat exchangers. The trendline was created from baseline test data and the solid points are results from the recurring performance testing.

The diagram is basically identical to Figure 24 but supplemented by the fluid temperatures of the 1000 h-tests. The most recent temperature values are very close to the baseline test which is a sign that the fouling process in the heat exchangers did not progress significantly since the start of the baseline tests. The fouling value at the beginning of the baseline tests cannot be retrieved from that graph.

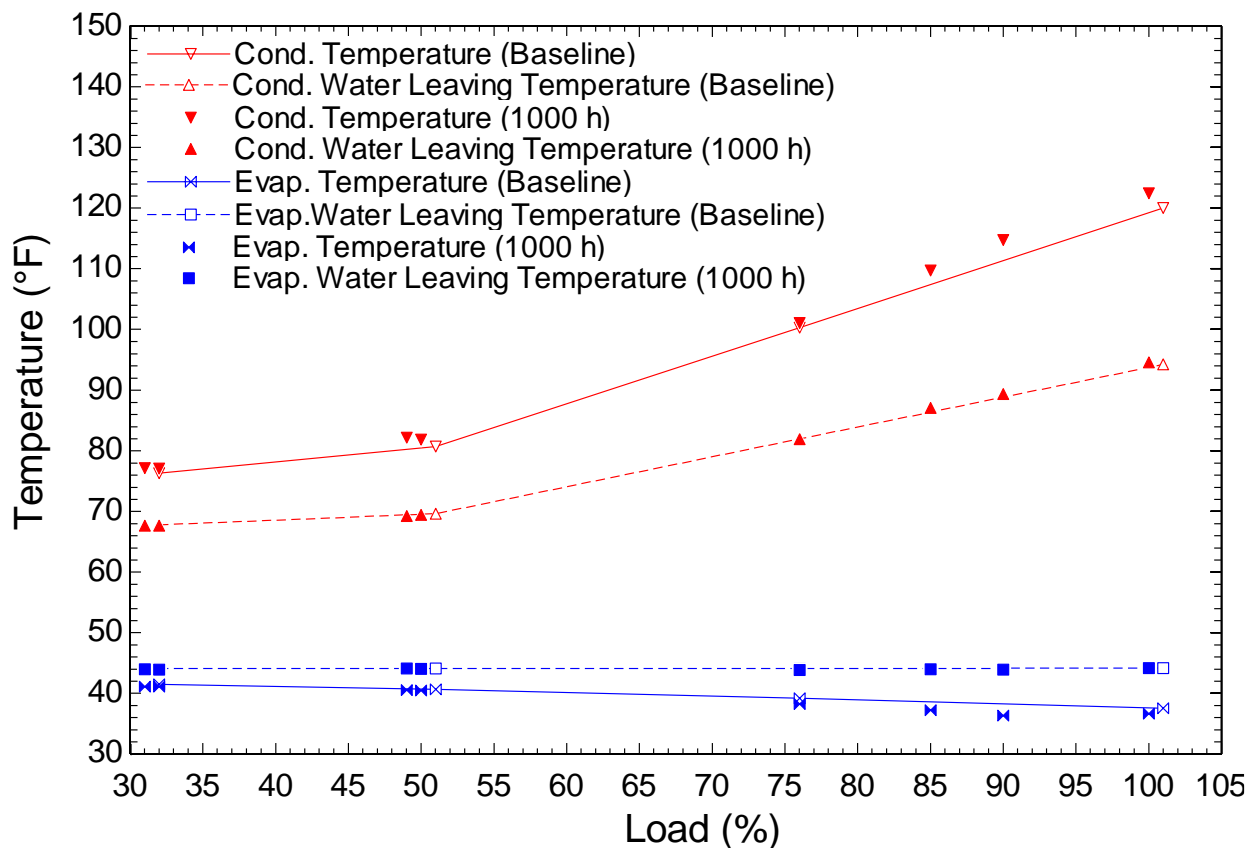


Figure 55: System fluid temperatures [48]

Additionally, the data from Figure 25 was supplemented by the 1000 h-test results from in Figure 56. An interesting finding is, that the temperature differences in the low load ranges (lower than 50%) are close to the trend line while the values deviate stronger at higher load ranges (above 50%) with a peak deviation at 90%. According to the manual [37], the change of the LMTD in

relation to the LMTD for clean tubes is the main indicator for heat exchanger fouling. The manual further states that the user should clean the heat exchanger tubes chemical or mechanical once the LMTD deviates more than 2 K from the base line. The maximum deviation at 90% load is 1.7 K, which is close to this value. For that reason, the temperature deviation should be investigated closely in further performance tests and a heat exchanger cleaning should be executed if the LMTD further rises.

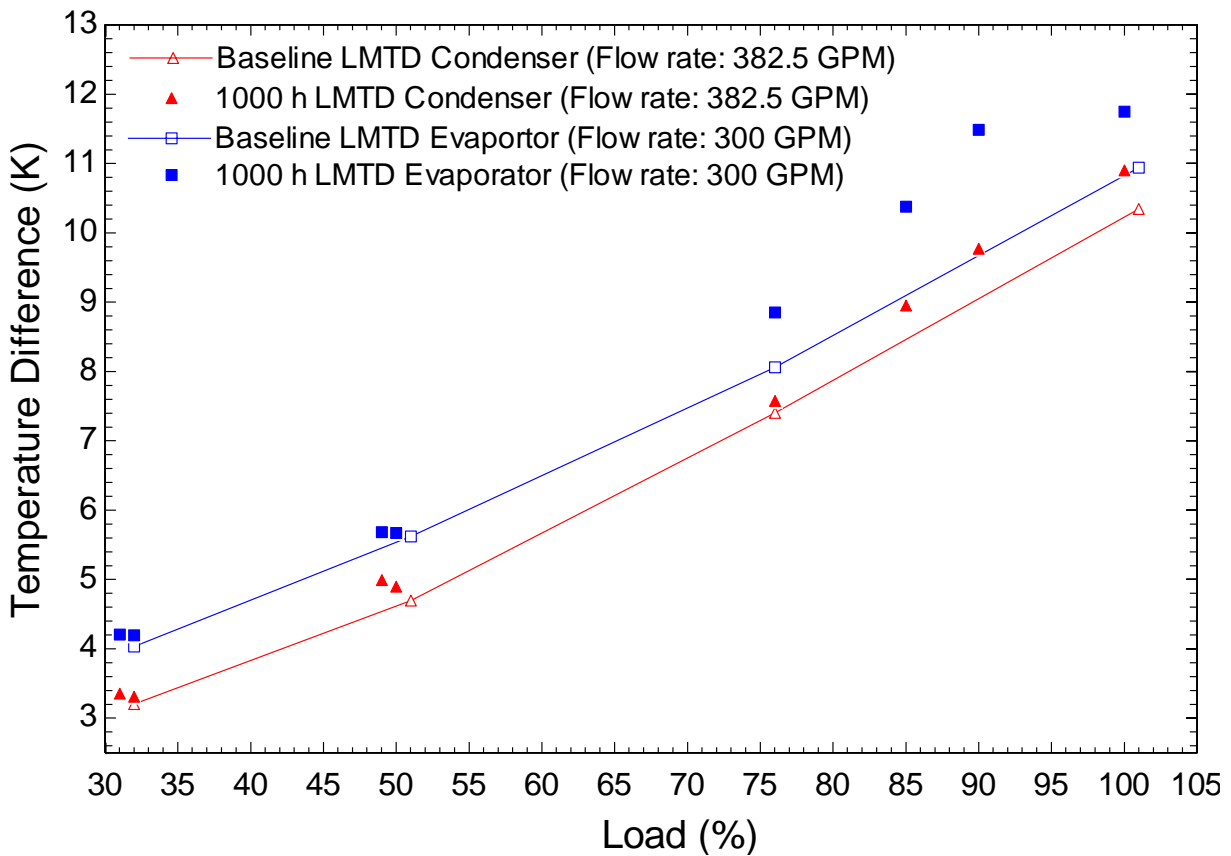


Figure 56: LMTD of the Condenser and the evaporator [48]

In conclusion, there is to say that the analysis set a solid benchmark for further performance and deviation tests. All sub-systems were analyzed extensively and properly. After 1000 hours of the ALT, no clear performance degradation could be measured yet. The temperature might show a beginning heat exchanger fouling and therefore should be investigated with increased attention.

Figure 57 and Figure 58 show the mass flows of the refrigerant in the evaporator and the condenser as well as the capacity of each heat exchanger as a comparison over the whole load range of the chiller. The trendlines were defined in the baseline test and the solid dots are the plotted results of the 1000 h-test. The mass flow in both chillers increases almost linear with the capacity raise. No abnormality can yet be determined yet in either heat exchanger on the basis of these values.

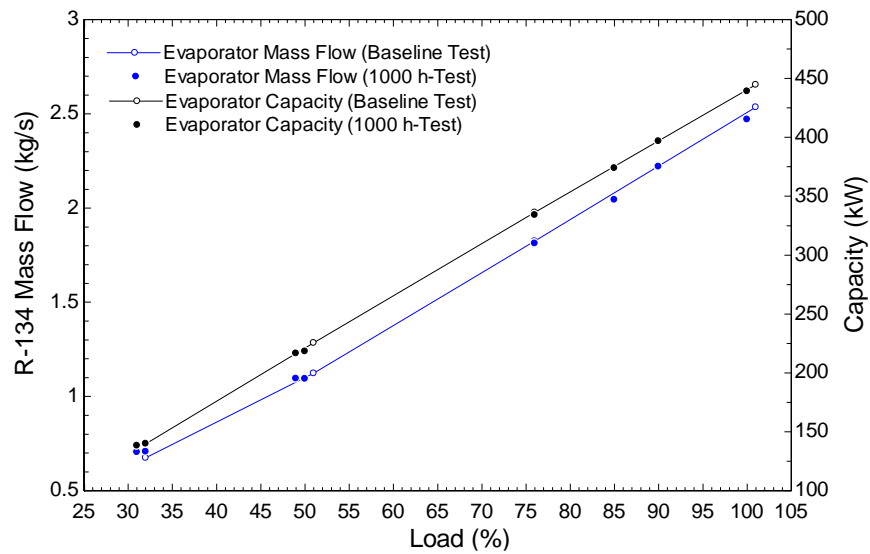


Figure 57: Evaporator mass flow and capacity [48]

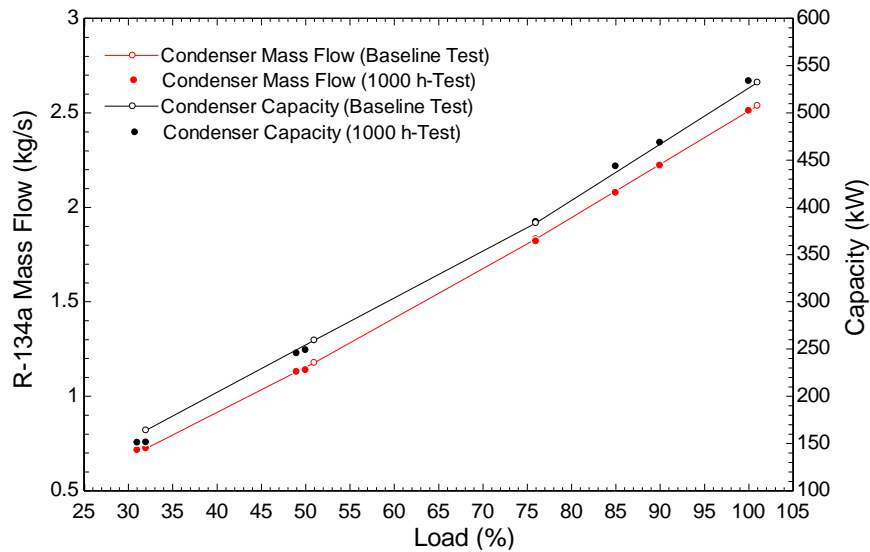


Figure 58: Condenser mass flow and capacity [48]

## 4. PRELIMINARY SYSTEM MODEL

### 4.1 Objectives

The experimental work described in the previous chapter serves the purpose to create a comprehensive screw chiller data set in long-term operation. Aim of the project is to create a system model, that can calculate the performance degradation of a twin-screw chiller with respect to the time. Such a model could be used in several applications such as life-cycle analyses or in an FDD tool to allow cost and time-effective maintenance. These applications become more and more relevant in times where energy-efficiency and carbon dioxide emissions play a bigger role.

### 4.2 Approach

The performance degradation model will be created in 4 steps:

1. Set up model
2. Validate model against steady-state data
3. Model of a more detailed compressor structure
4. Performance degradation over time

The first step was to set up a transient model that is running without any issues or errors. Therefore, the system was simplified as far as possible without compromising accuracy or neglecting important components. Figure 59 shows the PI diagram of this initial model set up. For this, the compressor which is a screw compressor with economization was replaced by two similar compressors. The refrigerant mass is represented by a module called “filling station” in Dymola [49]. The only system control that was integrated at this step was the control of the evaporator water outlet temperature which is the main task of the chiller. Once all components were selected, the modules which all represent mechanistic thermodynamic models of components, were adjusted so that the components use the actual geometrical and thermodynamical data of the chiller components as far as they were available from manuals [37] and specifications [41; 42; 43]. Until this point the system could already be set up. The further points give an overview of the next modeling steps.

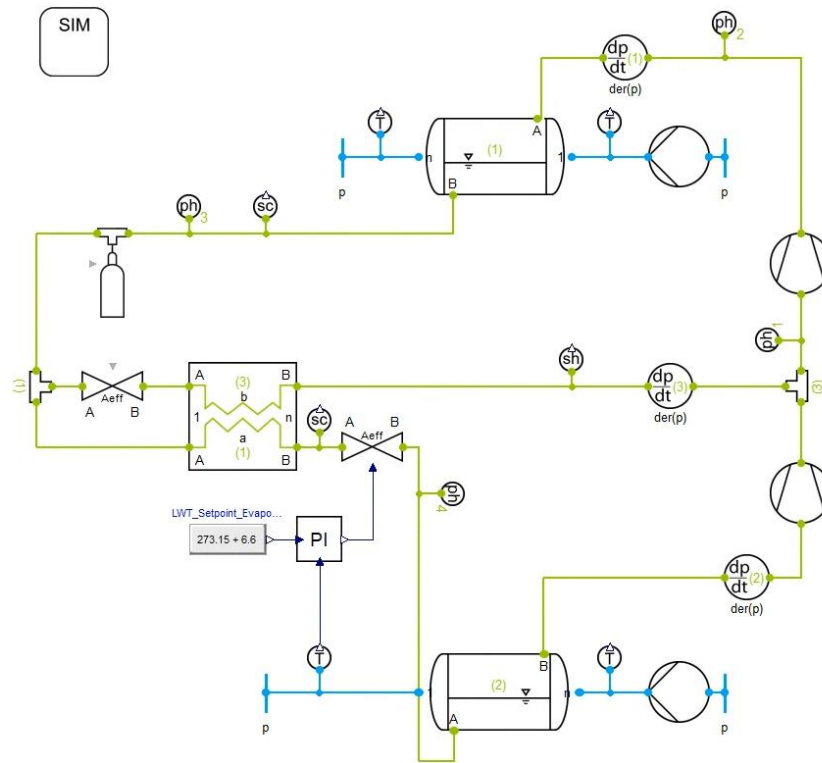


Figure 59: Dymola modeling set up [49]

In the next step, the model must be validated against steady state data. That means the thermodynamic data of all 4 baseline tests will be taken to run the model. The results, such as efficiency, will be compared to the actual efficiency measured in the test runs. In case there are deviations, the component properties will be adjusted accordingly so that the model properties are as close as possible to the actual system properties. Once the system is validated over the whole load range in a sufficient accuracy, step three can be taken. In this step, a compressor model must be created. Since the initial model consist out of two separate compressors, it cannot sufficiently provide the same characteristics as a screw compressor with economization. Due to this issue, a compressor structure must be created in Modelica [51] to provide a realistic compressor behavior for the system. The Modelica [51] code can then be used in Dymola. This change again must be validated before finally, the performance degradation over time can be implemented in the model. To create an algorithm that is sensitive to the performance degradation over time, the dataset is especially important. It should cover life span that is long enough to display an actual performance degradation on the investigated chiller, so that the model provides a sufficient accuracy.

## 5. CONCLUSION

The design and commissioning of the test stand provided some difficulties that were overcome by the application of thermodynamic models and an upgrade of main components the heat dissipation heat exchanger and the two pumps. The usability and controllability of the test system could clearly be increased in all load ranges. The new heat exchanger allows a reliable dissipation of heat from the system and the new pumps in both loops ensure a standard conform measurement which was not possible before.

In the baseline testing, 4 valid test runs were conducted. Three of them were not more than 2% off the target capacity. That allowed an easy and exact calculation of the unit efficiency at full load and the IPLV.IP value. While the IPLV.IP value is close to the specified value with a deviation of -4.13 %, the full load unit efficiency still has a clear deviation of -8.16 % to the specified value. Still, the efficiency values help to generate a characteristic curve of the system that is going to be used as the baseline for the beginning performance degradation tests. The chiller data that was collected during the test runs, was used for a detailed analysis of the variable speed drive and the compressor which is necessary to gain a better understanding for the factors that lead to a performance degradation during a long-term operation.

The accelerated life cycle tests are in operation since almost 5 months (April 2022) in alternating test intervals of two weeks. The first recurring baseline test was conducted in February after 1000 h of operation. A degradation of the performance could not be identified yet. A model of the cycle was set up to implement the experimental data

In terms of future work, the two main tasks for the future of this project are to improve and finish the model as well as run further tests. The transient model that was set up should focus on the impact of performance degradation. With the continuation of the test runs, more data will be available for a validation. The findings can be used to establish an algorithm for the performance degradation and FDD of the screw chiller. Possible field test will help to enable a wider application of the model for more than just the investigated chiller. Furthermore, the accelerated life testing is going to be continued with the current test modes. Recurring baseline tests will help to investigate the performance degradation of the chiller. The application of additional test modes is another possibility. By using a water-glycol mixture as working fluid, the ice making mode of the chiller with an operation at lower temperatures could be an option.

## APPENDIX I: P, h DIAGRAM OF THE BASELINE TEST CYCLES

*32% Part Load (Date: 08/03/2021)*

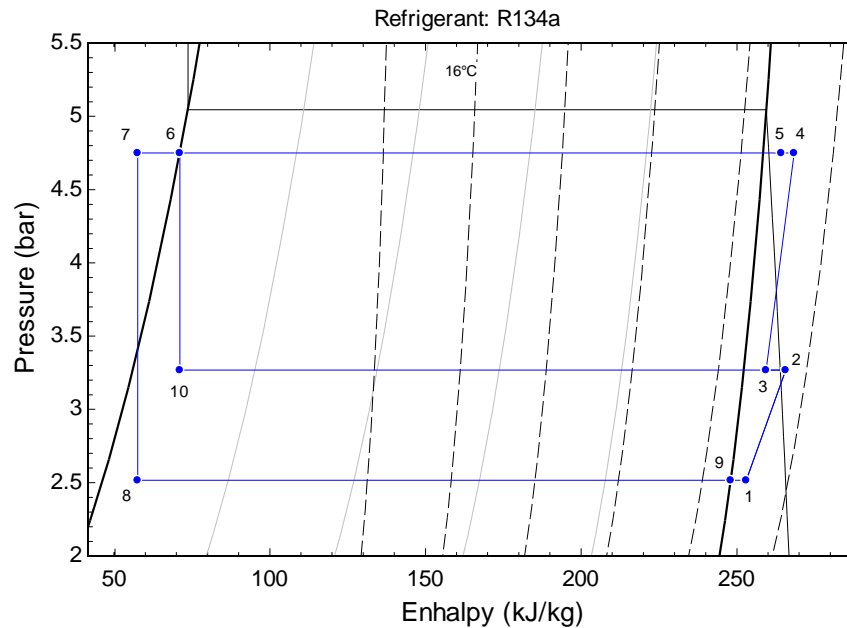


Figure 60: P, h diagram of the cycle at 32% load during the baseline test [48]

Table 27: Thermodynamic properties in cycle during 32% load baseline test run [48]

State	<b>p</b>	<b>T</b>	<b>u</b>	<b>h</b>	<b>s</b>	<b>x</b>	<b>ρ</b>	<b>v</b>
Point	<i>bar</i>	<i>K</i>	<i>kg/kJ</i>	<i>kg/kJ</i>	<i>kg/kJ·K</i>	-	<i>kg/m<sup>3</sup></i>	<i>m<sup>3</sup>/kg</i>
<b>1</b>	2.52	274.7	232.20	253.00	0.952	100	12.13	0.0825
<b>2</b>	3.27	291.1	243.70	265.70	0.952	100	14.91	0.0671
<b>3</b>	3.27	284.1	238.20	259.40	0.9553	100	15.42	0.0649
<b>4</b>	4.75	297.7	246.70	268.40	0.9587	100	21.87	0.0457
<b>5</b>	4.75	293.4	243.00	264.30	0.9448	100	22.36	0.0447
<b>6</b>	4.75	287.3	70.74	71.12	0.2726	0	1247.00	0.0008
<b>7</b>	4.75	277.3	57.18	57.55	0.2246	0	1281.00	0.0008
<b>8</b>	2.52	269.0	56.24	57.55	0.2258	0	193.10	0.0052
<b>9</b>	2.52	269.0	227.90	248.00	0.9338	1	12.47	0.0802
<b>10</b>	3.27	276.2	69.31	71.12	0.2741	1	180.90	0.0055

51% Part Load (Date: 08/03/2021)

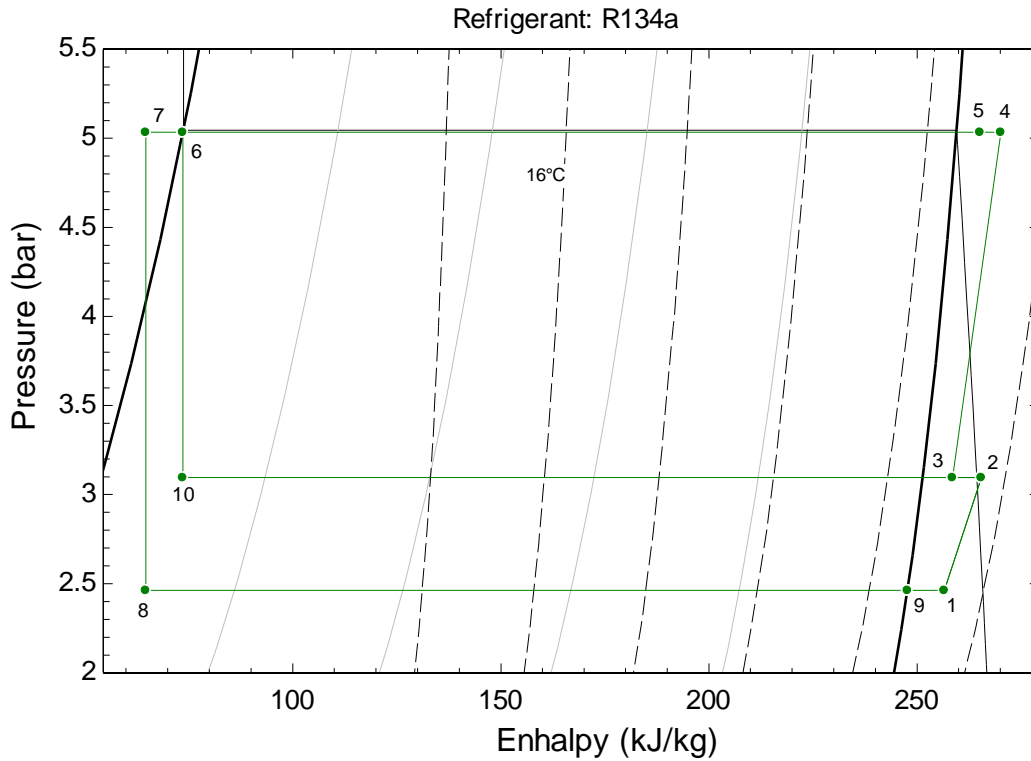


Figure 61: P, h diagram of the cycle at 51% load during baseline test [48]

Table 28: Thermodynamic properties in cycle during 51% load baseline test run [48]

State	p	T	u	h	s	x	$\rho$	v
Point	bar	K	kg/kJ	kg/kJ	kg/kJ·K	-	kg/m <sup>3</sup>	m <sup>3</sup> /kg
1	2.46	278.6	235.30	256.50	0.9665	100	11.62	0.0860
2	3.10	290.4	243.50	265.50	0.9665	100	14.10	0.0709
3	3.10	282.7	237.30	258.50	0.9563	100	14.63	0.0684
4	5.03	300.2	248.30	270.10	0.9603	100	23.06	0.0434
5	5.03	294.9	243.80	265.10	0.9433	100	23.70	0.0422
6	5.03	289.1	73.21	73.62	0.2812	0	1240.00	0.0008
7	5.03	282.6	64.38	64.71	0.2503	0	1256.00	0.0008
8	2.46	268.4	62.63	64.71	0.2526	0	118.30	0.0085
9	2.46	268.4	227.50	247.70	0.9342	1	12.21	0.0819
10	3.10	274.7	71.37	73.62	0.2836	1	137.90	0.0073

76% Part Load (Date: 08/03/2021)

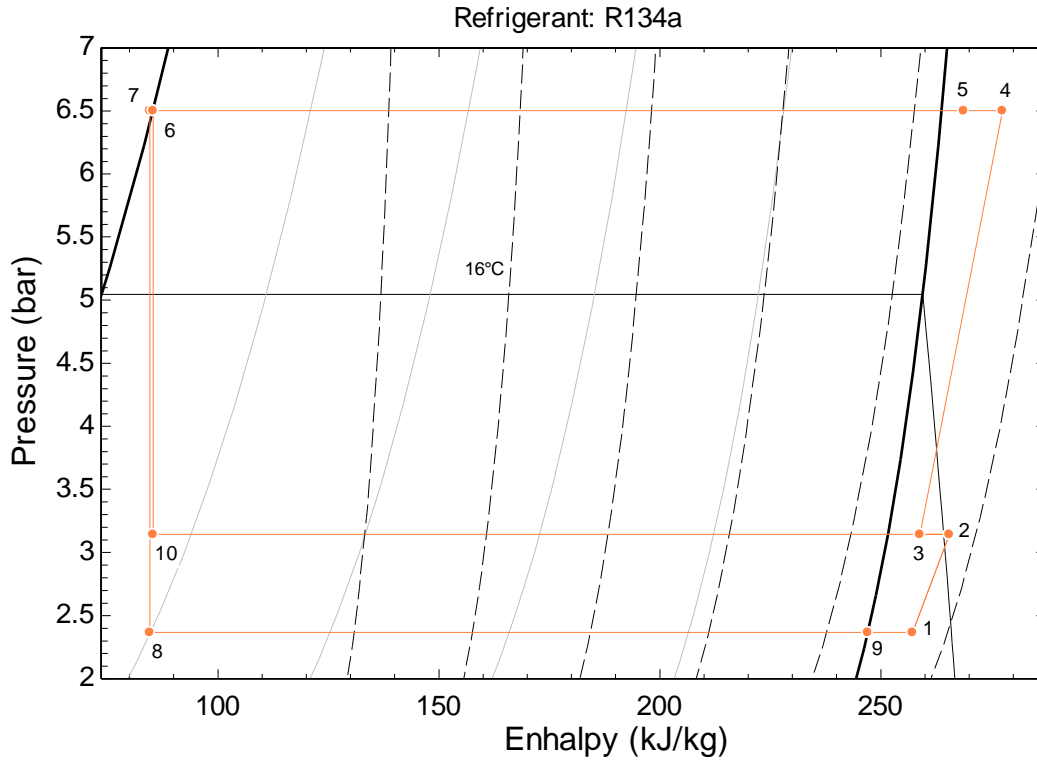


Figure 62: P, h diagram of the cycle at 76% load during baseline test [48]

Table 29: Thermodynamic properties in cycle during 76% load baseline test run [48]

State	p	T	u	h	s	x	$\rho$	v
Point	bar	K	kg/kJ	kg/kJ	kg/kJ·K	-	kg/m <sup>3</sup>	m <sup>3</sup> /kg
1	2.37	279.1	235.90	257.20	0.9720	100	11.11	0.0900
2	3.14	290.6	243.60	265.50	0.9720	100	14.33	0.0698
3	3.14	283.2	237.70	258.90	0.9564	100	14.84	0.0674
4	6.50	311.1	255.30	277.60	0.9661	100	29.26	0.0342
5	6.50	302.3	247.60	268.80	0.9374	100	30.70	0.0326
6	6.50	297.4	84.73	85.27	0.3206	0	1210.00	0.0008
7	6.50	296.8	84.00	84.53	0.3181	0	1212.00	0.0008
8	2.37	267.4	80.38	84.53	0.3271	0	56.99	0.0176
9	2.37	267.4	226.90	247.00	0.9348	1	11.75	0.0851
10	3.14	275.1	81.89	85.27	0.3258	1	92.96	0.0108

100% Full Load (Date: 08/03/2021)

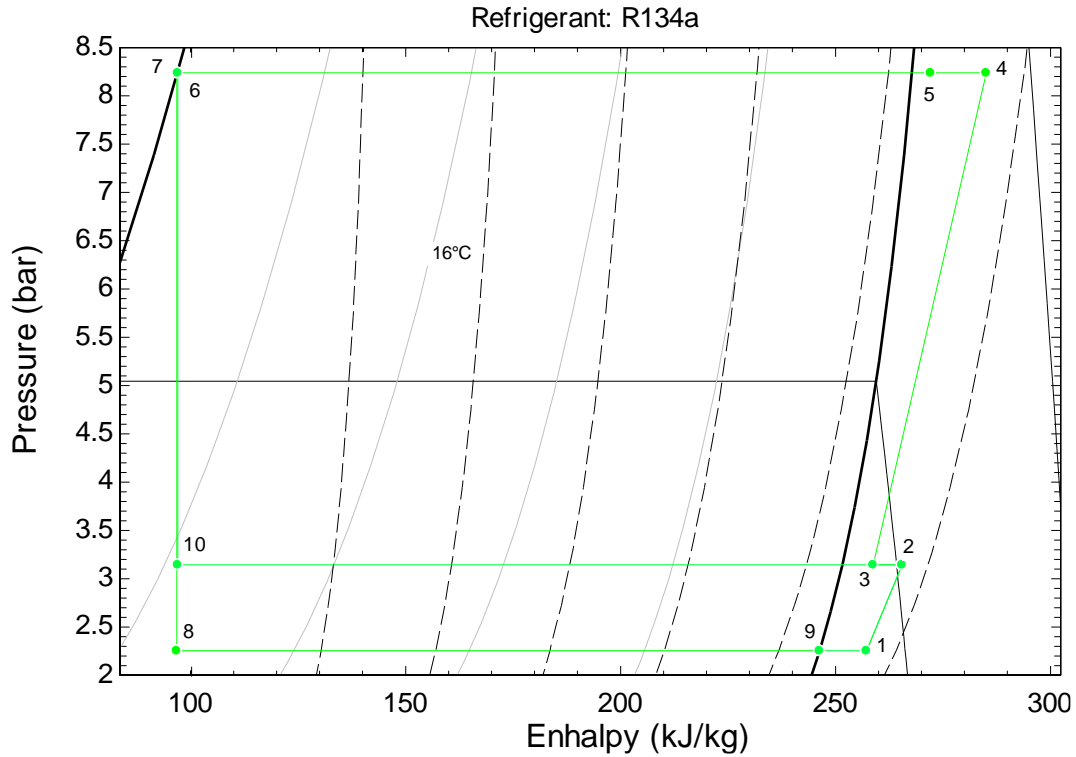


Figure 63: P, h diagram of the cycle at 101% load during baseline test [48]

Table 30: Thermodynamic properties in cycle during 101% load baseline test run [48]

State	p	T	u	h	s	x	$\rho$	v
Point	bar	K	kg/kJ	kg/kJ	kg/kJ·K	-	kg/m <sup>3</sup>	m <sup>3</sup> /kg
1	2.26	278.7	235.90	257.20	0.9756	100	10.57	0.0946
2	3.14	290.6	243.60	265.50	0.9756	100	14.33	0.0698
3	3.14	283.1	237.60	258.80	0.9560	100	14.85	0.0674
4	8.24	322.0	262.50	285.10	0.9732	100	36.48	0.0274
5	8.24	309.6	251.10	272.20	0.9323	100	39.18	0.0255
6	8.24	305.5	96.28	96.98	0.3589	0	1178.00	0.0008
7	8.24	305.4	96.10	96.80	0.3583	0	1179.00	0.0008
8	2.26	266.1	91.32	96.80	0.3739	0	41.17	0.0243
9	2.26	266.1	226.20	246.30	0.9356	1	11.23	0.0891
10	3.14	275.1	92.41	96.98	0.3684	1	68.70	0.0146

## APPENDIX II: P, h DIAGRAM OF THE ACCELERATED LIFE TEST CYCLES

### *High Load/Low Head Mode*

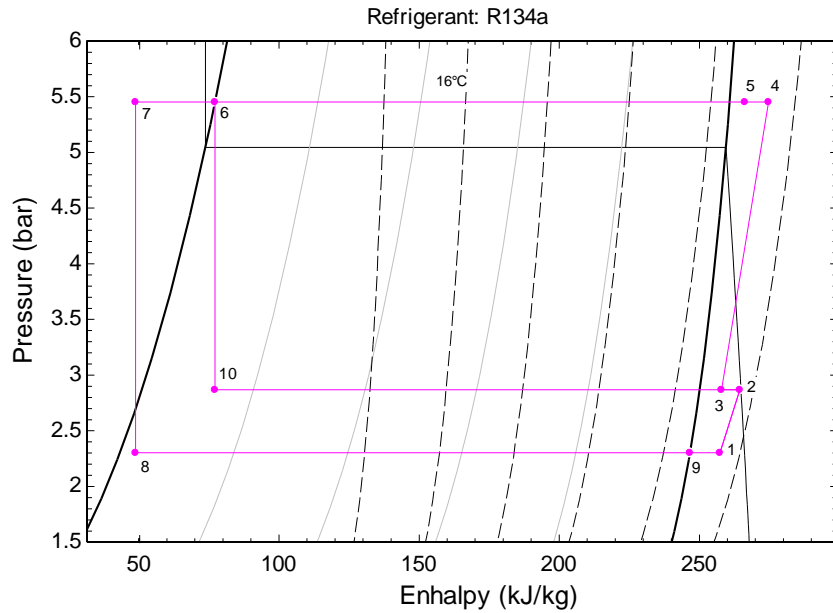


Figure 64: P, h diagram of the "high load/low head" test cycle conditions [48]

Table 31: Thermodynamic properties in cycle during "high load/low head" test cycle conditions [48]

State	p	T	u	h	s	x	$\rho$	v
Point	bar	K	kg/kJ	kg/kJ	kg/kJ·K	-	kg/m <sup>3</sup>	m <sup>3</sup> /kg
<b>1</b>	2.30	279.0	236.00	257.30	0.9744	100	10.80	0.0926
<b>2</b>	2.87	288.7	242.50	264.40	0.9744	100	13.09	0.0764
<b>3</b>	2.87	281.3	236.70	257.90	0.9598	100	13.54	0.0738
<b>4</b>	5.45	305.9	252.40	274.70	0.9694	100	24.55	0.0407
<b>5</b>	5.45	297.2	245.00	266.30	0.9416	100	25.68	0.0389
<b>6</b>	5.45	291.6	76.72	77.17	0.2933	0	1231.00	0.0008
<b>7</b>	5.45	270.8	48.56	48.77	0.1931	0	1262.00	0.0008
<b>8</b>	2.30	266.7	48.06	48.77	0.1934	0	320.30	0.0031
<b>9</b>	2.30	266.7	226.50	246.60	0.9353	1	11.46	0.0873
<b>10</b>	2.87	272.6	74.31	77.17	0.2973	1	100.60	0.0099

*Low Load/High Head Mode*

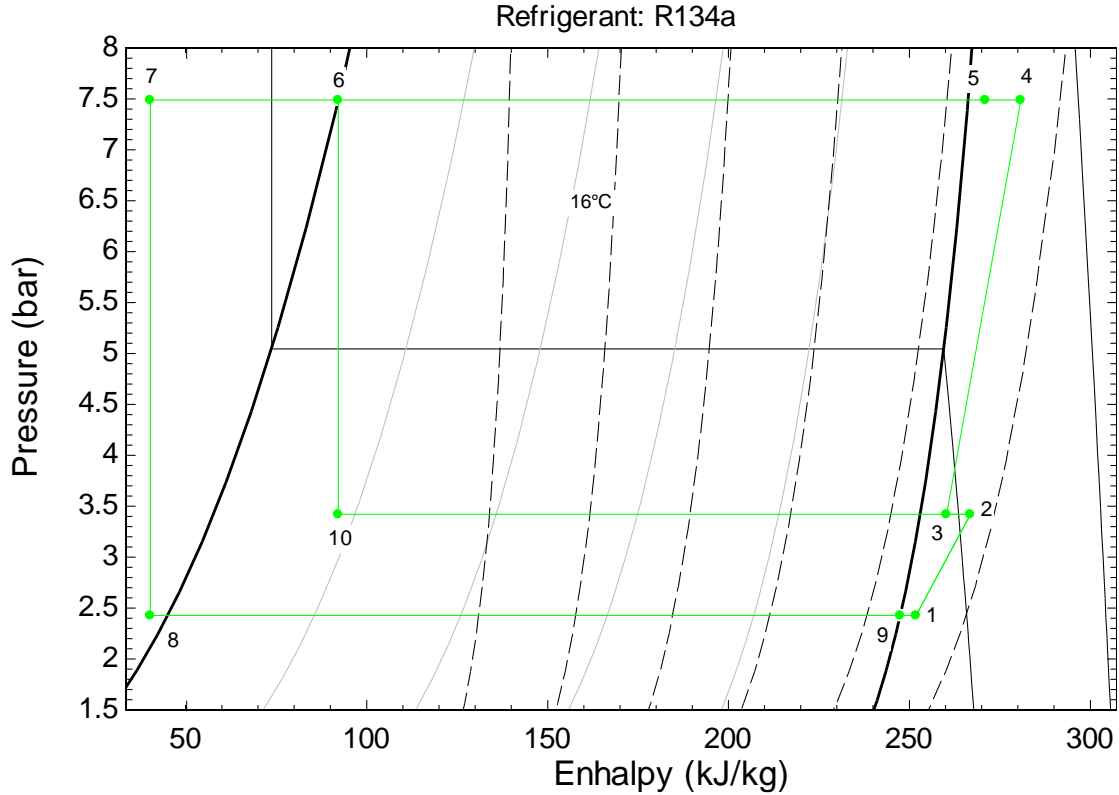


Figure 65: P, h diagram of the "low load/high head" test cycle conditions [48]

Table 32: Thermodynamic properties in cycle during "low load/high head" test cycle conditions [48]

State	<b>p</b>	<b>T</b>	<b>u</b>	<b>h</b>	<b>s</b>	<b>x</b>	<b>ρ</b>	<b>v</b>
Point	<i>bar</i>	<i>K</i>	<i>kg/kJ</i>	<i>kg/kJ</i>	<i>kg/kJ·K</i>	-	<i>kg/m<sup>3</sup></i>	<i>m<sup>3</sup>/kg</i>
<b>1</b>	2.43	273.0	231.20	251.80	0.9505	100	11.75	0.0851
<b>2</b>	3.42	292.8	244.90	266.90	0.9505	100	15.55	0.0643
<b>3</b>	3.42	285.5	239.00	260.20	0.9549	100	16.10	0.0621
<b>4</b>	7.49	316.3	258.50	280.80	0.9663	100	33.60	0.0298
<b>5</b>	7.49	306.8	249.90	271.00	0.9349	100	35.46	0.0282
<b>6</b>	7.49	302.2	91.53	92.16	0.3433	0	1191.00	0.0008
<b>7</b>	7.49	264.3	39.69	40.26	0.1599	0	1325.00	0.0008
<b>8</b>	2.43	264.4	40.08	40.26	0.1615	0	1316.00	0.0008
<b>9</b>	2.43	268.1	227.30	247.50	0.9344	1	12.05	0.0830
<b>10</b>	3.42	277.5	88.34	92.16	0.3496	1	89.57	0.0112

## APPENDIX III: P, H DIAGRAM OF THE RECURRING PERFORMANCE TEST CYCLES

*31% Part Load (Date: 01/12/2022)*

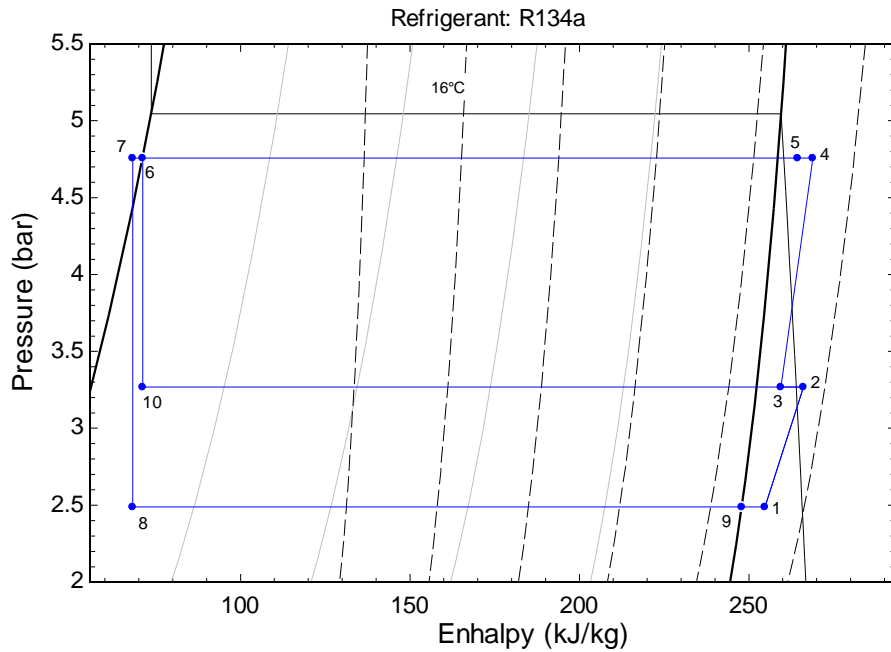


Figure 66 : P, h diagram of the cycle at 31% load during 1000 h-test [48]

Table 33: Thermodynamic properties in cycle during 1000 h-test at 31% load [48]

State	p	T	u	h	s	x	$\rho$	v
Point	bar	K	kg/kJ	kg/kJ	kg/kJ·K	-	kg/m <sup>3</sup>	m <sup>3</sup> /kg
<b>1</b>	2.49	276.6	233.80	254.70	0.9592	100	11.87	0.0842
<b>2</b>	3.27	291.5	244.10	266.00	0.9592	100	14.89	0.0672
<b>3</b>	3.27	284.2	238.20	259.40	0.9554	100	15.41	0.0649
<b>4</b>	4.76	298.2	247.10	268.90	0.9601	100	21.85	0.0458
<b>5</b>	4.76	293.4	243.10	264.30	0.9448	100	22.39	0.0447
<b>6</b>	4.76	287.3	70.80	71.18	0.2728	0	1246.00	0.0008
<b>7</b>	4.76	285.2	67.85	68.23	0.2625	0	1254.00	0.0008
<b>8</b>	2.49	268.7	65.84	68.23	0.2656	0	103.90	0.0096
<b>9</b>	2.49	268.7	227.70	247.90	0.9340	1	12.34	0.0810
<b>10</b>	3.27	276.2	69.37	71.18	0.2743	1	180.20	0.0055

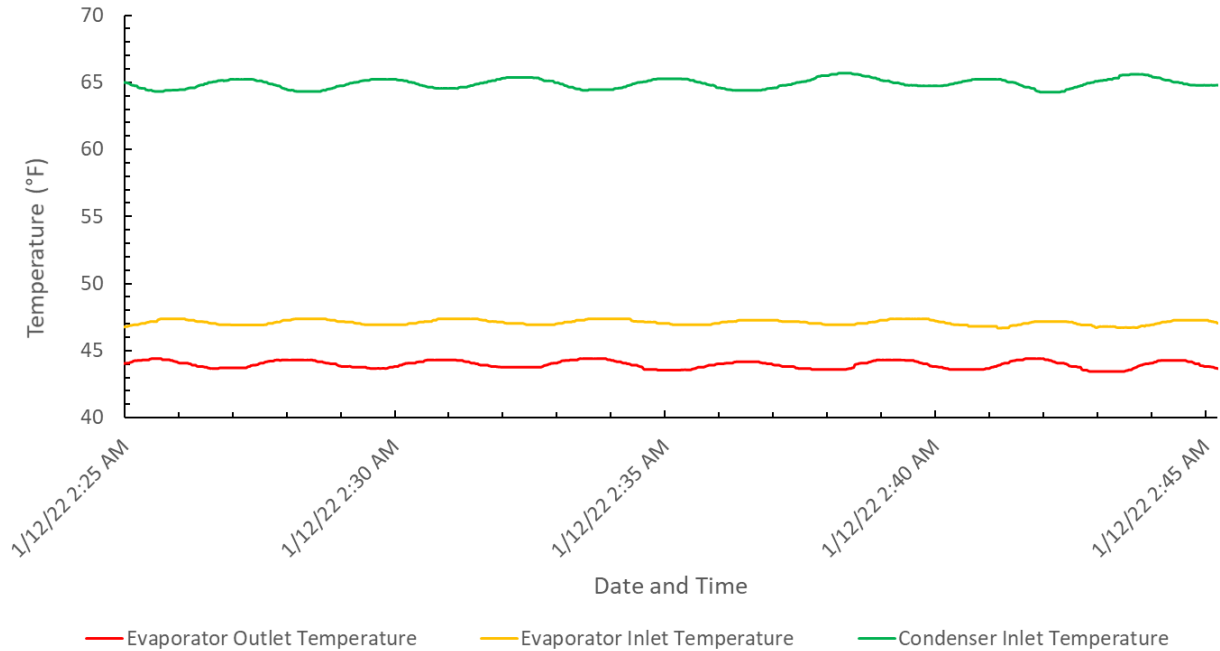


Figure 67: Fluid temperatures during 31% load recurring performance test

Table 34: Evaluated data at 31% load (1000 h-test)

<b>Load Rate in %</b>	<b>31</b>
Flow Rate over the Evaporator in <i>GPM</i>	300.42
Mass Flow (Evaporator) in <i>kg/s</i>	18.94
Cooling Capacity in <i>kW</i>	138.10
Cooling Capacity in <i>RT</i>	39.27
Average Temperature in the Evaporator in $^{\circ}\text{C}$	7.50
Evaporator Inlet Temperature in $^{\circ}\text{C}$	8.36
Evaporator Outlet Temperature in $^{\circ}\text{C}$	6.63
Electrical Input Power Value in <i>kW</i>	14.72
Coefficient of Performance COP	<b>9.38</b>
Unit Efficiency according to AHRI 550/590 Standard in <i>kW/RT</i>	<b>0.3749</b>

32% Part Load (Date: 01/12/2022)

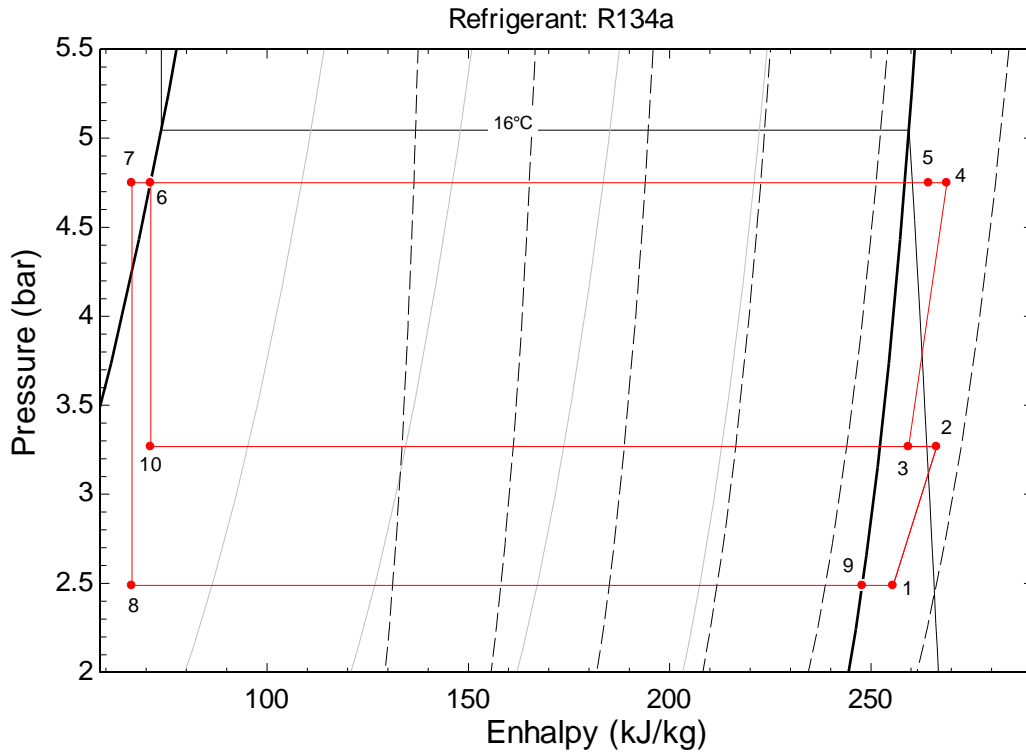


Figure 68: P, h diagram of the cycle at 32% load during 1000 h-test [48]

Table 35: Thermodynamic properties in cycle during 1000 h-test at 32% load [48]

State	p	T	u	h	s	x	$\rho$	v
Point	bar	K	kg/kJ	kg/kJ	kg/kJ·K	-	kg/m <sup>3</sup>	m <sup>3</sup> /kg
1	2.49	277.5	234.50	255.50	0.9621	100	11.82	0.0846
2	3.27	291.8	244.30	266.30	0.9621	100	14.86	0.0673
3	3.27	284.1	238.20	259.40	0.9553	100	15.42	0.0649
4	4.75	298.2	247.10	268.90	0.9603	100	21.81	0.0458
5	4.75	293.4	243.10	264.30	0.9450	100	22.36	0.0447
6	4.75	287.3	70.74	71.12	0.2726	0	1247.00	0.0008
7	4.75	283.8	66.00	66.38	0.2560	0	1259.00	0.0008
8	2.49	268.7	64.17	66.38	0.2587	0	112.50	0.0089
9	2.49	268.7	227.70	247.90	0.9340	1	12.34	0.0810
10	3.27	276.2	69.31	71.12	0.2741	1	180.90	0.0055

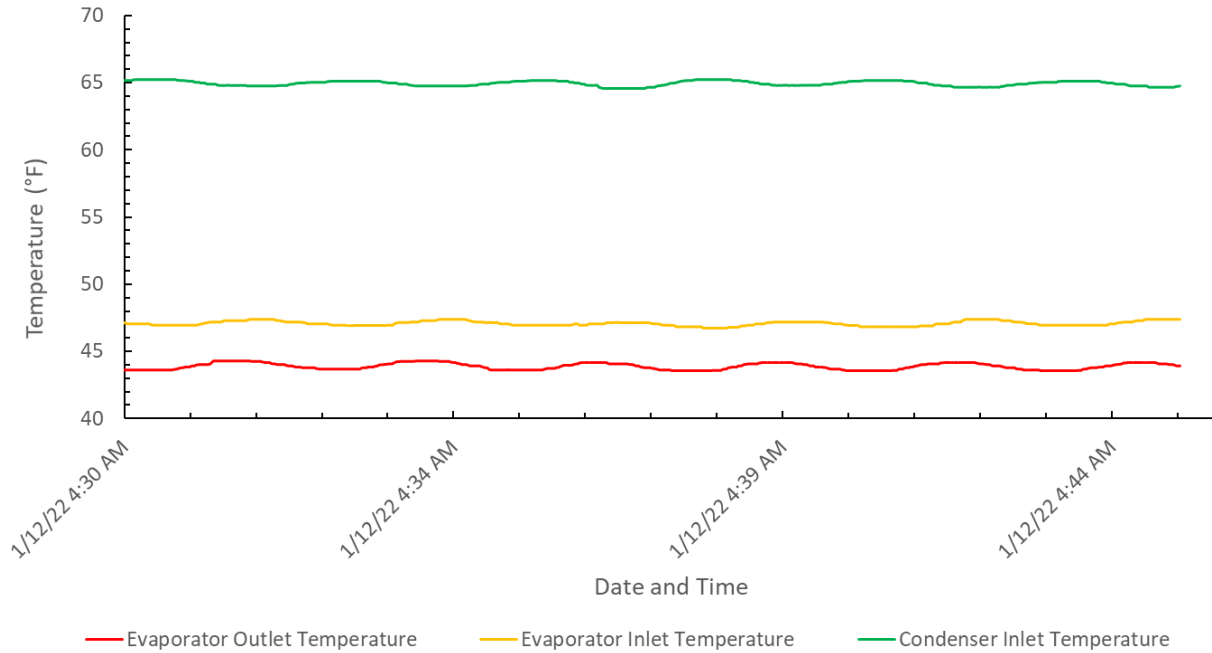


Figure 69: Fluid temperatures during 32% load recurring performance test

Table 36: Evaluated data at 32% load (1000 h-test)

<b>Load Rate in %</b>	<b>32</b>
Flow Rate over the Evaporator in <i>GPM</i>	300.37
Mass Flow (Evaporator) in <i>kg/s</i>	18.94
Cooling Capacity in <i>kW</i>	140.03
Cooling Capacity in <i>RT</i>	39.82
Average Temperature in the Evaporator in <i>°C</i>	7.49
Evaporator Inlet Temperature in <i>°C</i>	8.37
Evaporator Outlet Temperature in <i>°C</i>	6.61
Electrical Input Power Value in <i>kW</i>	14.52
Coefficient of Performance COP	<b>9.65</b>
Unit Efficiency according to AHRI 550/590 Standard in <i>kW/RT</i>	<b>0.3646</b>

49% Part Load (Date: 01/12/2022)

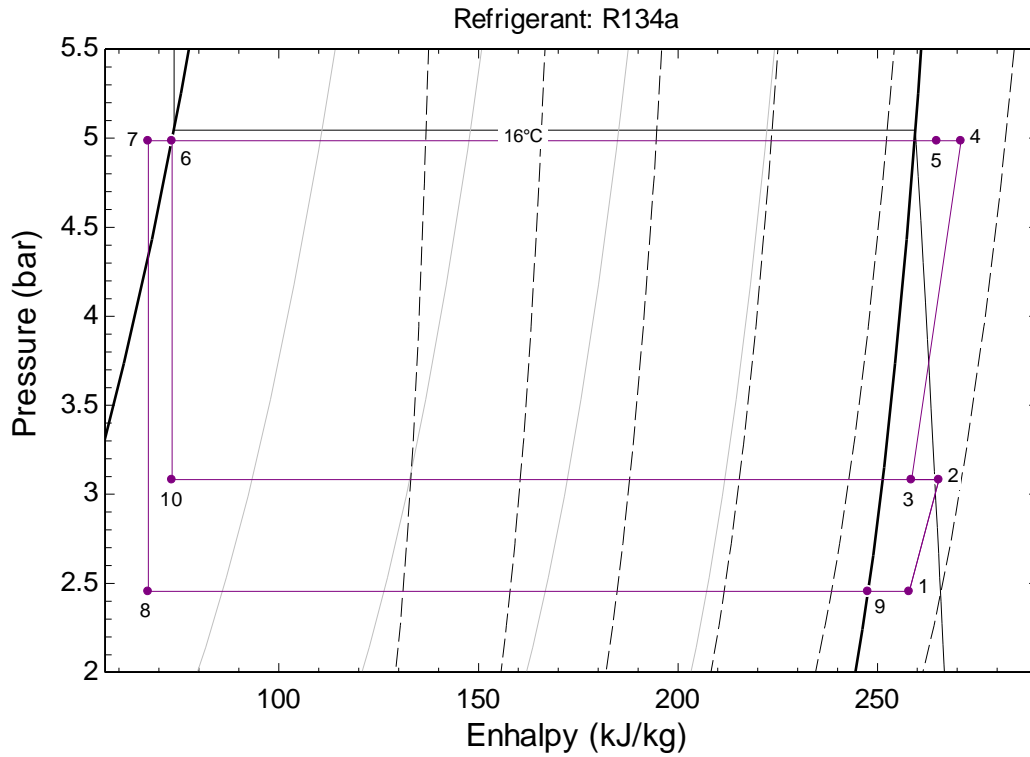


Figure 70: P, h diagram of the cycle at 49% load during 1000 h-test [48]

Table 37: Thermodynamic properties in cycle during 1000 h-test at 49% load [48]

State	p	T	u	h	s	x	$\rho$	v
Point	bar	K	kg/kJ	kg/kJ	kg/kJ·K	-	kg/m <sup>3</sup>	m <sup>3</sup> /kg
1	2.46	280.2	236.60	258.00	0.9718	100	11.50	0.0870
2	3.08	290.4	243.50	265.40	0.9718	100	14.04	0.0712
3	3.08	282.6	237.30	258.50	0.9565	100	14.56	0.0687
4	4.99	300.9	249.00	270.90	0.9637	100	22.72	0.0440
5	4.99	294.6	243.70	264.90	0.9433	100	23.48	0.0426
6	4.99	288.8	72.80	73.20	0.2798	0	1241.00	0.0008
7	4.99	284.5	66.86	67.26	0.2591	0	1257.00	0.0008
8	2.46	268.4	64.92	67.26	0.2621	0	104.90	0.0095
9	2.46	268.4	227.50	247.60	0.9342	1	12.18	0.0821
10	3.08	274.6	70.98	73.20	0.2821	1	139.00	0.0072

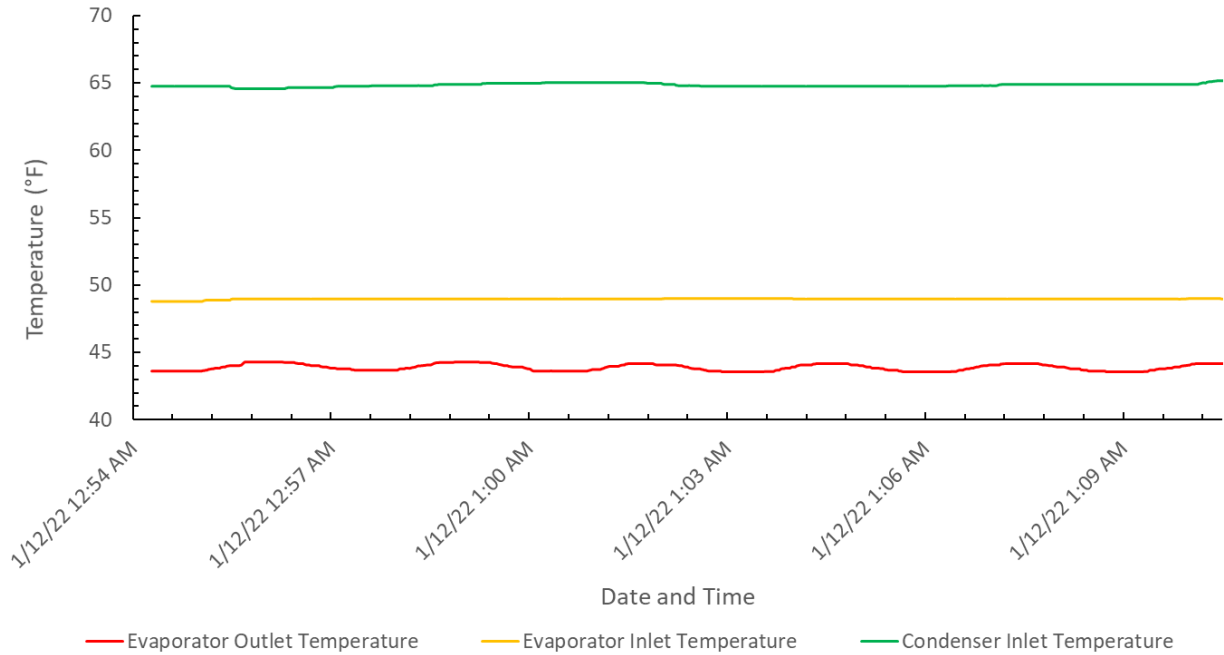


Figure 71: Fluid temperatures during 49% load recurring performance test

Table 38: Evaluated data at 49% load (1000 h-test)

<b>Load Rate in %</b>	<b>49</b>
Flow Rate over the Evaporator in <i>GPM</i>	300.64
Mass Flow (Evaporator) in <i>kg/s</i>	18.96
Cooling Capacity in <i>kW</i>	216.96
Cooling Capacity in <i>RT</i>	61.69
Average Temperature in the Evaporator in <i>°C</i>	8.07
Evaporator Inlet Temperature in <i>°C</i>	9.43
Evaporator Outlet Temperature in <i>°C</i>	6.71
Electrical Input Power Value in <i>kW</i>	22.26
Coefficient of Performance COP	<b>9.75</b>
Unit Efficiency according to AHRI 550/590 Standard in <i>kW/RT</i>	<b>0.3608</b>

50% Part Load (Date: 01/11/2022)

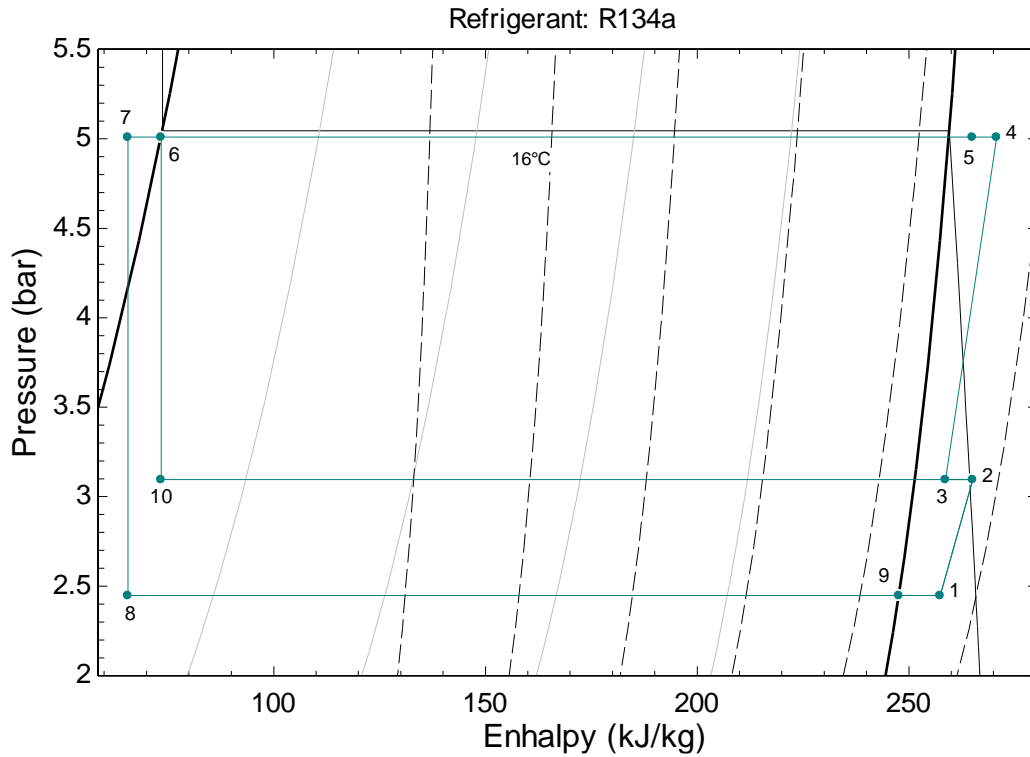


Figure 72: P, h diagram of the cycle at 50% load during 1000 h-test [48]

Table 39: Thermodynamic properties in cycle during 1000 h-test at 50% load [48]

State	p	T	u	h	s	x	$\rho$	v
Point	bar	K	kg/kJ	kg/kJ	kg/kJ·K	-	kg/m <sup>3</sup>	m <sup>3</sup> /kg
1	2.45	279.5	236.10	257.30	0.9698	100	11.51	0.0869
2	3.10	290.0	243.10	265.00	0.9698	100	14.13	0.0708
3	3.10	282.7	237.40	258.60	0.9565	100	14.62	0.0684
4	5.01	300.8	248.80	270.70	0.9626	100	22.87	0.0437
5	5.01	294.8	243.80	265.00	0.9433	100	23.59	0.0424
6	5.01	288.9	73.00	73.41	0.2805	0	1241.00	0.0008
7	5.01	283.3	65.29	65.63	0.2535	0	1255.00	0.0008
8	2.45	268.3	63.44	65.63	0.2561	0	111.90	0.0089
9	2.45	268.3	227.40	247.60	0.9343	1	12.15	0.0823
10	3.10	274.7	71.18	73.41	0.2828	1	139.20	0.0072

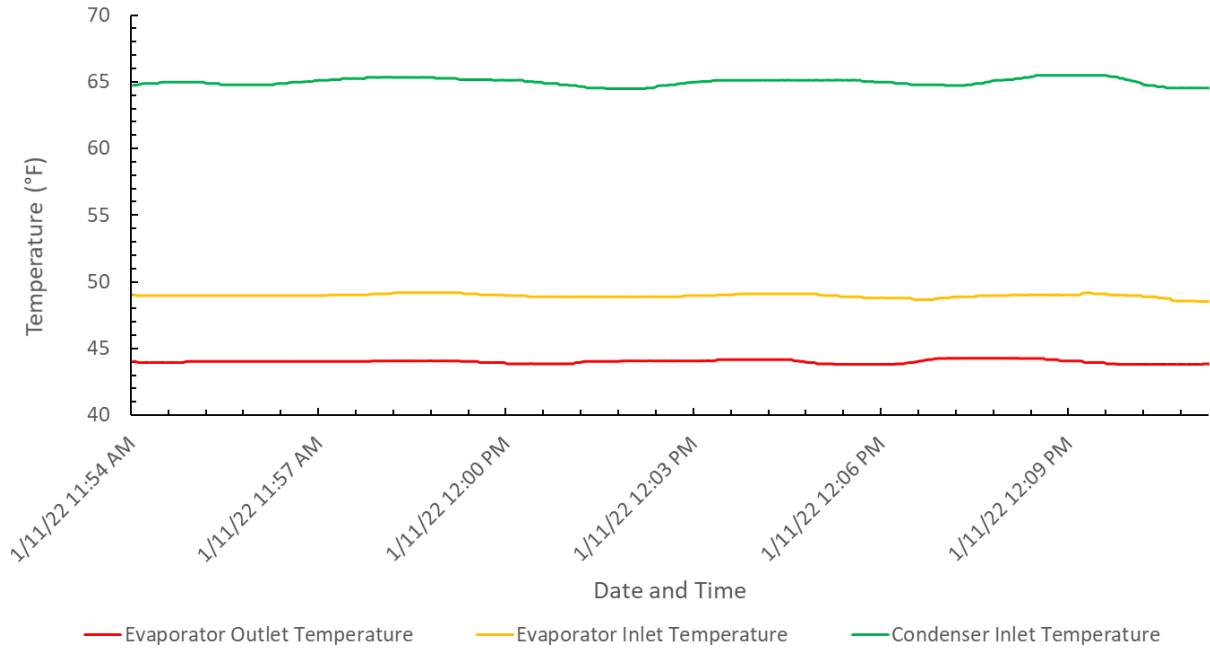


Figure 73: Fluid temperatures during 50% load recurring performance test

Table 40: Evaluated data at 50% load (1000 h-test)

<b>Load Rate in %</b>	<b>50</b>
Flow Rate over the Evaporator in <i>GPM</i>	301.03
Mass Flow (Evaporator) in <i>kg/s</i>	18.98
Cooling Capacity in <i>kW</i>	218.30
Cooling Capacity in <i>RT</i>	62.07
Average Temperature in the Evaporator in $^{\circ}C$	8.05
Evaporator Inlet Temperature in $^{\circ}C$	9.42
Evaporator Outlet Temperature in $^{\circ}C$	6.68
Electrical Input Power Value in <i>kW</i>	22.81
Coefficient of Performance COP	<b>9.57</b>
Unit Efficiency according to AHRI 550/590 Standard in <i>kW/RT</i>	<b>0.3675</b>

76% Part Load (Date: 01/11/2022)

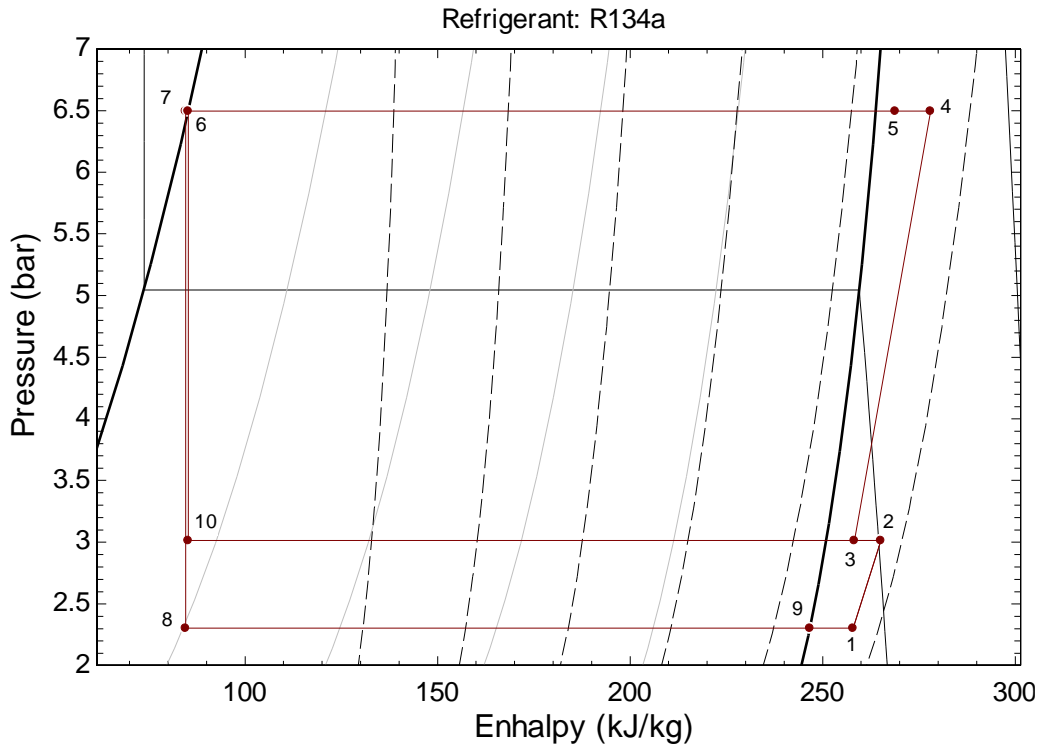


Figure 74: P, h diagram of the cycle at 76% load during 1000 h-test [48]

Table 41: Thermodynamic properties in cycle during 1000 h-test at 76% load [48]

State	p	T	u	h	s	x	$\rho$	v
Point	bar	K	kg/kJ	kg/kJ	kg/kJ·K	-	kg/m <sup>3</sup>	m <sup>3</sup> /kg
<b>1</b>	2.30	279.6	236.50	257.80	0.9763	100	10.77	0.0929
<b>2</b>	3.01	289.8	243.20	265.10	0.9763	100	13.73	0.0728
<b>3</b>	3.01	282.1	237.00	258.20	0.9572	100	14.24	0.0702
<b>4</b>	6.50	311.5	255.70	278.00	0.9677	100	29.16	0.0343
<b>5</b>	6.50	302.3	247.60	268.80	0.9378	100	30.65	0.0326
<b>6</b>	6.50	297.3	84.68	85.22	0.3204	0	1210.00	0.0008
<b>7</b>	6.50	296.8	83.99	84.52	0.3180	0	1212.00	0.0008
<b>8</b>	2.30	266.7	80.30	84.52	0.3274	0	54.56	0.0183
<b>9</b>	2.30	266.7	226.50	246.60	0.9353	1	11.46	0.0873
<b>10</b>	3.01	273.9	81.71	85.22	0.3262	1	85.81	0.0117

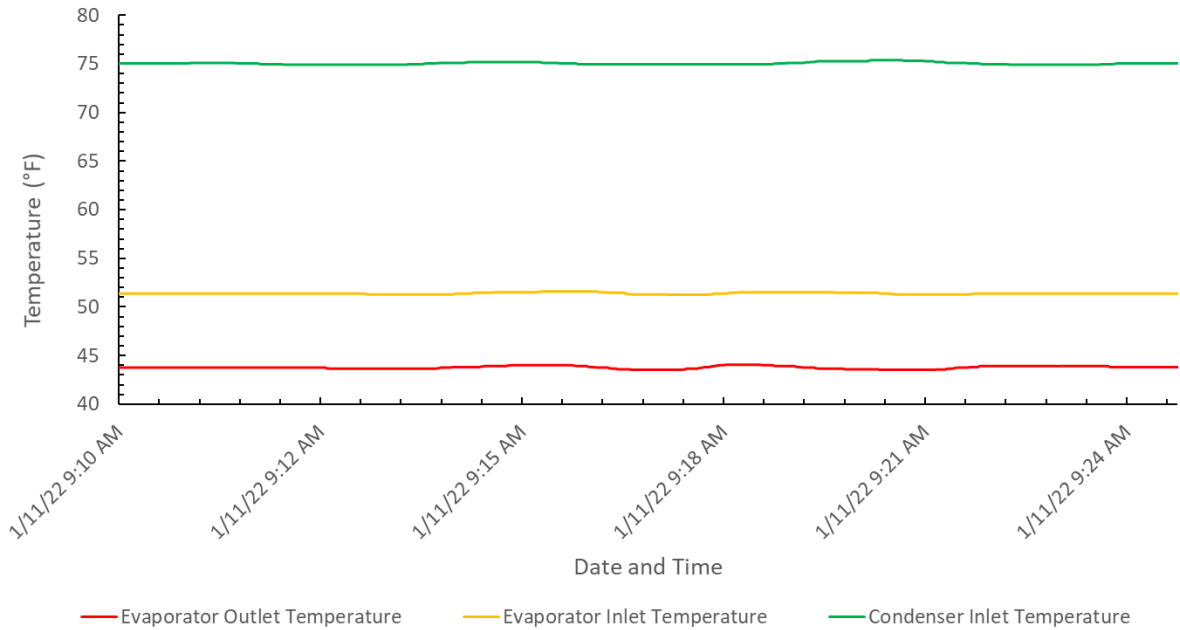


Figure 75: Fluid temperatures during 76% load recurring performance test

Table 42: Evaluated data at 76% load (1000 h-test)

<b>Load Rate in %</b>	<b>76</b>
Flow Rate over the Evaporator in <i>GPM</i>	299.90
Mass Flow (Evaporator) in <i>kg/s</i>	18.91
Cooling Capacity in <i>kW</i>	334.44
Cooling Capacity in <i>RT</i>	95.10
Average Temperature in the Evaporator in °C	8.66
Evaporator Inlet Temperature in °C	10.77
Evaporator Outlet Temperature in °C	6.56
Electrical Input Power Value in <i>kW</i>	49.29
Coefficient of Performance COP	<b>6.79</b>
Unit Efficiency according to AHRI 550/590 Standard in <i>kW/RT</i>	<b>0.5183</b>

85% Part Load (Date: 02/10/2022)

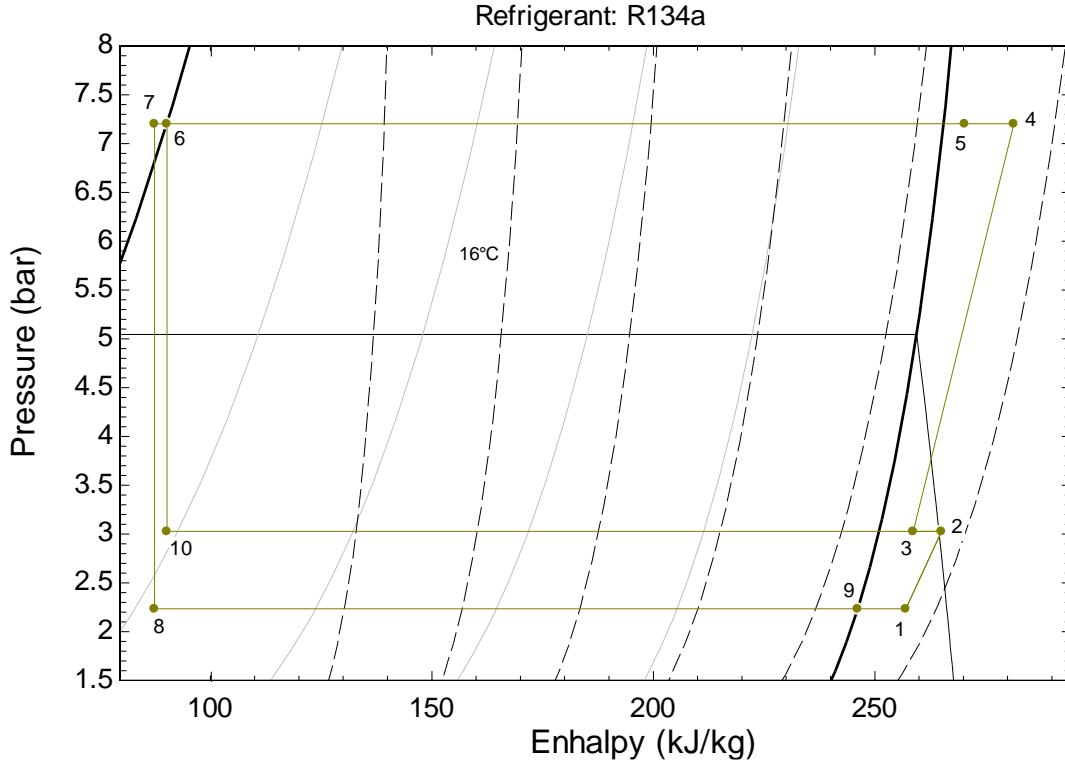


Figure 76: P, h diagram of the cycle at 85% load during 1000 h-test [48]

Table 43: Thermodynamic properties in cycle during 1000 h-test at 85% load [48]

State	<b>p</b>	<b>T</b>	<b>u</b>	<b>h</b>	<b>s</b>	<b>x</b>	<b><math>\rho</math></b>	<b>v</b>
Point	bar	K	kg/kJ	kg/kJ	kg/kJ·K	-	kg/m <sup>3</sup>	m <sup>3</sup> /kg
<b>1</b>	2.23	278.4	235.70	257.00	0.9755	100	10.48	0.0954
<b>2</b>	3.03	289.8	243.20	265.10	0.9755	100	13.80	0.0725
<b>3</b>	3.03	282.6	237.40	258.70	0.9585	100	14.27	0.0701
<b>4</b>	7.21	316.4	258.90	281.40	0.9710	100	32.09	0.0312
<b>5</b>	7.21	305.4	249.20	270.30	0.9354	100	34.09	0.0293
<b>6</b>	7.21	300.8	89.63	90.23	0.3369	0	1196.00	0.0008
<b>7</b>	7.21	298.9	86.84	87.44	0.3276	0	1204.00	0.0008
<b>8</b>	2.23	265.9	82.85	87.44	0.3389	0	48.71	0.0205
<b>9</b>	2.23	265.9	226.10	246.20	0.9358	1	11.13	0.0899
<b>10</b>	3.03	274.0	86.23	90.23	0.3444	1	75.57	0.0132

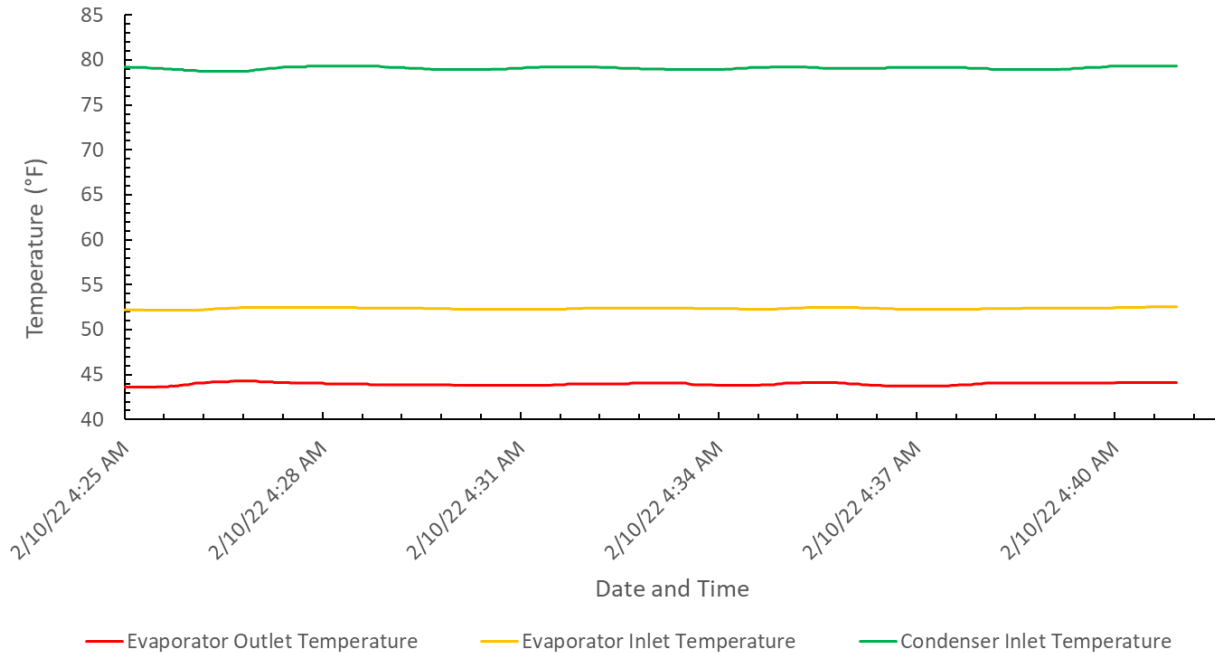


Figure 77: Fluid temperatures during 85% load recurring performance test

Table 44: Evaluated data at 85% load (1000 h-test)

<b>Load Rate in %</b>	<b>85</b>
Flow Rate over the Evaporator in <i>GPM</i>	300.70
Mass Flow (Evaporator) in <i>kg/s</i>	18.96
Cooling Capacity in <i>kW</i>	374.34
Cooling Capacity in <i>RT</i>	106.44
Average Temperature in the Evaporator in $^{\circ}C$	8.97
Evaporator Inlet Temperature in $^{\circ}C$	11.32
Evaporator Outlet Temperature in $^{\circ}C$	6.62
Electrical Input Power Value in <i>kW</i>	63.81
Coefficient of Performance COP	<b>5.87</b>
Unit Efficiency according to AHRI 550/590 Standard in <i>kW/RT</i>	<b>0.5995</b>

90% Part Load (Date: 02/12/2022)

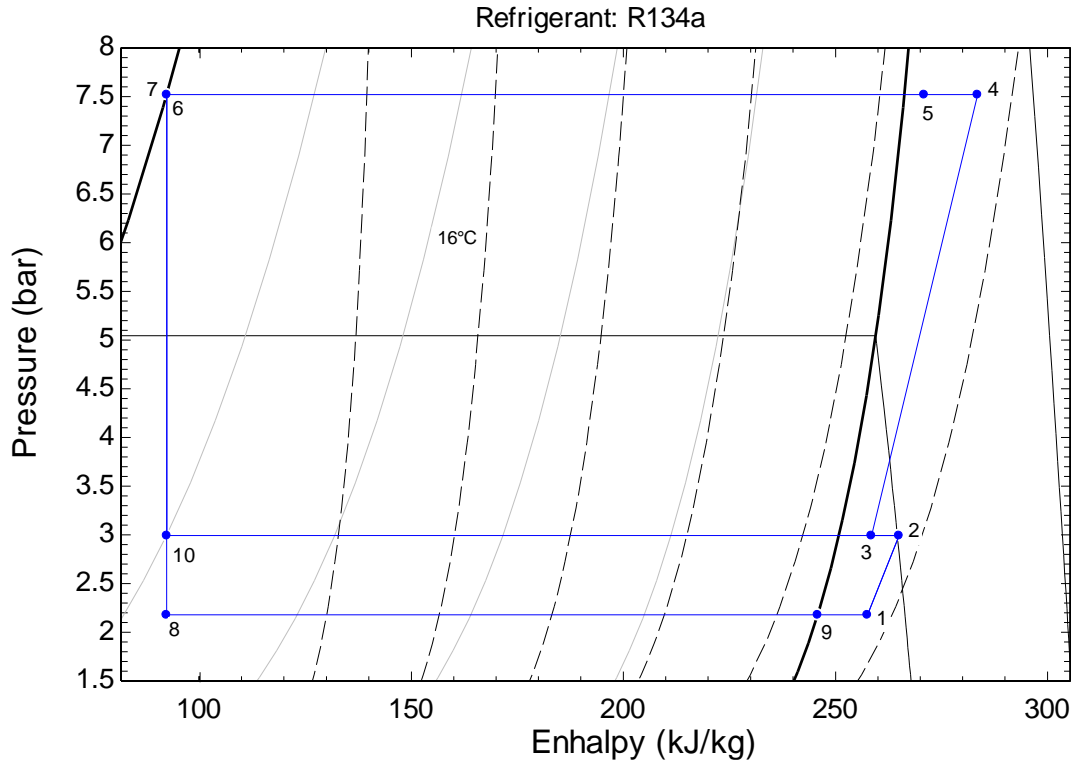


Figure 78: P, h diagram of the cycle at 90% load during 1000 h-test [48]

Table 45: Thermodynamic properties in cycle during 1000 h-test at 90% load [48]

State	<b>p</b>	<b>T</b>	<b>u</b>	<b>h</b>	<b>s</b>	<b>x</b>	<b>ρ</b>	<b>v</b>
Point	bar	K	kg/kJ	kg/kJ	kg/kJ·K	-	kg/m <sup>3</sup>	m <sup>3</sup> /kg
<b>1</b>	2.18	278.9	236.10	257.50	0.9793	100	10.18	0.0982
<b>2</b>	2.99	289.6	243.00	264.90	0.9793	100	13.64	0.0733
<b>3</b>	2.99	282.4	237.30	258.50	0.9589	100	14.11	0.0709
<b>4</b>	7.52	319.1	260.90	283.50	0.9746	100	33.28	0.0301
<b>5</b>	7.52	306.8	249.80	270.90	0.9344	100	35.64	0.0281
<b>6</b>	7.52	302.3	91.73	92.37	0.3439	0	1191.00	0.0008
<b>7</b>	7.52	302.2	91.64	92.27	0.3436	0	1191.00	0.0008
<b>8</b>	2.18	265.2	87.15	92.27	0.3575	0	42.55	0.0235
<b>9</b>	2.18	265.2	225.70	245.80	0.9362	1	10.87	0.0920
<b>10</b>	2.99	273.7	88.11	92.37	0.3524	1	70.30	0.0142

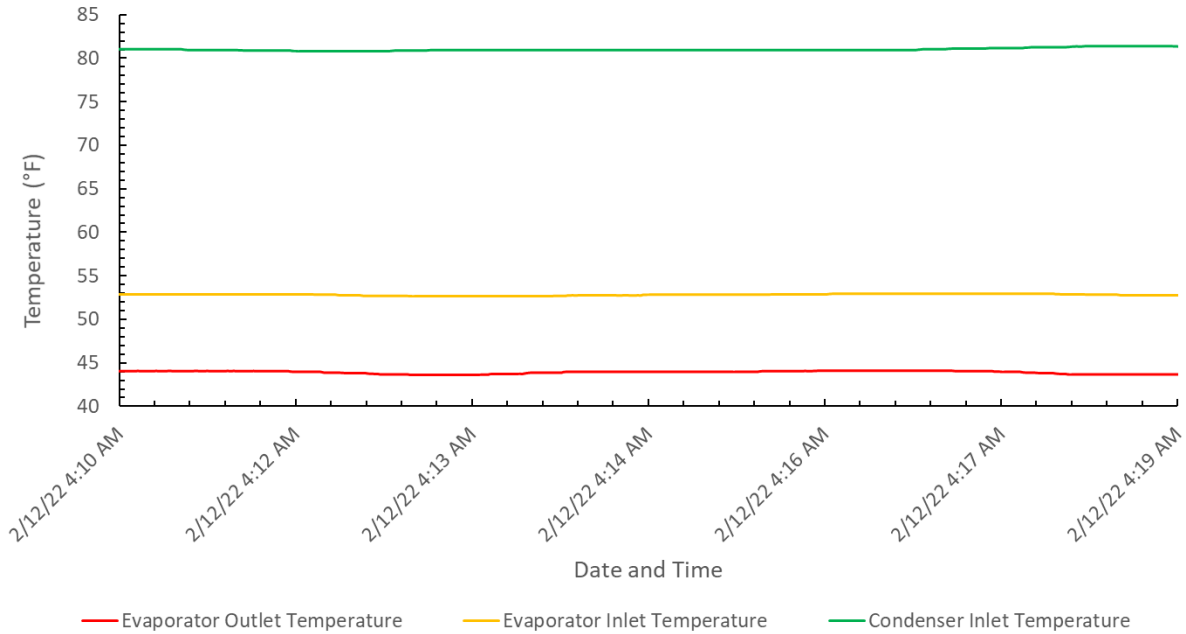


Figure 79: Fluid temperatures during 90% load recurring performance test

Table 46: Evaluated data at 90% load (1000 h-test)

<b>Load Rate in %</b>	<b>90</b>
Flow Rate over the Evaporator in <i>GPM</i>	300.81
Mass Flow (Evaporator) in <i>kg/s</i>	18.97
Cooling Capacity in <i>kW</i>	397.16
Cooling Capacity in <i>RT</i>	112.93
Average Temperature in the Evaporator in °C	9.09
Evaporator Inlet Temperature in °C	11.58
Evaporator Outlet Temperature in °C	6.60
Electrical Input Power Value in <i>kW</i>	72.04
Coefficient of Performance COP	<b>5.51</b>
Unit Efficiency according to AHRI 550/590 Standard in <i>kW/RT</i>	<b>0.6379</b>

100% Full Load (Date: 02/22/2022)

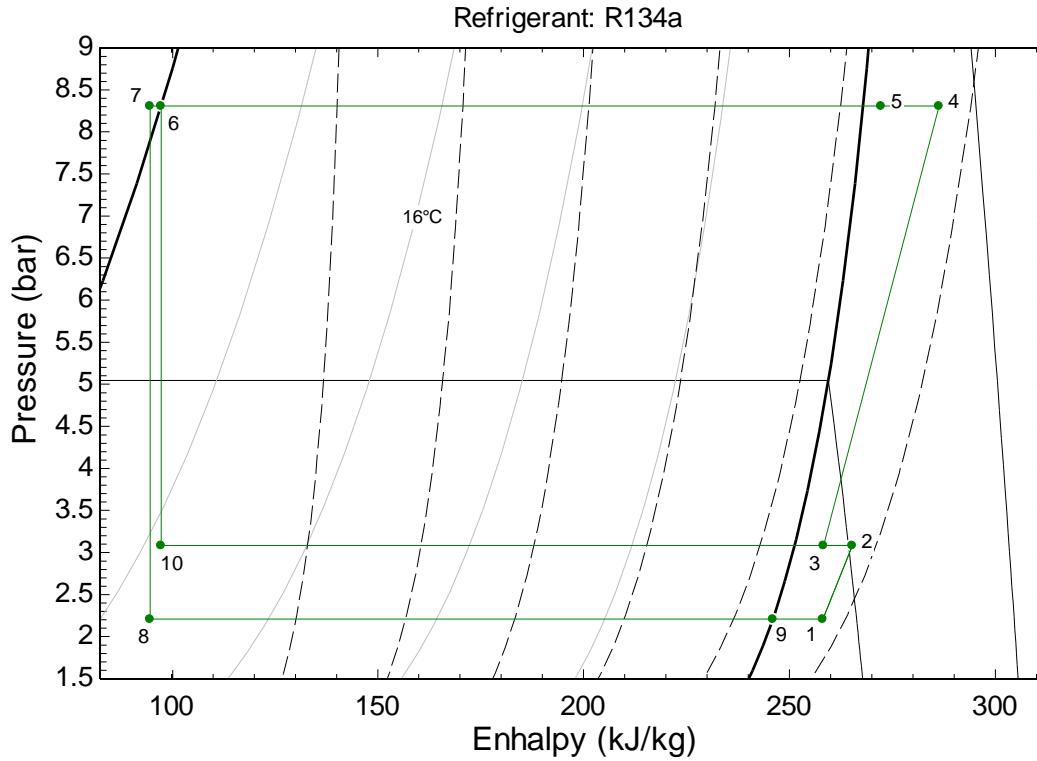


Figure 80: P, h diagram of the cycle at 100% load during 1000 h-test [48]

Table 47: Thermodynamic properties in cycle during 1000 h-test at 100% load [48]

State	p	T	u	h	s	x	$\rho$	v
Point	bar	K	kg/kJ	kg/kJ	kg/kJ·K	-	kg/m <sup>3</sup>	m <sup>3</sup> /kg
1	2.21	279.7	236.70	258.10	0.9806	100	10.28	0.0972
2	3.08	290.2	243.30	265.30	0.9806	100	14.05	0.0712
3	3.08	282.4	237.20	258.30	0.9559	100	14.57	0.0686
4	8.31	323.4	263.60	286.30	0.9765	100	36.59	0.0273
5	8.31	309.9	251.30	272.30	0.9321	100	39.52	0.0253
6	8.31	305.8	96.71	97.41	0.3603	0	1177.00	0.0008
7	8.31	303.9	94.03	94.73	0.3515	0	1185.00	0.0008
8	2.21	265.6	89.40	94.73	0.3666	0	41.40	0.0242
9	2.21	265.6	225.90	246.00	0.9360	1	11.00	0.0909
10	3.08	274.6	92.73	97.41	0.3703	1	65.85	0.0152

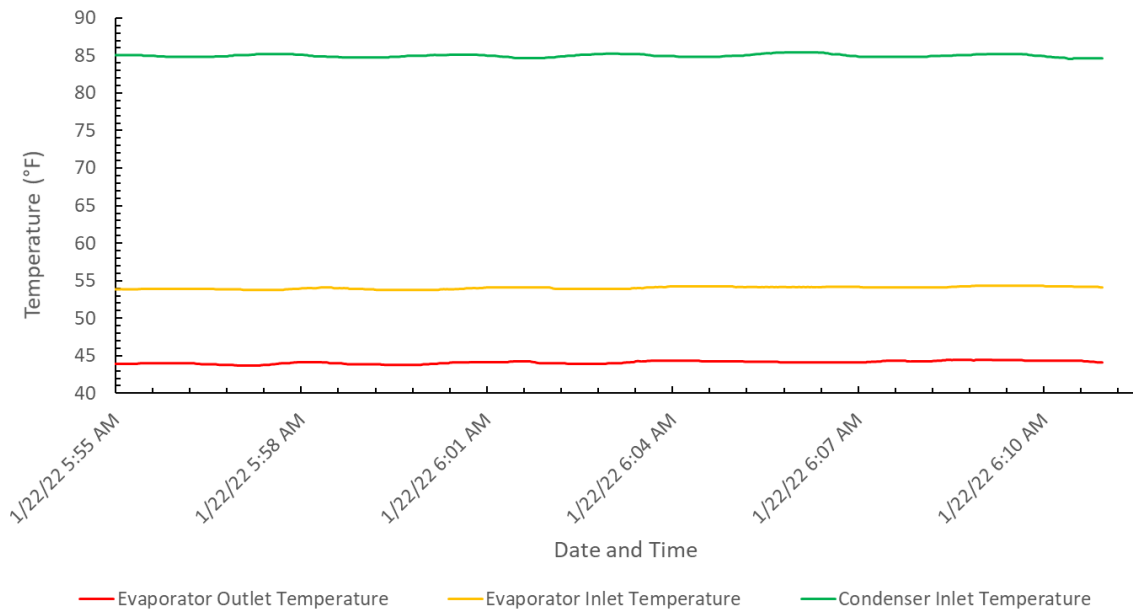


Figure 81: Fluid temperatures during 100% load recurring performance test

Table 48 : Evaluated data at 100% load (1000 h-test)

<b>Load Rate in %</b>	<b>100</b>
Flow Rate over the Evaporator in <i>GPM</i>	302.12
Mass Flow (Evaporator) in <i>kg/s</i>	19.05
Cooling Capacity in <i>kW</i>	439.62
Cooling Capacity in <i>RT</i>	125.01
Average Temperature in the Evaporator in $^{\circ}\text{C}$	9.49
Evaporator Inlet Temperature in $^{\circ}\text{C}$	12.23
Evaporator Outlet Temperature in $^{\circ}\text{C}$	6.74
Electrical Input Power Value in <i>kW</i>	88.02
Coefficient of Performance COP	<b>4.99</b>
Unit Efficiency according to AHRI 550/590 Standard in <i>kW/RT</i>	<b>0.7042</b>

## REFERENCES

- [1] IEA, “Electricity”, Data Browser, Global Energy Review, International Energy Agency, 2020, Retrieved from <https://www.iea.org/fuels-and-technologies/electricity>
- [2] IEA, “Electricity Market Report”, International Energy Agency, 2022, Retrieved from [https://iea.blob.core.windows.net/assets/d75d928b-9448-4c9b-b13d-6a92145af5a3/ElectricityMarketReport\\_January2022.pdf](https://iea.blob.core.windows.net/assets/d75d928b-9448-4c9b-b13d-6a92145af5a3/ElectricityMarketReport_January2022.pdf)
- [3] US Census Bureau, “World Population Review – Electricity Consumption by Country”, Retrieved from <https://worldpopulationreview.com/country-rankings/electricity-consumption-by-country>
- [4] IEA, “The future of cooling – opportunities for energy efficient air conditioning”, OECD/IEA, 2018, retrieved from <https://www.iea.org/reports/the-future-of-cooling>
- [5] U.S. Department of Energy, “Quadrennial Technology Review – An Assessment of Energy Technologies and Research Opportunities”, Chapter 5: Increasing Efficiency of Building Systems and Technologies, 2015, retrieved from <https://www.energy.gov/quadrennial-technology-review-2015>
- [6] IEA, “Cooling”, Data Browser, Global Energy Review, International Energy Agency, 2020, Retrieved from <https://www.iea.org/fuels-and-technologies/cooling>
- [7] EIA, “Annual energy outlook 2019 with projections to 2050”, Annual Energy Outlook 2019 with Projections to 2050., vol. 44, pp. 1-64, 8, 2019
- [8] U.S. Department of Energy, “Buildings Energy Data Book”, 2011, Retrieved from <http://192.31.135.76/TableView.aspx?table=5.3.13>
- [9] EIA, “2018 Manufacturing Energy Consumption Survey Consumption Results”, Manufacturing Energy Consumption Survey, U.S. Energy Information Administration, 2021, Retrieved from <https://www.eia.gov/consumption/manufacturing/>
- [10] EIA, “Use of energy explained in depth - Energy use in industry”, Manufacturing Energy Consumption Survey, U.S. Energy Information Administration, 2021, Retrieved from <https://www.eia.gov/energyexplained/use-of-energy/industry-in-depth.php>
- [11] J. Koomey, E. Masanet, N. Horner, I. Azevedo, W. Lintner, “United States Data Center Energy Usage Report “, Ernest Orlando Lawrence Berkeley National Laboratory, 2016, retrieved from <https://eta.lbl.gov/publications/united-states-data-center-energy>
- [12] GreenRiverside, “Efficient Electric Chillers”, Energy Depot, 2000-2021, Retrieved from <http://www.energydepot.com/rpucom/library/hvac013.asp>
- [13] T. M. Rossi, J. E. Braun: “A statistical, rule-based fault detection and diagnostic method for vapor compression air conditioners”, in HVAC&R Research, Vol. 3, Issue 1 (1997), pp. 19-37, ISSN 1078-9669

- [14] M. C. Comstock, J. E. Braun: “Development of analysis tools for the evaluation of fault detection and diagnostics in chillers”, Master’s thesis, Ray W. Herrick Laboratories, Purdue University, West Lafayette, IN, 1999
- [15] I. B. D. McIntosh, J. W. Mitchell, W. A. Beckmann: “Fault detection and diagnosis in chillers – part I: Model development and discussion”, in ASHRAE Transactions, Technology Collection, Vol. 106 (2000), pp. 268
- [16] J. E. Braun, S. A. Klein, J. W. Mitchell, W. A. Beckmann: „Methodologies for the design and control of central cooling plants”, Ph. D. thesis, University of Wisconsin, Madison, WI, 1988
- [17] S. Bendapudi, J. E. Braun, E. A. Groll, T. M. Rossi, J. Y. Murthy: “Development and evaluation of modeling approaches for transients in centrifugal chillers”, Ph. D. thesis, Ray W. Herrick Laboratories, Purdue University, West Lafayette, IN, 2004
- [18] H. Li, J. E. Braun: “A methodology for diagnosing multiple simultaneous faults in vapor-compression air conditioners”, in HVAC&R Research, Vol. 13, Issue 2 (2007), pp. 369-395, ISSN 1078-9669
- [19] Q. Zhou, S. Wang, Z. Ma: “A model-based fault detection and diagnosis strategy for HVAC systems”, in International Journal of Energy Research, Vol. 33 (2009), pp. 303-918
- [20] A. Beghi, R. Brignoli, L. Cecchinato, G. Menegazzo, M. Rampazzo, F. Simmini: “Data-driven fault detection and diagnosis for HVAC water chillers”, in Control Engineering Practice, Vol. 53 (2016), pp. 79-91
- [21] A. L. Hjortland, J. E. Braun, W. T. Horton, E. A. Groll, N. Jain: “Automated fault detection, diagnostics, impact evaluation, and service decision-making for direct expansion air conditioners”, Ph. D. thesis, Ray W. Herrick Laboratories, Purdue University, West Lafayette, IN, 2018
- [22] W. Meslameni, T. Kamoun: “Detection of an imbalance fault by vibration monitoring: case of a screw compressor”, in Journal of Applied Research on Industrial Engineering, Vol. 8, Issue 1 (2021), pp. 27-39
- [23] R. Miller, W. Nelson: “Optimum simple step-stress plans for accelerated life testing”, IEEE Transactions on Reliability, Vol. R-32, Issue 1 (1983)
- [24] G. R. Pruitt, T. M. Davis, B. A. Ross: “Methods for accelerated life evaluation of long-life cryocoolers”, in AIP Conference Proceedings, No. 710 (2004)
- [25] S. Jayatilleka: “Performance verification throughout the product life cycle using accelerated life testing”, in IEEE Transactions on Annual Reliability and Maintainability symposium, 2018

- [26] M. W. Browne, B. K. Bansal, “Transient simulation of vapour-compression packaged liquid chillers”, in *International Journal of Refrigeration*, Vol. 25, Issue 5 (2002), pp. 597-610
- [27] L. Fu, G. Ding, Z. Su, G. Zhao, “Steady-state simulation of screw liquid chillers”, in *Applied Thermal Engineering*, Vol. 22, Issue 15 (2002), pp. 1731-1748
- [28] L. Fu, G. Ding, C. Zang, “Dynamic Simulation of air-to-water dual-mode heat pump with screw compressor”, in *Applied Thermal Engineering*, Vol. 23, Issue 13 (2003), pp. 1629-1645
- [29] G. Ding, Fu. L, “Performance analysis and improvement of air-to-water chiller for application in wide ambient temperature range”, in *Applied Thermal Engineering*, Vol. 25 (2005), pp.135-145
- [30] Y. Chang, “Application of Hopfield Neural Network to the optimal chilled water supply temperature calculation of air-conditioning systems for saving energy”, in *International Journal of Thermal Sciences*, Vol. 48, Issue 8 (2009), pp. 1649-1657
- [31] T. Lee, W. Lu, “An evaluation of empirically-based models for predicting energy performance of vapor-compression water chillers”, in *Applied Energy*, Vol. 87, Issue 11 (2010), pp. 3486-3493
- [32] C. Tian, Z. Xing, X. Pan, Y. Tian, “A method for COP prediction of an on-site screw chiller applied in cinema”, in *International Journal of Refrigeration*, Vol. 98 (2019), pp. 459-467
- [33] E. Sala-Cardoso, M. Delgado-Prieto, K. Kampouropoulos, L. Romeral, “Predictive chiller operation: A data-driven loading and scheduling approach”, in *Energy and Buildings*, Vol. 208 (2020)
- [34] X. Zhu, S. Zhang, X. Jin, Z. Du, “Deep learning-based reference model for operational risk evaluation of screw chillers for energy efficiency”, in *Energy*, Vol. 213 (2020)
- [35] Y. Bao, S. Lee, J. Jia, W. Lee, “Developing an integrated part load value for chillers of office buildings in Hong Kong”, in *International Journal of Refrigeration*, Vol. 129 (2021), pp. 139-152
- [36] E. Hess, “York YVWABCDFXJE0125SA”, 145.9 RT Specification, York/JCI, 2018
- [37] York, “York YVWA User Manual”, York/JCI, 2015

Retrieved from:

[https://www.johnsoncontrols.com/pt\\_br/-/media/jci/be/united-states/hvac-equipment/chillers/files/be\\_yvwa\\_res\\_singlecompressor\\_maintenance.pdf?la=pt&hash=7A4F36336E4FFECA49A4071D4F1A3468780DF53C](https://www.johnsoncontrols.com/pt_br/-/media/jci/be/united-states/hvac-equipment/chillers/files/be_yvwa_res_singlecompressor_maintenance.pdf?la=pt&hash=7A4F36336E4FFECA49A4071D4F1A3468780DF53C)

- [38] AHRI, “AHRI Standard 550/590 – 2018 Standard for Performance Rating of Water-chilling and Heat Pump Water-heating Packages Using the Vapor Compression Cycle”, AHRI, Arlington, VA, 2018
- [39] S. Kakac, H. Liu, “Heat Exchangers – Selection, Rating, and Thermal Design”, Second Edition, University of Miami, Florida, CRC Press LLC, 2002
- [40] D. Q. Kern, “Process Heat Transfer”, International Student Edition, Case Institute of Technology, McGraw-Hill International Book Company, 1983
- [41] Bell & Gossett, “e-1510 Model 3EB “, Technical Data Sheet, Bell & Gossett/Xylem, 2020
- [42] Bell & Gossett, „e1531 Model 3BD “, Technical Data Sheet, Bell & Gossett/Xylem, 2019
- [43] E. Hess, “York YVWABCBDXJE0125SA”, 125 RT Specification, York/JCI, 2018
- [44] AHRI, “1997 Guideline for Fouling Factors: A Survey of Their Application in Today’s Air Conditioning and Refrigeration Industry”, AHRI, Arlington, VA, 1997
- [45] K. J. Lambers, “Isentropic and Volumetric Efficiencies for Compressors with Economizer Port”, International Compressor Engineering Conference, Paper 1920, School of Mechanical Engineering, Purdue University, West Lafayette, IN, 2008

*Software:*

- [46] RI CAD, V5.1.1, PI Diagram Software, Student Version, HiTec Zang GmbH, 2014, Germany
- [47] LabVIEW 2018, National Instruments, 2018, USA
- [48] EES 2020 ME, Engineering Equation Solver, V10.834, F-Chart Software
- [49] Dymola, Thermodynamic Modeling Software, Dassault Systems, France
- [50] MATLAB, Natick, The MathWorks Inc., Massachusetts
- [51] Modelica, Otter, Modelica Association, Germany

## VITA

Andreas Josef Höß was born in 1994 in Fürstfeldbruck, Bavaria. After school he completed a vocational training and worked as technician for Diesel engines at MAN Diesel & Turbo SE in Augsburg, Germany. In 2017 he completed his undergraduate education at the European University of Applied Science in Maintal, Germany and finished with a Bachelor of Science in Refrigeration Technology (B. Sc.). The undergrad application was succeeded by an employment as product manager at the heat exchanger manufacturer Güntner GmbH & Co. KG with a focus on control technology for heat exchangers. He joined the Master's in Science and Mechanical Engineering (MSME) program at the Purdue University in West Lafayette, Indiana in spring 2020 which he is expected to finish in December 2021. The focus of his Master's research was on thermal science and the testing and optimization of chillers with vapor compression cycle and screw compressor. This work included the baseline testing of a chiller and the development and conduction of accelerated life test cycles. The research work was done at the Ray W. Herrick Laboratories in West Lafayette, Indiana. He will continue PhD work at Purdue further focusing on refrigeration systems.

## PUBLICATIONS

A. J. Hoess, D. Ziviani, J. E. Braun, E. A. Groll, “Leistungsverhalten von Schraubenverdichtern im Langzeitbetrieb – Basistest der empirischen Untersuchung”, Performance behavior of screw compressors in a long-term operation – Baseline testing, Conference Presentation, Purdue University, Annual DKV Conference, DKV, 2020, Magdeburg

A. J. Hoess, N. P. Salts, D. Ziviani, J. E. Braun, E. A. Groll, “Baseline testing of a variable-speed water-cooling Chiller according AHRI standard 550/590”, Conference Paper, Purdue University, 12<sup>th</sup> International Conference on Compressors, City University, London, 2021

A. J. Hoess, D. Ziviani, J. E. Braun, E. A. Groll, “Veränderung der Leistungskennlinie im Dauerbetrieb – Untersuchung eines wassergekühlten Kaltwassersatzes mit Schraubenverdichter”, Change of the characteristic line in long-term operation – Investigation of a water-cooled screw chiller, Conference Presentation (was awarded as the best student presentation), Purdue University, Annual DKV Conference, DKV, 2021, Dresden